Building Policy-Aware Research Test Beds: Lessons from Laboratory Development for Optical Neuroimaging

by
Casey Gail Evans
B.S., Electrical Engineering
United States Air Force Academy, 2017

Submitted to the Institute for Data, Systems, and Society and the Department of Electrical Engineering & Computer Science in partial fulfillment of the requirements for the degrees
of
Master of Science in Technology and Policy
and
Master of Science in Electrical Engineering and Computer Science
at the
Massachusetts Institute of Technology
June 2019

Signature of Author_____ Signature redacted
Institute for Data, Systems, and Society Technology & Policy Program
Department of Electrical Engineering & Computer Science
May 10, 2019

Certified by_____ Signature redacted
Megan H. Blackwell
Technical Staff, Advanced Imager Technology Group, Lincoln Laboratory
Thesis Supervisor

Certified by_____ Signature redacted
George C. Verghese
Henry Ellis Warren Professor of Electrical Engineering
Thesis Reader

Accepted by_____ Signature redacted
Noelle Eckley Selin
Associate Professor, Institute for Data, Systems, and Society and
Department of Earth, Atmospheric and Planetary Sciences
Director, Technology & Policy Program

Accepted by_____ Signature redacted
Leslie A. Kolodziejski
Professor of Electrical Engineering and Computer Science
Chair, Departmental Committee on Graduate Students

Building Policy-Aware Research Test Beds: Lessons from Laboratory Development for Optical Neuroimaging

by

Casey Gail Evans

Submitted to the Institute for Data, Systems and Society Technology Policy Program and the Department of Electrical Engineering & Computer Science on May 22, 2019, in partial fulfillment of the requirements for the degrees of Master of Science in Technology and Policy and Master of Science in Electrical Engineering and Computer Science.

Abstract

Despite the prevalence of applications for compelling technologies, communication between scientists and policy makers is often obfuscated by conflicting philosophies concerning the role of science and technology in decision-making. Research test beds are here proposed and defended as a critical component of technologist-decision-maker communication. Approaches that enable a test bed to more effectively achieve such communication are enumerated, discussed and then compared with examples from the design, setup and validation process of a gated time-domain diffuse correlation spectroscopy (TD-DCS) test bed. Gated TD-DCS is a novel optical neuroimaging technique that can be used in applications that require higher spatial resolution than electroencephalograms (EEGs) but more portability than Magnetic Resonance Imaging (MRI). The gated TD-DCS test bed described here is the first of its kind for evaluating gated detector performance in a TD-DCS system and the methodology used for this test bed development is explored in depth. Lessons learned from test bed development in this wholly new field are then used to reassess the role of test beds in facilitating faithful policy applications of technology. This study highlights the significance of science-policy communication and illustrates through concrete example one promising method of improving such communication.

Thesis Supervisor: Megan H. Blackwell
Title: Technical Staff, Advanced Imager Technology, MIT Lincoln Laboratory

Thesis Reader: George C. Verghese
Title: Henry Ellis Warren Professor of Electrical Engineering, MIT

Acknowledgments

Wow, you are reading my master's thesis. Thank you. I was told no one would read this document—and especially not the acknowledgements—so thank you for being an outlier. We need more people like you in this world. This is the culmination of a two year journey, so there are many people to thank, and I will approach it as a series of toasts in the style of formal dinners at the Academy:

To Douglas McKechnie, for being absurdly clever and getting me interested in law—and, by proxy, policy. (*To Douglas!*)

To Rich Younger and Jon Frechette, for introducing me to research. (*To Rich and Jon!*)

To John Kuconis, for the Military Fellows program at MITLL. (*To John!*)

To Jeff Mendenhall, for making this adventure possible and being one of the best leader-mentors I've ever worked for. (*To Jeff!*)

To Shane Crippen, for guilting me into a dual degree. (*To Shane!*)

To Shireen Warnock for great lunch conversations, hikes, and more than one great recommendation at the start of this journey. (*To Shireen!*)

Pierre-François Wolfe (and Java and Macha and Chai), for being generally excellent and a highlight to Lincoln. (*To Pierre!*)

To Jane Luu, for words of harsh encouragement, a trip to a library, the chance to walk with bears, and delicious food. Please don't curse me if you read this, though I shall embrace Arthur Plotnik's thoughts: "I want to be so offbeat that crazed readers chase me down alleys." It would maybe mean I wrote something worth getting upset about. (*To Jane!*)

To Lorenzo Vigano, for believing in me and introducing me to the greatest random things ever. (*To Lorenzo!*)

To Saeyoung Rho, my first friend at TPP. (*To Saeyoung!*)

To Micah Ziegler, for lab thoughts, and for the idea of including NIST. He probably wants me to mention that the U.S. Air Force has more planes than the US Navy, in case there was any kind of confusion. (*To Micah!*)

To Barb DeLaBarre, for tea time and the inerasable mental image of flying manatees. (*To Barb!*)

To Noelle Selin, for making me feel like thinking outside the box is okay and helping me through my first ginormous paper. (*To Noelle!*)

To Frank Field, for incredible patience with my absurdities and for pushing me to think even more outside of the box. (*To Frank!*)

To Miles Lifson, 黎靚, Grégoire JACQUOT, and the rest of the TPP Family, for unconditional support and friendship and for showing me that the world is bigger and more filled with interesting ideas than I imagined. (*To TPP!*)

To Judy Gertner and Francis Shen, for encouraging me and introducing me properly to law and neuroscience. (*To Judy and Francis!*)

To Andy Siegel, Brian Aull, Oleg Shatrovoy, Niyom Lue, and George Jordy, for sharing in the learning experience of diffuse correlation spectroscopy (and sometimes near-infrared spectroscopy). (*To MITLL!*)

To Davide Tamborini, Mari Franceschini, and Stefan Carp, for being helpful and kind when answering questions on diffuse correlation spectroscopy and test bed setup. (*To MGH!*)

To Jonathan Schiller and Allie Sedgewick, for putting up with me these past two years, you're both going to go far in life, for sure. (*To Jon and Allie!*)

To Jasmine, for being an agile and spunky Scottish Terrier. You set the example for all of us. (*To Jasmine!*)

To Mom, for being you. (*To Mom!*)

To Ben, for believing in me and being kind all the time. (*To Ben!*)

To Dad, for helping me think through things, and for teaching me that sometimes the most important thing that you get out of an education is a way of thinking more than the knowledge itself. (*To Dad!*)

To Megan Blackwell, for careful edits. (*To Megan!*)

And finally, to George Verghese, for getting me through this thesis. (*To George!*)

Contents

List of Figures

List of Tables

Chapter 1

Introduction to policy-awareness

In academia, the term 'research test bed' evokes many ideas, each specific to its own field. The overarching idea of a test bed, however, is a space, whether physical or simulated, where something in development is evaluated in some way. This could apply to a yard for the development of a child, a pitch for the evaluation of soccer cleats, or a simulated market for a model of economic understanding. For the purposes of this thesis, the qualifier 'research' is used to extract the subset of test beds that pertain to the advancement of knowledge in the empirical disciplines, such as science and engineering. Charles Plott defines this subset of test bed purposes being "to determine if the process can be implemented and how it works once it is implemented" [1]. This thesis will focus on research test beds for technological development, but the means by which the lessons learned can be applied to broader practices in science and policy will be explored in depth.

A policy question is one in which the solution indicates the implementation of, and therefore commitment to a particular course of action [2]. In this sense, every deliberate action or inaction is a form of policy. But few people live in total isolation, and a person's private actions are less concerning to a society than actions that impact others. So a policy is of broader interest when it involves a collective commitment to change norms or standards of how people operate together.

A policy-aware research test bed achieves two fundamental goals: (1) science communication and (2) experimental rigor. These goals are important because they ensure that a test bed can appropriately address a policy question. That is, the test bed is able to evaluate something in the manner it is intended to evaluate it and is able to communicate the results of that evaluation to the user. The importance of these values can be expressed as preventing two unacceptable extremes. One extreme is knowing a test result exists and not being able to fairly understand it and the other is being able to understand the result but knowing that it is imprecise. Although these are two extremes, there is no inherent tradeoff between communication and rigor. An ideal state is one in which the research test bed is able to accomplish its goal, which is to inform the user of the knowledge developed through the tests, so the best result is achieved when both science communication and experimental rigor are maximized.

Science Communication

Communication is critical to the execution of even the most well-made plans. Evidence of this can be found at the heart of both humanity's greatest accomplishments and its greatest failures, when communication or

miscommunication decided the outcome. For instance, power dynamics blurred the conversation between U.S. President John F. Kennedy and his advisors during the Bay of Pigs invasion of Cuba in 1961 resulting in disaster for the American trained Cuban troops. Conversely, meticulous planning and communication made the Berlin Airlift of 1948-1949 an incredible demonstration of the capabilities of large-scale air transportation that we make use of today [3]. Science communication does not always have such immense repercussions, but it is nonetheless a key component of translating research test bed outputs into actionable influences for the decision maker in a policy situation.

It follows that to design a policy-aware test bed, consideration must be made for science communication. The goal of science communication is achieved when test bed results influence the decision maker in a logical way. The magnitude of the influence can be zero, if the information is irrelevant or dwarfed by other deciding factors, but the influence should always be vectored in alignment with the meaning of the results. If there is some miscommunication, then the influence on the decision maker could be illogical. Illogical influence is undesirable because it indicates that even though the results may have been carefully produced, the noise added when applying the results to a decision distorted its meaning to the point that only noise (mistaken for a signal) was communicated. If this is the case, then the effort made to develop precise results is partially wasted and a decision has been made based on noise rather than experimental evaluation. We have lost both efficiency and accuracy.

Communication is challenging, and there remain several obstacles to constructing a policy-aware test bed. The most fundamental obstacle is that human communication is both sender and receiver dependent. For senders, they can only incorporate into their expression what they perceive or understand. In the Bay of Pigs historical example, Kennedy's advisors interpreted their best option to be communicating agreement with the President, since that was perceived as the direct route to further their careers. A more basic example considers how two people would describe a location when one is standing in a valley and the other is standing on a mountain. They are describing the same place but their understanding and perception of the features would vary. On the receiver's end, we must accept that humans are imperfect users of information. Not only are receivers also limited by their perception and understanding, but their resulting action or inaction will depend on how the information is interpreted and incorporated into their existing knowledge. Since policy is about commitment to action (or inaction), the user interpretation is especially relevant from a policy perspective.

Even when the sender and receiver understand a communicated test bed result, user interpretation effects can reweight the influence of that result to something illogical in the collective stakeholders' perspective. For example, if an

investigator needed to show a certain result to make their supervisor satisfied, they may publicize outlier results more prominently than the median. Decisions are rooted not only in reason, but also in opinion, experience and feeling. And because policy fundamentally implies decision-making, then policy will always have a connection to judgement calls and decisions. Since these reactions to information are based on individual logic, the decisions themselves are not necessarily illogical, but they do complicate the process of scientific communication, since they require the policy-aware senders to consider their audiences' motivations relative to those of the group of stakeholders to ensure relative weights are properly communicated for group-wide logical influence. For example, if a test bed reports that blockchain technology performs a given calculation 10.4 times more efficiently than traditional methods under certain conditions, someone who is drawn to trendy words might decide to use blockchain in future work, even though they would not do so if the report referenced a novel networking technique instead. Figure 1-1 outlines the communication path of a test bed result to the user.

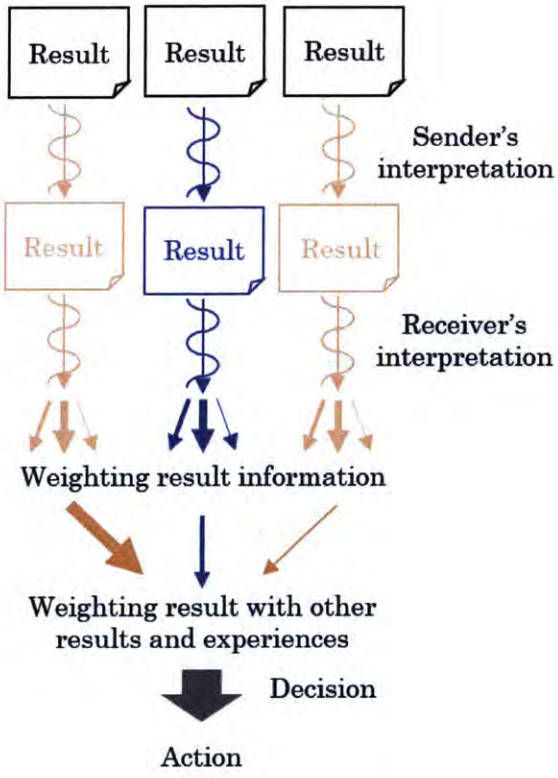

Figure 1-1. Outline of the science communication process. A test bed result must first be interpreted by the sender, then transmitted to the receiver who interprets the information themselves and then weights the importance of each component of the result to extract and summarize their own understanding. This summary is further compared and weighed against the user's prior experiences and

understandings of previous results, culminating in a decision and resulting policy (deliberate action or inaction).

But further complicating individual-to-group logic is the truth that there is no simple way to determine the weight ratio between individual and collective logic, since there is no deterministic response for a human when they receive a certain message. So unlike nature, which dictates a ball on Earth with no external acceleration other than gravity will fall at 9.81 m/s^2, a human may use that information to catch the ball if they feel confident, or simply watch it fall if they fear embarrassment for failing. For a policy-aware test bed to contribute to making the most logical decisions possible for a group, we would need to read the receiver's mind to recover the proper weighting scheme for the each component of the result. This is certainly outside the scope we would expect even from a policy-aware test bed but there are ways to facilitate the use of an appropriate frame of reference when considering the test bed result.

To overcome these interpretation obstacles, we can consider the central questions: "How will science be interpreted when the sender and the receiver do not use the same vocabulary?" and "How can people who speak the same language still miscommunicate and have misunderstandings?" One solution could be utilizing intermediaries who know a bit about both worlds and act as translators between the sender, who works directly with the test bed, and the receiver, who is directly making policy decisions. A second solution could be to balance the skills of those who know how to make decisions with limited information, commit to those actions, and follow them through, with the skills of those who can make a decision as informed as possible so that there is compromise between momentum and enduring legacy. Additionally, adding people with diverse perspectives to a team would reduce noise during the information-weighting stage of communication. Another option is to explore the more basic link between policy and technology, using test beds that inherently incorporate policy considerations and communicability into them.

A policy-aware test bed can achieve science communication by using scientific rigor as a common language among scientists and, to some extent, engineers, and record details of results that will enable a report consistent with the audience's background. This can alleviate the translation barrier in science communication for research test beds. For example, a test bed that records distances in meters is more easily interpreted than a test bed that records distances in hedgehog spikes. Similarly, well-commented code will be more transparent to the user than poorly commented code. There is a balance between incorporating new information and using recognized standards that is critical to moving forward in science. If a test bed never expresses new ideas as distinct from established standards, then we will forever be limited by our current understanding of the world. But if research test

beds only record details that cannot be related to existing literature, no one will ever understand them. So a policy-aware test bed must be a balance because it needs to answer a question that requires new information, since no one would be asking about it otherwise, but in a way that does not misrepresent information because of its difficulty to understand. Furthermore, a policy-aware test bed is designed to record results in terms of the question it is trying to answer with reference to the questions it does answer, to minimize misunderstandings on the part of the user.

Experimental Rigor

The second goal of a policy-aware test bed assures that the output to be communicated is as precise an evaluation of what it tests as it can be. Achieving experimental rigor requires understanding the empirical nature of the task required of the test bed and addressing the research question as directly as possible, recording the assumptions that arise from using a model, cleanly recording results, carefully analyzing and iterating on the investigation and appropriately building on the works of others. Many of these tasks are incentivized by the current structure of science education and the scientific community. For example, the National Institute of Standards and Technology (NIST) in the United States serves as a definition space for numerous measures and tests, and other institutions and academic peer-reviewed journals serve as standards for reporting rigorous science. The scientific community is not in agreement on every topic, and peer-reviews are far from perfect, but scientific rigor still gives more weight to the test, and more meaning in a policy context.

Despite support from the community for many aspects of scientific rigor, some components are easier to overlook with the current system. These include replicating results, considering basic assumptions, and avoiding selection bias in deciding which reports to highlight. Maintaining scientific standards alleviates the need for experiment reproduction to compare results, but not for improving the statistical information surrounding those results. Repeated experiments can be just as important as the first attempt at a certain test. This concept bleeds into the need to continue to assess the basic assumptions of even a very complicated system. A rigorous test must include checks to ensure that what is assumed is actually the case, at least to the extent that upon reflection the results make sense given the assumptions. The whole point of debugging and testing is that something may be wrong that was not expected to be wrong. A scientist who does not investigate these cases is failing to meet meaningful standards of scientific rigor. With assumption checks, the test bed is more informative, but also more likely to be exposed to the areas where it fails in a controlled manner. And when tests fail, it is important to not fall for the tendency of downplaying these results. By acknowledging

uncertainty alongside certainty and failure alongside success, the test bed can more effectively contribute to the forum of empirical observation.

There are ethical aspects to scientific rigor as well. Ethics is essential for scientific rigor because it creates an environment where results can be trusted, where scientists are appropriately incentivized to produce rigorous results so that they can be recognized for their work. The Accreditation Board for Engineering and Technology (ABET) recognizes this crucial role, and considers engineering ethics as a necessary component of professional formation. Although people try their best, knowing how to operate in a way that treats others with respect in a socially-fabricated environment like the engineering community is not instinctual, and comes from a social contract that must be taught for people to recognize the impact of their actions. Respecting experimental rigor therefore requires believing in something bigger than the individual and acknowledging the work of those who come before and those who will come after.

1.1 Motivation

Policy-aware test beds are representative of what science is for a society, and are therefore an integral part of scientific and societal progress. The ensemble of science communication and experimental rigor embodied in policy-aware test beds integrates what have become two distinct and specialized units of society: researchers and politicians. Industries, institutions and individuals would not invest time and money into research if they did not consider it important. Policy-aware research test beds promote more efficient use of resources, to get more "importance" for less cost. Ideally the significance of these projects aligns with improvement for human welfare, since humans are funding the projects, but even in cases where the incentives are skewed for selfish gain or with hurtful intent, policy-aware test beds improve the clarity of human understanding and are less likely to fall into such traps. For instance, it is harder to misuse results to support a personal claim if the results include comments on the context in which they can and cannot be used. Likewise, it is harder to misrepresent results, when they are clearly presented and carefully supported from basic assumptions.

The idea of policy-aware research test beds is not new. The National Institute of Standards and Technology (NIST) was chartered in 1901 by the United States Congress to appease electrical components manufacturers who were struggling to make progress with inconsistent standards. NIST demonstrates by its existence and influence that the quest for standardizing science communication and rigor is historically relevant for the United States. Looking further back, scales, written records, and measures themselves have existed for millennia as a means of minimizing loss in trade. Even now, in the news near the time of this publication, the crash of two of Boeing's 737 MAX aircraft has highlighted the responsibility of

standardization and evaluation organizations like the Federal Aviation Administration (FAA) and the National Transportation Safety Board (NSTB) [4]. Clearly, even in 2019, testing and measurement standards are critical for life saving as well as for scientific progress. This example, which involved an American manufacturing company's impact on carriers from Indonesia and Ethiopia, also highlights the global importance of policy-aware test beds. In 2012, French ambassador Sylvie Bermann spoke in Suzhou, China, saying that she sees the European Union as the world power in standards [5]. The mere idea of a world power in standards suggests opportunity for science diplomacy with policy-aware test beds. With global standards, science can be a lingua franca and means of cross-cultural communication. Moreover, developing universal standards requires compromise and intercultural understanding, which is an invaluable base for sustainable peace and cooperation. Policy-aware test beds are poised to step in to this critical role.

So the fact that policy-aware test beds have a positive impact on society is neither brand-new, outdated, nor esoteric, but this thesis seeks to add to this idea by considering what we can learn from the test beds themselves to improve both the policy approach and the calculation and representation of test bed results. To do this, a case study in building an optical neuroimaging test bed will be examined in detail. Optical neuroimaging is an especially interesting application to examine when considering policy-aware test beds because it is an applied field, because it investigates biology, and because it is a measurement technology.

Since optical neuroimaging is an applied science that intersects multiple disciplines, it must use both new and old methods, which constantly evolve as some function of the evolution of its derivative fields. As a sort of saddle point, this requires especially thoughtful use of scientific communication even within the field to continue moving forward effectively. Furthermore, since optical neuroimaging investigates biology, it is probing a subject that is challenging from a causal inference perspective, especially in terms of group to individual (G2i) and individual to group (i2G) assessment of results. This challenge, along with the inherently human nature of its application, makes optical neuroimaging technology especially interesting to study in depth. Finally, because imaging is a quest to learn more, it lends itself to the consideration of how knowledge itself makes an impact, rather than simply being technology that performs a task. This allows the case study investigation to make some conclusions about more basic sciences as well as technology development.

Gated time domain diffuse correlation spectroscopy (TD-DCS) as a particular modality of optical neuroimaging is suited to this investigation due to its novelty. The test bed designed here has never been built before, so few, if any, of the steps in its fabrication were predetermined. The selection of each component needed to be

considered using interpolations of multiple similar works. As a result, this test bed is not only a particularly challenging case to make policy-aware, and therefore a great means of investigating challenges to test bed development, but it can be broken down into pieces derived from different disciplines, each with a unique story to tell about how it came to be a part of the test bed.

1.2 Contribution and outline

To showcase the exploration of the intermingling of science communication and experimental rigor explored here in the introduction, the remainder of this thesis aims to:

- ✓ Develop a framework for analyzing and evaluating policy-aware research test beds according to the way the user interprets, and hence applies, the technology under development to a problem (Chapter 2)

- ✓ Introduce the foundational theory of gated TD-DCS in an approachable way and in the context of other technologies (Chapter 3)

- ✓ Explore the design, setup, validation, and to some extent operation, of a gated TD-DCS research test bed and simultaneously exemplify some of the means by which a test bed can be evaluated for scientific rigor (Chapter 4)

- ✓ Identify techniques to bridge the common misalignments between scientifically rigorous measurement and user interpretations and applications (Chapter 5)

Overall, this thesis contributes a rare perspective on the importance of research test bed development not only for achieving research goals, but also policy goals.

Chapter 2

Evaluating policy-aware research test beds

"Why is it so difficult for us to think in relative terms? Well, for the good reason that human nature loves absoluteness, and erroneously considers it as a state of higher knowledge."

–Professor Felix Alba-Juez, University of Utah, 2011

In this section, I develop a policy model to facilitate the evaluation of research test beds for technology development. The policy model is intended to facilitate research test bed development for more effective science—i.e., science that is easily applied to human questions—and more effective policy—i.e., policy that is better informed. In particular, the model will first identify the human goals of the test bed that led to the research investment. Then, the model will consider those goals to isolate the specific influences and interpretation effects involved. The use of this model to find mitigation strategies for these influences and interpretation effects will also be discussed as a means of examining the quality of the model itself. Chapter 5 will consider the application of the model to the optical neuroimaging test case and how the neuroimaging test case can be used to improve the model.

2.1 Background

From Chapter 1, a policy question is one in which the solution indicates the implementation of, and therefore commitment to a particular course of action [2]. This contrasts with scientific questions, which create a space to evaluate evidence for or against a testable hypothesis, and research questions, which seek knowledge rather than action, but there remains room for overlap among the three types of questions, especially in technology policy. Policy context refers to the space of policy questions that can be answered by a technology. A question falls within the policy context of a technology if the question relates what a technology does—which in the case of gated TD-DCS is a specific measurement—to a particular action in an application. However, the application that the technology is used for certainly incorporates other elements of design not related to the science of the technology. For example, indicator lights, procedures, and laws help translate data into actions for the involved parties. These facets of an application are not within the policy context of a technology, but rather the problem space addressed by the purpose of the application. These concepts surrounding policy context are summarized in Figure 2-1, but note that subject areas, purposes, and applications can and do overlap. Briefly, we can consider how this framework could be applied to gated TD-DCS.

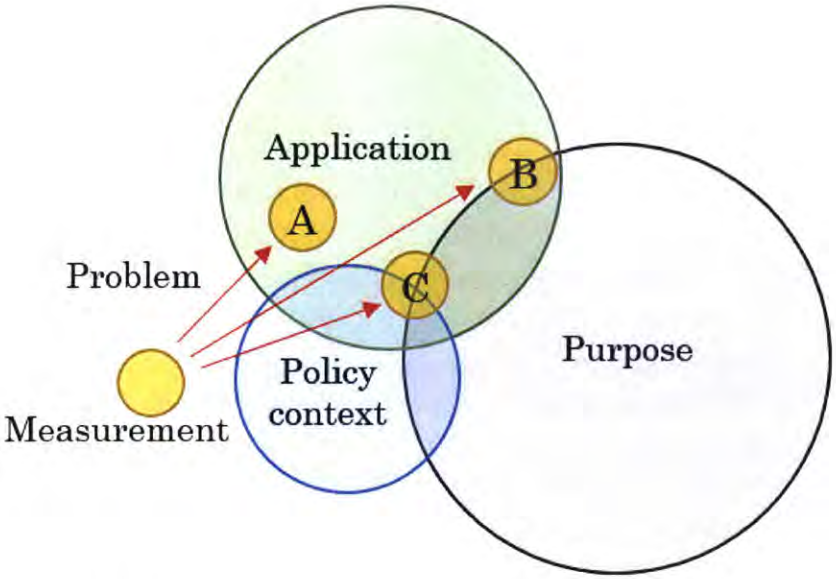

Figure 2-1: Defining policy context. A problem can be approached with a certain goal, or purpose, in mind. Trying to achieve the purpose involves specific applications of a technology to the problem. The problem statement guides the measurement into some application, as shown here. Some of these applications fall within the policy context of the measurement made by the technology, meaning that those applications are valid from a scientific perspective. In the diagram, measurement use A is an application where the purpose is not addressed properly and the measurement is outside of its policy context, measurement use B can respond to the purpose, but is still outside of the measurement's policy context, and measurement use C can be within the policy context and meet the purpose if properly interpreted. Measurement uses with overlap like measurement C are the best case. Proper use of a policy-aware test bed increases the probability of falling in the intersection of all four circles.

Consider the example purpose of improving military flying. The policy questions that can feasibly be addressed by gated TD-DCS for military flying can be derived from certain identified applications of gated TD-DCS in military flying, such as aircraft design, pilot training, and pre-flight risk mitigation. For example, an appropriate policy question for aircraft design in military flying could be: "By what methodology can we integrate the gated TD-DCS recorded measurement of the cerebral metabolic rate of oxygen ($CMRO_2$) from a pilot into the flight controls system?" or "How do the $CMRO_2$ levels of a specific pilot change from the use of one flight controls system to another?". These policy questions are framed such that a gated TD-DCS system could reasonably provide an answer which has a clear implementation. These questions emerge from the application of neuroimaging to

the purpose of creating a pilot-adapted flight controls system to address a human factors problem in U.S. military flying. Similar logic can be applied to determine the policy context of other applications of gated TD-DCS for military flying.

Evidently, there are also many questions pertaining to purpose that do not fall within the policy context of gated TD-DCS. Such questions relate the purpose to inappropriate implementations of gated TD-DCS. For example, going back to the aircraft design phase example, if we instead asked "How can we use pilot stress levels as an input to the aircraft control system?" or "Do pilots have more trouble using control system A or control system B?" we would be asking inappropriate questions of gated TD-DCS. "Inappropriate" here does not mean that gated TD-DCS cannot provide evidence to the question or that the questions are outside of the application space, but it does mean that gated TD-DCS cannot address the question without additional input from other research or policy areas. Another way to understand why these questions are inappropriate is by considering that gated TD-DCS does not measure the concepts of "stress" or "trouble". Instead, the measurements that are made by gated TD-DCS can only be correlated with specific definitions of "stress" or "trouble" through controlled experiments. These definitions are determined by behavioral researchers, or even policy makers. Unless the definition of the concept in the question matches, or has a testable relationship with, the definition of the concept in one of the controlled experiments, the policy question falls outside of the policy context of gated TD-DCS. The policy question will also fall outside of the application space if gated TD-DCS cannot even be used in further studies or alongside other inputs to provide evidence in support of or opposition to a question in the problem space.

2.2 Model development

Approach

To develop an appropriate model and framework for evaluating policy-awareness in a research test bed, I will start with two assumptions. The first is that a measurement and the measurement's purpose will intersect where the measurement is applied. The second is that the user's interpretation defines the application. In other words, I assume that a measurement fulfills a purpose according to how it is used. Building from these assumptions, I will classify various user interpretations in terms of their perspective on the purpose of the measurement. These groupings can be used to classify both the interpretations of a test bed measurement applied to a problem *ex post facto* and the interpretations of a test bed measurement applied to the problem it was developed for. For each type of user interpretation, I will explore some of the ways in which that interpretation can fail to be policy-aware. These potential failures and risk levels will be the parameters of the model.

The secondary stage of the model approximates the objective function of policy-awareness for research test beds by using the parameters developed in the first stage. As defined in Section 2-1, the policy context of a measurement is the scope of the measurement in a scientific or statistical sense. By comparing the user interpretation of the application in terms of the identified parameters with the policy context of the measurement, the test bed can be evaluated according to how well it aligns the two, so part of the model development will involve consideration of how this comparison should be performed in a repeatable fashion.

The final stage of the model will be an optimization framework developed by estimating the possible adjustments that can be made based on the evaluation of the objective function model. Consideration of the model is intended to lead to insights about how adjusting the test bed, the application, or both could possibly converge to an ideal test bed or else regularly adapt to changes over time. The model approach is summarized as a flowchart in Figure 2-2.

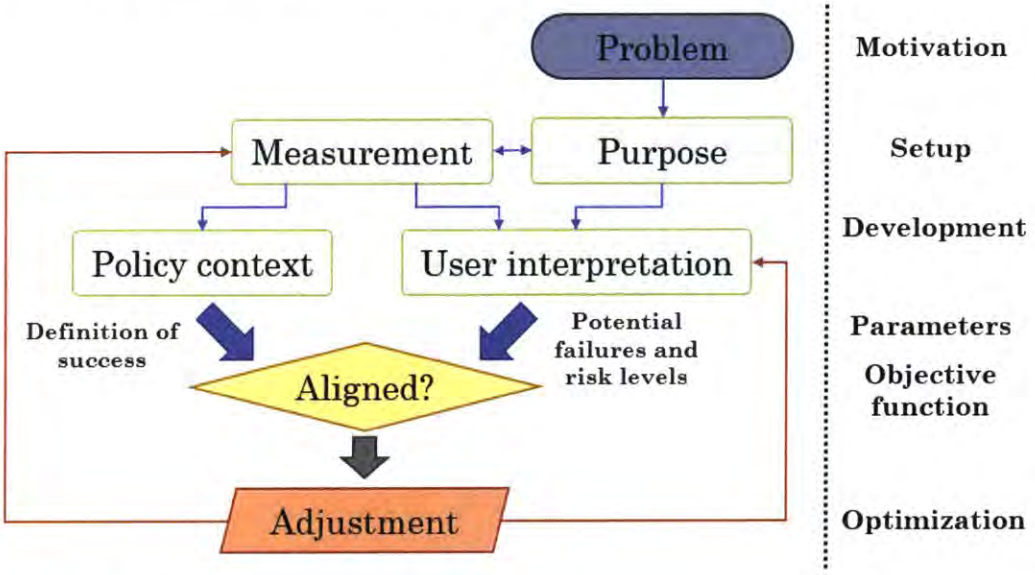

Figure 2-2: Model development. Problems motivate research and technology goals that aim to achieve a purpose that addresses the problem. Measurements are made to achieve that purpose. Alternatively, measurements are made independently and then applied to a purpose different from the original. Each measurement has a policy context and one or more applications based on user interpretations. Comparing the policy context and modeled user interpretation informs adjustments that can be applied to the test bed, the application, or both.

Evidence

The relevant evidence to develop a model and framework for evaluating policy-aware research test beds includes technology policy literature, historical examples, and deductive reasoning based on the approach framework. Specifically, the evidence will focus on describing user interpretation and identifying potential areas of misalignment with the policy context. In Chapter 4 the optical neuroimaging test bed case study will also be incorporated as evidence for improving the model. It is important to note that the goal of this model is not to create stagnant or "gold" standards for evaluating policy-aware research test beds, but rather to serve as a means of navigating considerations for design and development of such test beds. Similarly to how measurement science allows a field to deconvolve the measurement from the experiment in order to divide the challenge of rigorous science and continue moving forward, this model is meant to be both usable and adaptable as new evidence comes to light.

2.3 Characterizing user interpretation

To categorize user interpretation, it is important to consider how people approach problems. When a group of individuals has posited some problem to be researched, there are many ways of doing so. Some users seek to solve the problem so that it is no longer a problem, but a solved thing, an answer. This is a practical, or tactical, mindset. Other users investigate the problem to learn more about it and then approach it in light of what they know, reminiscent of an engineering approach. And some just try to approach the problem, and in approaching it shape how they think about it. This approach is in the spirit of basic research.

The effectiveness of the application is determined by user interpretation. Sometimes user interpretation stays within the policy context of a technology, but often it reaches beyond. For example, if the user asks a research test bed to answer a question or to provide evidence outside of its policy context, the effectiveness of the test bed is hindered by an inappropriate evaluation of scope. Consequently, if the user considers test bed results as an answer to a question, the user is applying the question to the policy context even when it does not belong there. This misalignment implies that the test bed is now serving a different purpose than the purpose defined originally which can in turn impact how future iterations of the technology are designed. Knowing that the user interpretation may not align with the policy context of a technology, technology itself becomes an inquisitive method that shapes the way that we understand and define the problem addressed by the purpose. The three subsections of Section 2.3 will consider the implications of using a research test bed as an answer, as evidence or investigation, and as a question or approach, respectively.

2.3.1 Test bed results as answers

Perhaps the most common misuse of technology is to use what is called the technocratic approach outside of the policy context of a technology. The technocratic approach sees technology as an answer to any problem. From this perspective, if only we make the camera fast enough, the laser pulse clean enough, and the results processed enough, there is nothing beyond our ability to solve. In such a world, the value of the solution lies entirely on the ends; the means and the stakes of the problem to be solved become lost in the quest for an answer. That is, overconfidence in technological advancements improperly justifies that this is the way the problem should be solved and that solving it in this way is better than not solving it. This has two major implications: (1) scientists and engineers often fail to adequately prepare their contributions for the skewing it will face under stress in society and (2) when technology is applied to solve a question that is not answerable by science, the solution it posits is still imbued with the trappings of scientific confidence. This creates situations where either the science is not ready for the policy application or the policy application is not ready for the science. Both of these implications will be discussed below.

To address the first consequence of the technocratic approach, policy expert Langdon Winner analogizes the situation of engineering negligence to Mary Shelley's Gothic novel *Frankenstein.* In his article, Winner likens engineers to Dr. Frankenstein, who begins his research optimistically in a quest to "show how [Nature] works," but once his work was achieved, fled his lab and abdicated moral responsibility for his creation [6]. Winner argues that engineers tend to have a similar disregard for the work that they do. This may be because the engineers who develop technologies balance tight schedules, conferences, sponsor meetings, precise budgets, promotions, and grant proposals on top of their research and as a result they feel pressured to move on to the next technology with the hope that they are leaving their work in the capable hands of policy makers [6,7].

Another possible explanation for this resignation to the ether is the concept of technological optimism, developed by philosophers Mary Tiles and Hans Oberdiek, which claims that technology is value neutral [8]. This idea is characterized by the sentiment that "if only people understood or had or used X, then they could solve their problem." It does not ask what should be done or what will happen when the problem is solved in this manner. The technology itself is merely a tool to be used. It is an answer for both good and evil. For gated TD-DCS, this refers to the engineers who consider only the implications of the policy questions that gated TD-DCS can and cannot answer, thinking that the reported technical specifications of the technology, determined with some underlying statistic thresholds, are sufficient for even nonscientists to understand the scope. Applications where the technology is

used to measure something that it is statistically unlikely to be able to measure properly are ignored because the assumption is that the engineers only have responsibility to the implications of the ideal use case. The unfortunate consequence is that the rationalization of limited effort on the part of engineers to address the social implications of their work can lead to situations where the science is not ready for its application. Compounding this issue is the variation between disciplines for what thresholds determine what is "statistically unlikely." For example, while a biomedical application may consider an R^2 statistic of 0.6 indicative of a high likelihood of a relationship, a social science application may consider any R^2 value below 0.95 a weak indication of a relationship, and any application not expecting a linear relationship would find this statistic useless.

The second consequence of the technocratic approach leads to the neglect of the presence of questions that transcend science, which in turn leads to misguided conclusions. Sometimes this is due to a Type III error, which occurs when a researcher correctly answers the wrong question [1,9]. This can also result from what Deborah Stone refers to as "fallible indicators," which are data based in categorization biases, assumptions inherent in the decision to measure something, the power dynamics of numerical information or the reactions of the thing being measured [10]. These fallible indicators look like and often are results of empirical method, but have internalized noise from nonscientific sources. For example, if gated TD-DCS were applied to evaluate stress-related performance criteria for post-flight pilot debriefs, and if a pilot observes that practicing challenging maneuvers results in abnormal measurements, the pilot may refrain from building experience in those areas in order to seem more at ease in the cockpit than her peers. In such a case, the pilot may seem to have higher performance metrics, but in reality, she has just learned how to work within the system. Addressing this manipulation would require policy efforts beyond science. Here, solutions might include positive feedback for performing well in stressful conditions, or adding weight to other performance metrics, such as the quality and challenge of the maneuvers, in feedback.

Another manifestation of the second consequence is consideration of trans-science research questions as science questions. As defined by Alvin Weinberg, trans-science relates to "questions of fact and can be stated in the language of science, [but] are unanswerable by science." Weinberg's examples of trans-science include determining harm from extremely low doses of radiation, determining the probabilities of improbable events, engineering as a discipline, and predicting the behavior of an individual [7]. The developers of gated TD-DCS technology, and neuroscientists in general, ask how physiological processes in the brain can be quantified and used to understand its inner workings. These questions about quantifying brain activity fall into trans-science, because engineers modify

technology according to their design process as well as rigorous scientific understanding [7]. Air Force policy asks how understanding of the brain contributes to predicting degraded performance in flying operations. Predictive models never represent science alone, and yet neuroimaging can be applied to help answer such questions. In cases where policy tries to objectively answer trans-science questions with a test bed, policy makers are at risk for being unprepared to incorporate test bed results in policy.

2.3.2 Test bed results as evidence

To counter the double-edged sword of researchers and decision-makers not being ready for each other, a policy maker can frame a user interpretation that considers test bed results as evidence rather than a solution to inform a problem approach. The United States legal system has proposed a few different standards for incorporating expert scientific testimony into the court decision-making process that may be useful guidelines for the policy equivalent. The most commonly referenced standards are known as the Frye standard, the Daubert standard and the pertinent sections of the Federal Rules of Evidence [11]. This section will also consider a framework proposed by earth scientist Danielle Wood that can help a policy maker understand the value of scientific evidence when it reaches into the space beyond its explicit policy context. These guidelines can help the user understand the utility of information that is not explicitly an answer to their question.

To briefly summarize, the Frye standard is sometimes known as the "general acceptance" test and is satisfied when "the thing from which the deduction is made [is] sufficiently established to have gained general acceptance in the particular field in which it belongs [12]." The Daubert standard is a bit more robust with four recommendations for considering scientific evidence: (1) whether the theory or technique has been or can be tested, (2) whether the theory or technique has been peer reviewed, (3) whether the information presented considers uncertainties, and (4) whether there is general acceptance for the theory or technique [13]. A policy-aware research test bed should meet all four of the Daubert criteria. Indeed, any rigorous scientific study should meet all of these criteria, except perhaps the general acceptance test, which could be achieved after a time.

The takeaways from the Federal Rules of Evidence are that evidence should have some relevance to the purpose, and that a technology's translation of scientific evidence into policy should help the user understand the evidence or make a determination, be based on sufficient facts or data, be the product of reliable principles and methods reliably applied to the problem space [14]. The appropriated Federal Rules of Evidence suggest what evidence from a research test bed to consider valuable for policy-awareness. The first idea suggests that the

communication of test bed results to the user, whether through direct interaction with the test bed or through mediation via an expert in the field, should be informative for decision making. This could be accomplished with scientific input on the crafting of checklists for interpreting the output of a research test bed. The second and third ideas suggest that even when a research test bed is not being used to answer a problem, it cannot release its grasp on scientific rigor in the role of evidence. The fourth and final idea suggests that when a research test bed is applied to areas outside of science, efforts must still be taken to ensure that the application has been made in good faith and is not needlessly outstepping the bounds of reasonable application.

Dr. Danielle Wood proposes an 'application value chain' that flows from evidence within the explicit policy context of a technology all the way to decision support, which is at the heart of policy questions. The eight steps are (1) system design and implementation, (2) system operation, data retrieval, calibration and validation, (3) data correction and processing, (4) modeling and assimilation of observations, (5) providing an interface to find and explore data, (6) creating a data interface based on user needs, (7) combining physical, social, economic and other data, and (8) providing recommendations for action [15]. For research test beds this framework can help guide the conversation between engineers and policy makers to ensure that critical steps in the process are not forgotten before arriving at the evidence level steps (4)-(8). This framework is also useful in identifying application areas that fall within the scope of using research test beds as evidence. The remainder of this thesis focuses on test bed design and validation, with some mention of test bed operation, addressing steps (1)-(2), but there is great potential for future work that would consider the remaining steps of the value chain.

One scholastic method of applying legal evidence that can be applied to scientific evidence in a policy context is a five step process that begins with listing the facts, and continues with a description of the issue that the court, or research facility, is tasked with resolving. Next, the rules that pertain to the case are enumerated. The fourth step is to apply the rules and facts to the issue and analyze the result. The final step is to draw conclusions [16]. This method also has potential for breaking down and analyzing evidence from research test beds.

2.3.3 Test bed results as questions

Using a research test bed as evidence is an excellent way to work within an application space, but the policy maker must also be aware of instances where the purpose area is ill-formed and the user is in danger of making a Type III error. Fortunately, test bed results can also be used as an inquisitorial method, or feedback loop, for redefining the underlying purpose. This area shows promise due to some inherent properties of technology. The properties discussed here are (1) that

technology is a generative metaphor for the purpose it serves and (2) that technology is an inherent source of values. By capitalizing on these inherent properties, technologies like gated TD-DCS can and are used to inform purpose statements in each round of policy implementation.

Policy theorist Donald Schön defines generative metaphors as descriptions that constitute a perspective and can simultaneously act as a process for creating new perspectives [17]. By this definition, technology is a type of generative metaphor because it embodies the current understanding of science with respect to the purpose it serves and leads to translations of that science into new perceptions about its possible applications. This concept is in line with the saying: for someone with a hammer, every problem is a nail. In this sense, considering how test bed results could be applied to a problem affects how we think about that problem. For example, the technology of gated TD-DCS could be used to monitor aircraft pilot blood flow. This implies the aircraft and the pilot could be considered an integrated unit on which system diagnostics could be run to help with in-flight risk mitigation. Where previously the purpose may have been to ensure that the pilot know when the aircraft is degraded, using gated TD-DCS we can now consider the purpose of ensuring that both the pilot and the aircraft are mutually informed of each other's, and their own, statuses. From this we can see that using different metaphors allows the policy maker to look behind the problem-solving process at the problem setting process.

But technology as a generative metaphor has further implications. In the article "Materializing Morality: Design Ethics and Technological Mediation" (2006) Peter-Paul Verbeek argues that because technology shapes both how people perceive the world and how they act in it, it carries moral weight and is an inherent source of values [18]. With this reasoning, technology provides the policy maker with insight about the moral background of a problem that may be fracturing the stated purpose from the true purpose. For example, a hypothesized gated TD-DCS brain computer interface (BCI) missile firing system is one solution for the purpose of improving the speed and responsiveness of a missile system to pilot input; however, the idea of firing a missile with concentrated thought clearly highlights ethical concerns. Contemplating how this problem could be addressed with gated TD-DCS asks the developer to consider what it means to make missile a thought away. If such a thought is unacceptable, then maybe a more accurate statement of the purpose might be to improve the speed and accuracy of pilot input with respect to missile systems decisions. With a more accurate statement of purpose, Type III error is reduced.

2.4 Evaluation using the model

The policy model outlined in Figure 2-2 can now be filled in with the user interpretation characterizations and the potential policy-awareness failures and risks they entail. Recall that the problem motivated the setup, which performs some measurement to achieve some purpose, recognized either before or after the measurements were made. In development the policy context of the technology and the user interpretation are identified. The policy context answers the question: scientifically speaking, what purposes can the technology fulfill? The user interpretation effects, as explored in Section 2.3, answer at least one of three questions: (1) what are we answering with the technology? (2) what does what we are doing with the technology show? and (3) what are we asking with the technology. In the style of the Jeopardy game show, user interpretations can be categorized by determining which question best suits how the user understands the role of the technology. Naturally, this is a subjective classification, but I argue that it is nonetheless useful because it enables the user to identify the potential failures and risk levels most relevant to their understanding.

If (1) seems like the most appropriate question relating to the use of the technology, the technology is seen as a solution. This interpretation class has the highest risk of misalignment with the policy context as most of the worthwhile human policy questions cannot be answered by science alone. Additionally, the possible failures of this interpretation are overconfidence and incorrect uses of science, which can be damaging to the scientific community through inevitable loss of credibility if the error is not identified and dealt with appropriately.

If (2) seems like the most appropriate question relating to the use of the technology, the technology is seen as an investigation. This user interpretation has only a moderate risk of being out-of-alignment with the policy context. Failures of this interpretation arise when the weights given to the technology output is unreasonably high or low. For example, if the majority of the scientific community agreed that smoking has health risks, but the user highly weighted a few isolated studies that found smoking has no health risks, this would constitute an unreasonably high weighting. These failures could lead to decisions that are not broadly applicable or that are simply poorly informed.

If (3) seems like the most appropriate question relating to the use of the technology, the technology is seen as an approach. This user interpretation will always be in alignment with the policy context, and therefore seemingly low risk, but it is also the least useful in a policy setting as it does not lead to an action. Potential failures in this case are not related to the effects of this user interpretation on policy outcomes, but rather on the difficulty of such studies to continue or even exist in the first place. Despite the fact that studies using

technology as an approach can improve the understanding of a problem, because they do not directly tie to clear outcomes they can be hard to motivate, and struggle to find funding or support. This difference with the other two user interpretations implies that studies where technology is interpreted as an approach use a more scientific than technocratic mindset. An additional concern if a user has this interpretation is that they may be blinded to possible negative outcomes of the test bed results when others apply them to policy development.

Despite these potential failures, there is a chance that the user interpretation and policy context will align. Examples of proper alignment for each of the user interpretation categories in the case of using a cerebral metabolic rate of oxygen ($CMRO_2$) measurement for the purpose of improving aircraft-pilot integration are provided here to illustrate the concepts. If a user interprets the technology as a solution and the technology made aircraft-pilot integration seamless such that aviation performance were uninhibited, it would be reasonable to assume, at least until further results suggest otherwise, that $CMRO_2$ was the missing link. Likewise, if a user interprets the technology as an investigation and the technology indeed collects information that appropriately informs a solution to aircraft-pilot integration, it would be reasonable to assume that $CMRO_2$ has something to do with aircraft-pilot integration. Finally, if a user interprets technology as an approach, and the technology opens the solution and investigation space by asking if $CMRO_2$ has anything to do with aircraft-pilot integration, then it is reasonable to assume that $CMRO_2$ is a way of thinking about the topic of aircraft-pilot integration.

More often than either extreme, the user interpretation will be partially, but not completely, aligned with the policy context. The next question is: how can we align policy context with user interpretations? That is, how can we make it so that what we are trying to decide is within the realm of what is measured? This adjustment of both the test bed measurement and the user application is the focus of Chapter 5. Having already explored possible user interpretations, the next step is to develop the example of gated time-domain diffuse correlation spectroscopy (TD-DCS). This will build the intuition required both to identify adjustments that can be made to the test bed in order to align the measurement with various applications, and to identify adjustments that can be made to the applications to be more aligned with the measurement. Since gated TD-DCS is such a novel system, I outline the theory and compare it to other neuroimaging modalities in Chapter 3, then closely consider the measurements of the test bed, including test bed setup and component validation, in Chapter 4.

Chapter 3

Background on the optical neuroimaging test bed

This chapter seeks to build a foundational understanding of diffuse correlation spectroscopy (DCS) and its position in the neuroimaging community so that the gated time-domain diffuse correlation spectroscopy (TD-DCS) research test bed under development at the Massachusetts Institute of Technology Lincoln Laboratory (MITLL), which is described in Chapter 4, can be used as an example to identify potential adjustments for either the test bed or the user's application of test bed results to more appropriately address policy concerns. This theoretical overview will cover diffuse correlation spectroscopy theory, its applications, its comparison with other neuroimaging techniques, and will be followed in Chapter 4 by a careful consideration of the test bed assembly, including selection criteria and validation tests for all major components of the test bed.

3.1 Diffuse correlation spectroscopy theory

Diffuse correlation spectroscopy (DCS), also known as diffusing wave spectroscopy (DWS), is attributed to the 1996 University of Pennsylvania dissertation by David Boas and has been patented by the same [19,20]. Earlier work in diffuse spectroscopy was done by Boas' mentor, Arjun Yodh [21,22,23], and the work has been continued by several of Yodh's other students, including Chao Zhou [24], Meeri Kim [25] and Xingde Li [26]. Other universities looking into DCS include the University of Kentucky [27,28] and Boston University [29], among others [30]. The Athinoula A. Martinos Center for Biomedical Imaging is affiliated with Massachusetts General Hospital (MGH) and the Health Sciences and Technology (HST) joint program between Harvard University and the Massachusetts Institute of Technology. Optics @ Martinos is a group of research labs within the Martinos Center, including the lab of Maria A. Franceschini who is our primary partner in DCS research and a major contributor to the field [31].

3.1.1 Overview

Diffuse correlation spectroscopy (DCS) theory is described in Section 3.2.1.1 and different measurement strategies are described in Section 3.2.1.2. DCS is an optical technique that uses laser illumination to measure changes in how the coherent laser light diffuses among moving red blood cells [32]. An index of blood flow (BFi, in cm^2/s) can then be measured by fitting the slope of the temporal intensity autocorrelation curve to that of the solution to a model derived from the

diffusion equation [31]. Note that BFi for head measurements is sometimes called cerebral blood flow index (CBFi). The BFi is extremely sensitive to estimates of the optical properties used in the diffusion equation model, so analysis and applicability of DCS are greatly improved by using a time-domain (TD) method to ascertain the temporal point spread function (TPSF) and time of flight (ToF) data required to make *in situ* estimation of the optical properties [31].

Though BFi is more accurate than tissue oxygen saturation (SO_2) in estimating cerebral blow flow (CBF), which is a known biomarker for impaired cerebral autoregulation, a few research groups have turned to combining functional near-infrared spectroscopy with TD-DCS in order to more accurately measure the cerebral metabolic rate of oxygen ($CMRO_2$) [33,34]. Functional near-infrared spectroscopy (fNIRS) and TD-DCS can share data acquisition [32]. However, combining these modalities presents several design challenges, because while fNIRS and the measurement of optical properties can be performed with arbitrarily short pulses, and perform better as pulses become shorter, TD-DCS requires pulses with long coherence length. The fNIRS modality is examined in more detail in Section 3.2.2.

3.1.2 Theory

3.1.2.1 Basic principles

Transport theory considers radiative transfer of particles in electromagnetic radiation to be affected by three processes: emission, absorption, and scattering. For a given phase unit, which is a point in space at a given time with some direction, emission describes how particles contribute to the radiance of the phase unit, absorption describes how particles diminish the radiance of the phase unit, and scattering describes the transfer of radiance between the phase unit and other phase units. Considering the combination of these three processes in a linear fashion results in the radiative transfer equation (RTE), which describes conservation of radiance for a phase unit

$$\frac{1}{v}\frac{\partial}{\partial t}L(\vec{r},\Omega,t) + \Omega \cdot \nabla L(\vec{r},\Omega,t) + [\mu_a(\vec{r}) + \mu_s(\vec{r})]L(\vec{r},\Omega,t) = S(\vec{r},\Omega,t) + \int_0^{4\pi} L(\vec{r},\Omega',t)\mu_s(\vec{r},\Omega' \to \Omega)d\Omega' \tag{3.1}$$

where $L(\vec{r},\Omega,t)$ is the energy radiance (in $Wm^{-2}sr^{-1}$) of the phase unit at position $\vec{r}$ (in m), in direction Ω (in sr), at time t (in s). For dimensional analysis, note that steradian is a unitless dimension. See Appendix B for more details on solid angle directions. Additionally, v is the speed of light (in ms^{-1}) in the medium; $\mu_a(\vec{r})$ is the absorption coefficient (in m^{-1}) at position $\vec{r}$; $\mu_s(\vec{r})$ is the scattering coefficient (in m^{-1}) at position $\vec{r}$; and $S(\vec{r},\Omega,t)$ represents the source (in $Wm^{-3}sr^{-1}$). The term $\mu_s(\vec{r},\Omega' \to \Omega)$ is the scattering coefficient at position $\vec{r}$ specifically for scattering

events from direction Ω' to direction Ω. It is also commonly written as the product of $\mu_s(\vec{r})$ and $P(\Omega, \Omega')$, the probability of scattering from direction Ω' to direction Ω, also known as the phase function. Note that direction Ω is often written as $\hat{s}$, and the sum of $\mu_a(\vec{r})$ and $\mu_s(\vec{r})$ is often written as $\mu_t(\vec{r})$.

The first term on the left hand side of Equation 3.1 accounts for the changes in radiation over time, the second term accounts for the contribution of the spatial gradient of radiation to the movement of particles against the Ω direction, and the third term accounts for both the loss due to scattering away from the Ω direction and the loss due to the absorption of particles in the phase unit. The first term on the right side accounts for the source and the second term accounts for the scattering from all other directions to the Ω direction. In general, the terms on the left hand side of Equation 3.1 are attributed to particles leaving the phase unit, and therefore add to the radiance of the phase unit, while the terms on the right hand side are attributed to particles entering the phase unit, and therefore subtract from the radiance of the phase unit. For radiative equilibrium, assumed in this case, these two sides must be equal [19,35].

The radiative transfer equation is notoriously difficult to solve for all but the most reductive of systems. To make the solutions more tractable, the following assumptions are often made: (1) the radiance, source and phase are approximately equal to their truncated spherical harmonics series expansion; (2) the phase probabilistic scattering coefficient function (i.e. $\mu_s(\vec{r}, \Omega' \rightarrow \Omega)$) is only dependent on the change in direction of the particle, $\Omega \cdot \Omega'$; (3) the source is isotropic; and (4) the scattering frequency is much greater than the frequency of the time dependence of the source (i.e. the scattering particles have moved a distance much smaller than a wavelength of light during one period of the source). Assumption (2) further requires $\mu_s(\vec{r}) \gg \mu_a(\vec{r})$, anisotropy factor $g(\vec{r}) < 0.99$, where $g(\vec{r})$ is the average cosine of the scattering angle (so we require not too much anisotropy), and the source-detector separation be much greater than the inverse of the reduced scattering coefficient, $\mu_s'(\vec{r})$, which is defined as

$$\mu_s'(\vec{r}) = \big(1 - g(\vec{r})\big)\mu_s(\vec{r}) \tag{3.2}$$

These assumptions are often reasonable in diffusive media, so the resulting approximate equation, known as the diffusion equation, is

$$\frac{1}{v}\frac{\partial}{\partial t}\Phi(\vec{r}, t) - \nabla \cdot \frac{1}{3\big(1 - g(\vec{r})\big)\mu_s(\vec{r})}\nabla\Phi(\vec{r}, t) + \mu_a(\vec{r})\Phi(\vec{r}, t) = S_0(\vec{r}, t) \tag{3.3}$$

where $S_0(\vec{r}, t)$ is the isotropic component of the source, and the flux $\Phi(\vec{r}, t)$ (in $\mathrm{Wm^{-2}}$), which here is interpreted as the photon fluence, is the sum of the radiance, or energy flow, in all directions from a point.

Photon fluence is represented by the equation

$$\Phi(\vec{r},t) = \int_0^{4\pi} L(\vec{r},\Omega,t)d\Omega \tag{3.4}$$

Methods based on the RTE (Equation 3.1) or the diffusion equation (Equation 3.3) can be used to measure static light scattering and absorption. Static light measurements are especially insightful in the near-infrared, where the differences in the absorption spectra of oxy- and deoxy-hemoglobin and water indicates the relative concentrations of these components [36]. Such measurements have been used to calculate blood oxygen saturation, tumor tissue properties, and blood volume, which can be useful for numerous medical applications involving brain tissue properties, blood content, and oxygenation [24]. Diffuse correlation spectroscopy (DCS), however, is concerned with dynamic light scattering and absorption. These dynamic properties emerge from the movement of scatterers such as red blood cells (RBCs). To measure the influences of these dynamic particles, a generalization to the RTE (Equation 3.1) and the diffusion equation (Equation 3.3) will need to be made. This can be done by considering the autocorrelation of speckle intensities at the detector [24].

In diffuse media, light that has travelled from a collimated source will appear as a pattern of speckled intensities at the detector. This is due to the constructive and destructive interference that occurs from photons that have travelled different path lengths to arrive at the detector. Movement within the turbid, or diffusive, medium will cause the speckle pattern to change over time. By considering the intensity correlation over time of a single speckle, the movement in the turbid medium can be quantified. To do this, we can consider that intensity is analogous to fluence with units of Wm^{-2} and therefore related to radiance, and can be modelled as a transfer much like the RTE (Equation 3.1), in what is known as the correlation transfer equation (CTE) [37]

$$\begin{aligned}\frac{1}{v}\frac{\partial}{\partial t}G_1(\vec{r},\Omega,t,\tau) + \Omega\cdot\nabla G_1(\vec{r},\Omega,t,\tau) + [\mu_a(\vec{r})+\mu_s(\vec{r})]G_1(\vec{r},\Omega,t,\tau) \\ = S(\vec{r},\Omega,t,\tau) + \int_0^{4\pi} G_1(\vec{r},\Omega',t)g_1^s(\Omega,\Omega',\tau)\mu_s(\vec{r},\Omega'\to\Omega)d\Omega'\end{aligned} \tag{3.5}$$

where $G_1(\vec{r},\Omega,t,\tau)$ is the unnormalized multiple scattering temporal electrical field autocorrelation, $\langle E(\vec{r},\Omega,t,\tau=0)E^*(\vec{r},\Omega,t+\tau)\rangle_t$ (in V^2m^{-2}) at position $\vec{r}$ (in m) in direction Ω (in sr), at time t (in s), and lag τ (in s). The operator $\langle\dots\rangle_t$ is the average over all time for the function. The new term in the integral, $g_1^s(\Omega,\Omega',\tau)$, is the normalized electric field correlation for single scattering from the Ω' direction to the Ω direction at lag τ, represented by the equation

$$g_1^s(\Omega,\Omega',\tau) = G_1(\vec{r},\Omega,t,\tau)\langle|E(\vec{r},\Omega,t,\tau=0)|^2\rangle_t^{-1} \tag{3.6}$$

Aside from replacing $L(\vec{r},\Omega,t)$ with $G_1(\vec{r},\Omega,t,\tau)$, the only qualitative difference between the RTE (Equation 3.1) and the CTE (Equation 3.5) is the addition of $g_1^s(\Omega,\Omega',\tau)$, the single scattering term. This term decays at greater lags, demonstrating that correlation functions, unlike radiance, are not necessarily conserved. Use of this term assumes that the scatterers in the media are spread enough to use single scattering in the calculation. As a first order calculation, this assumption is often reasonable for common applications of light passing through a volume of scattering particles [38]. At zero lag, the CTE (Equation 3.5) reduces to the ensemble-averaged field intensity, $|I(\vec{r},\Omega,t)| = \langle|E(\vec{r},\Omega,t)|^2\rangle$, analogous to the RTE (Equation 3.1). An ensemble average, denoted by $\langle\dots\rangle$, is an average over all possible realizations of the function. In ergodic systems, the ensemble average equals the time average, $\langle\dots\rangle_t$.

The CTE (Equation 3.5), like the RTE (Equation 3.1), has a diffusion approximation, and it is known as the correlation diffusion equation

$$\frac{1}{v}\frac{\partial}{\partial t}\mathrm{G}_1(\vec{r},t,\tau) - \nabla\cdot\frac{1}{3\mu_s'(\vec{r})}\nabla\mathrm{G}_1(\vec{r},t,\tau) + \mu_a(\vec{r})\mathrm{G}_1(\vec{r},t,\tau) + \frac{1}{3}\mu_s'(\vec{r})k_0^2\langle\Delta r^2(\tau)\rangle = S_0(\vec{r},t) \tag{3.7}$$

where k_0 is the wavenumber in m^{-1} (also given by $\frac{2\pi n}{\lambda}$, where n is the index of refraction in the medium and λ is the wavelength of light in a vacuum in m) and $\langle\Delta r^2(\tau)\rangle$ is the mean square scatterer displacement in m^2, and is equal to $6D_B\tau$ in Brownian motion, where D_B is the effective Brownian coefficient in units of $\mathrm{m}^2\mathrm{s}^{-1}$, and $\langle V^2\rangle\tau^2$ in random ballistic flow, where $\langle V^2\rangle$ is the mean square speed of the random flow in $\mathrm{m}\cdot\mathrm{s}^{-1}$.

The last term on the left hand side was introduced as a result of $g_1^s(\Omega,\Omega',\tau)$, the decay term added to the integral on the right side of the CTE (Equation 3.5). With this term, additional assumptions are required for the correlation diffusion equation (Equation 3.7): (5) the photons are diffusing, so a photon random walk step is much shorter than the measured object's dimensions and the absorption length, μ_a^{-1}; (6) the normalized single scattering temporal electrical field correlation $g_1^s(\Omega,\Omega',\tau)$ is only dependent on the scattering angle, $\Omega\cdot\Omega'$, which is true when scatterers are randomly oriented and have isotropic dynamics, as in Brownian motion and random ballistic flow, where the former involves collisions of particles with fluid molecules and the later involves molecular collisions within a fluid due to turbulent eddies [39], but notably not in directional flows; and (7) scattering particles move a distance much shorter than λ, so $k_0^2\langle\Delta r^2(\tau)\rangle \ll 1$, and the lag τ is much less than the time it takes a scatterer to move one wavelength. Otherwise, the correlation diffusion equation (Equation 3.7) is analogous to the diffusion approximation (Equation 3.3).

Solving the correlation diffusion equation in a semi-infinite homogeneous medium [30] results in

$$G_1(\rho,\tau) = \frac{\nu S_0}{4\pi D}\left(\frac{e^{-K(\tau)r_1}}{r_1} - \frac{e^{-K(\tau)r_2}}{r_2}\right) \tag{3.8}$$

where ρ is the source-detector separation in m, S_0 is the source intensity, and the remaining terms are defined as follows:

$$D = \frac{\nu}{3\mu_s'} \tag{3.9}$$

$$K(\tau) = \sqrt{3\mu_a\mu_s' + \mu_s'^2 k_0^2 \alpha \langle \Delta r^2(\tau)\rangle} \tag{3.10}$$

$$r_1 = \sqrt{\rho^2 + z_0^2} \tag{3.11}$$

$$r_2 = \sqrt{\rho^2 + (z_0 + 2z_b)^2} \tag{3.12}$$

$$z_0 = \mu_s' \tag{3.13}$$

$$z_b = \frac{2}{3\mu_s'}\frac{1 + R_{eff}}{1 - R_{eff}} \tag{3.14}$$

where R_{eff} is the effective reflection coefficient, which depends on the ratio of the indices of refraction in and out of the medium, and α is the percentage of light scattering events from moving scatterers [24]. The value of α is 1 in an Intralipid® phantom and estimated as 0.01 for red blood cells in tissue [24].

The location of the isotropic approximation of a collimated source is one scattering length into the medium, as given in Equation 3.13. The term z_b given in Equation 3.9 represents the extrapolated zero boundary condition, which is satisfied by a negative isotropic imaging source at $-(z_0 + 2z_b)$ [40]. Equations 3.11 and 3.12 give the Pythagorean distances from z_0 and $-(z_0 + 2z_b)$, i.e., from the source and imaging source respectively, to the detector, defined to be at $z = 0$. This geometry is summarized in Figure 3-1.

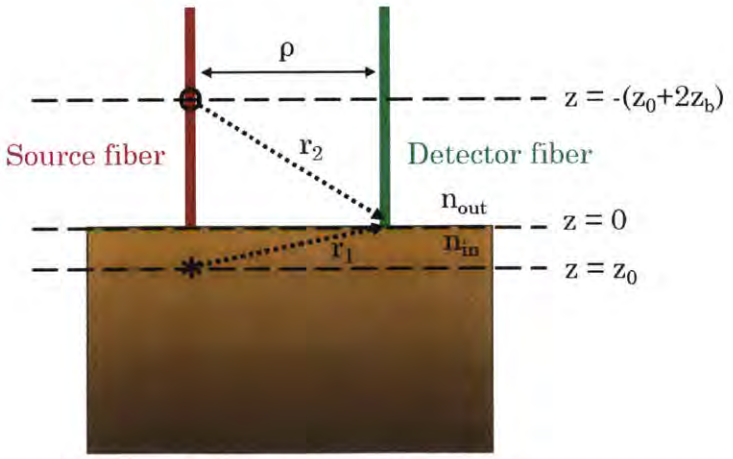

Figure 3-1: Semi-infinite homogenous medium assumed geometry. The geometry used to solve the correlation diffusion equation for the result in Equation 3.8. Adapted from Figure 2.1 in [24].

To estimate blood flow, we use the blood flow index (BFi), which is calculated as

$$BFi = \alpha D_B \tag{3.15}$$

and is in units of cm^2s^{-1}. Typically, blood perfusion is measured in units of mL/min/100g, but BFi correlates well with standard measures of absolute flow as measured by numerous other methodologies [24,31]. Since the detector measures the intensity, a DCS measurement is actually first used to find the unnormalized temporal intensity correlation, $G_2(\rho,\tau)$. The intensity correlation is related to the field correlation by the Siegert relationship [30]

$$G_2(\tau) = \langle I(t)\rangle^2 + \beta|G_1(\tau)|^2 \tag{3.16}$$

which for normalized correlations reduces to

$$g_2(\tau) = 1 + \beta|g_1(\tau)|^2 \tag{3.17}$$

where β is an ideality parameter ranging from 0 to 1 [30], influenced by several factors including the coherence length and stability of the laser, detection optics, and the number of detected speckles. Long coherence length and low numbers of detected speckles (preferably a single speckle) improve the measurement [19,24]. Ideally, $\beta = 1$ [19,30], but without a polarizer the best value is 0.5 due to the inverse relationship of β with the number of detected speckles, or laser modes [31].

Considering everything up until this point, the goal of time-domain DCS is to build a temporal intensity autocorrelation function that can be used to solve for BFi in the correlation diffusion equation (Equation 3.7). This can be done by considering a photon stream that has travelled from a coherent source through some diffuse medium to a detector. Typically, timestamps are taken because they contain the most information. There are three approaches to computing the intensity autocorrelation of these timestamps that will be discussed here: (1) time-domain convolution; (2) frequency domain multiplication using the fast Fourier transform (FFT); and (3) building a histogram of interarrival times [30].

The first two methods require an explicit intensity function in time. To build an intensity function, photon arrival times stored in the length-N vector `'photons'` are converted into a binary signal `'I'`, where detections are indicated by a 1 and non-detections are indicated by a 0. For a measurement of t_{meas} seconds, where $t_{meas} = t_{end} - t_{start}$ with t_{start} being the first measured time in the experiment and t_{end} is the last measured time in the experiment, and time resolution Δt_{min} seconds, the binary signal will have length

$$T = \frac{t_{meas}}{\Delta t_{min}} + 1 \tag{3.18}$$

For example, if `photons` $= \{670, 860, 990, 1020\}ns$ and $\Delta t_{min} = 10ns$, then $t_{meas} = 1020 - 670 = 350ns$ and $T = \frac{350ns}{10ns} + 1 = 36$. Accordingly, `I` would be the length-36 vector with zeros everywhere except `I[0]`, `I[19]`, `I[32]`, and `I[35]`.

To compute the autocorrelation of `I` in the time domain, convolution is used

$$G_2[k] = \langle I[m]I[m+k] \rangle_n = \sum_{m=-\infty}^{\infty} I[m]I[m+k] = I[k] * I[-k] \tag{3.19}$$

where m is the time index and k is the lag. Note that the limits can be simplified such that $m \in \{0, \ldots, T-1\}$.

To find the normalized autocorrelation, $G_2[k]$ must be divided by $G_2[0]$, which is

$$G_2[0] = \frac{N^2}{T} \tag{3.20}$$

where T is the length of the intensity function and N is the number of detected photons. Note that this is simply the average square value of the binary intensity function.

Although using convolution in the time-domain is the most direct method of computing the autocorrelation, it is typically the most computationally costly. Even when only calculating for lags of interest (i.e. $k \in \{0, \ldots, k_{max}\}$), there are still Tk_{max} multiplications in Equation 3.19. The fast Fourier transform (FFT) presents the possibility of improving performance by processing the signal in the frequency domain. Because convolution in the time domain is equivalent to the cheaper multiplication operation in the frequency domain, and the FFT is able to perform efficient Fourier transforms, Equation 3.19 can be simplified with

$$G_2[k] = \mathcal{F}^{-1}\{\mathcal{F}\{I[k]\}\mathcal{F}\{I[-k]\}\} \tag{3.21}$$

where $\mathcal{F}\{\cdot\}$ is the FFT and $\mathcal{F}^{-1}\{\cdot\}$ is the inverse FFT. The frequency domain method presented in Equation 3.21 does not allow for discrimination with a maximum value of k, so all values of k will be computed; however, this method achieves a computational complexity of $\mathcal{O}(TlogT)$, which is often faster than time domain methods of Equation 3.19. Note that since the output of Equation 3.21 is also unnormalized, it must also be normalized by the $G_2[0]$ factor determined in Equation 3.20.

The third method is to take advantage of the binary nature of the intensity function to build a histogram of the interarrival times as an equivalent calculation of the autocorrelation. In one-indexed pseudocode this looks like

```
photons = timestamps   % 1:N
G2 = zeros(1:T)        % Initialize G2
for i in 1:(N-1)
     for j in (i+1):(i+kmax)
          G2(photons(i)-photons(j))+=1
     end
end
g2 = G2*T/N^2          % Normalize to g2
```

Here the signal can remain in timestamp form, which saves memory, as the signal 'I' is likely much longer than the signal 'photons.' This method also significantly reduces complexity by using summations instead of multiplications. If incoming photons are approximated as a Poisson process, the expected number of photons arriving within a certain time unit is the average number of photons that arrive within such a time unit. This expected value is typically denoted λ in Poisson statistics, but to avoid confusion with wavelength, I will use $\lambda_{E[I]} = N/T$. The histogram method therefore in expectation considers $N\lambda_{E[I]}k_{max}$ photon pairs. Since $N \ll T$ for a useful measurement, and k_{max} is also usually much less than T, this method will be faster than both the time domain and frequency domain methods.

Some time correlators use the multi-tau binning scheme, which uses time domain methods with a staircase of progressively longer lag steps to save on computational cost. Since this scheme also reduces noise artifacts by acting as a low pass filter at higher lags, the autocorrelation algorithm used by our lab rebins the output of our histogram method to resemble the multi-tau method output [30,41,42].

It is the job of the test bed to collect timestamps that can be used with this theory to produce meaningful results, both for evaluating the components of the test bed itself as well as the eventual measurement of BFi in biological studies. Chapter 4 will cover the test bed development in detail.

3.1.2.2 Variations on DCS

There are three varieties of light sources commonly used for optical measurements in diffuse media. These light sources constitute three approaches: continuous wave (CW), time domain (TD), and frequency domain (FD). In the CW approach, a source with constant intensity is used and the change in intensity is measured. In the TD approach, an impulse source is approximated with a sub-nanosecond pulse and the temporal point spread function (TPSF) is measured. In the FD approach, a source with modulated intensity is used and the phase shift and change in intensity is measured [24]. Note that the TD and FD approaches are Fourier transforms of each other and the CW approach is the FD approach at zero frequency (DC) [26]. These approaches are illustrated in Figure 3-2.

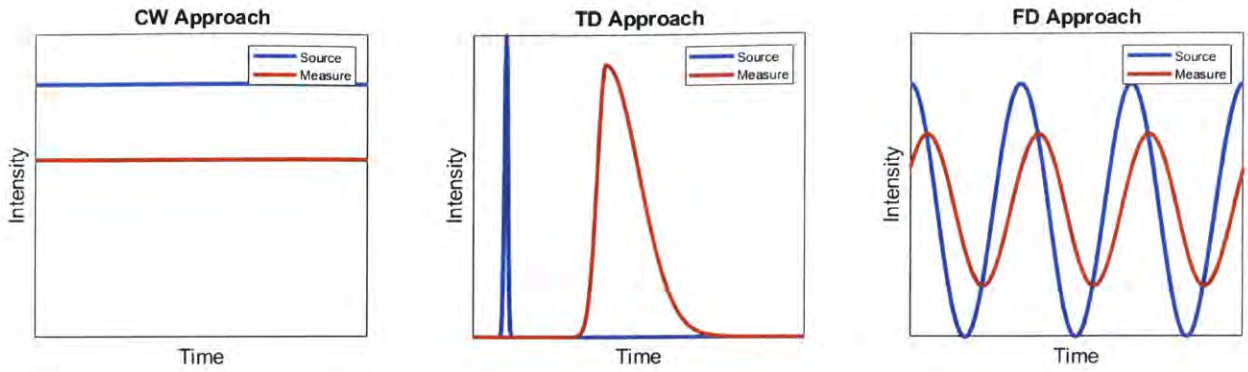

Figure 3-2: Approaches in diffuse media optical measurements. Optical measurements in diffuse media traditionally follow one of three approaches: (1) continuous wave (left), (2) time domain (center), or (3) frequency domain (right). The CW and FD approaches are shown at steady state.

Diffuse correlation spectroscopy (DCS) is typically implemented using a continuous wave (CW) source, as this greatly simplifies the technical requirements of the setup; however, the CW approach loses much of the potential information of a DCS measurement, as it only returns intensity information. The TD approach preserves the most information in the TPSF, but it requires the most challenging setup. In addition, the TD approach requires adjustments to the correlation diffusion equation (Equation 3.7) to correct for nonidealities resulting from laser pulse profiles, laser coherence length, and temporal dependencies in the detector instrument response function (IRF) [29].

As of May 2019, frequency domain (FD-)DCS has not been attempted, although frequency domain methods have been used in other applications of diffuse photon physics, including breast tumor imaging [43] and cerebral hypoxia measurements [44]. Frequency domain (FD) measurements would only return intensity and phase information. Since TD-DCS produces a TPSF, it is equivalent to running FD-DCS at a wide range of frequencies. FD-DCS does have the advantage of concentrating photon energy at a single frequency to decrease the impact of wide spectrum noise in amplitude; however, high noise in phase data defeats much of the potential benefit of FD-DCS [45]. Still, FD-DCS presents a compromise between the high information content of TD-DCS and the simplicity of setup of CW-DCS [26]. Despite these potential benefits, the remainder of this chapter will focus on the TD-DCS approach.

To address the fact that TD-DCS measurements are close to the noise floor, time-domain photon discrimination techniques are typically applied to TD-DCS outputs. The noise comes from the detector dark count rate (DCR) and other non-idealities in the detector, as well as photons originating from ambient light sources

and spontaneous emission. Neuroimaging applications are especially noisy due to high scattering in the scalp and skull, which causes a large flux of photons with short path lengths that never penetrate into the brain [43]. Fortunately, by applying certain computational methods to TD-DCS data, or by using detector gating, photons can be selected for longer pathlengths, which are more likely to have travelled through brain tissue [45]. This method of discarding photons outside of a certain set of pathlengths before computing the intensity autocorrelation has been referred to as a "time-gating scheme" [31], but it should not be confused with gated TD-DCS, which uses gated detectors that are synchronized with the laser pulses to only measure photons during a specified temporal window. The benefit of gated TD-DCS is that since the detectors are not turned on until after the peak reflections from superficial tissues have mostly passed, they are less likely to saturate with early photons and therefore are less likely to be resetting when late photons arrive. The test bed I built is intended to be used for the development of gated TD-DCS.

One final variation on DCS worth noting is the combined modality with functional near-infrared spectroscopy (fNIRS), which takes diffuse light measurements at two wavelengths: one where oxygenated hemoglobin is a more dominant absorber than deoxygenated hemoglobin, and another where the reverse is true [36]. Properties of oxygenation, hemoglobin concentration, and blood volume can be determined by comparing observations at these two wavelengths. While all three primary approaches to fNIRS (CW, TD, FD) can measure relative changes and differences in hemoglobin concentration by using the diffusion equation (Equation 3.3) to estimate μ_a and μ_s', the TD and FD approaches can also take absolute measurements of hemoglobin concentrations, since they are able to distinguish between intensity changes due to absorption and intensity changes due to scattering [30,46,47]. Functional near-infrared spectroscopy combined with dynamic observations of blood flow from DCS provide enough information to estimate the cerebral metabolic rate of oxygen, or $CMRO_2$ [48]. $CMRO_2$ is the rate of oxygen absorption in the brain as determined by an application of Fick's principle [49]

$$\frac{\partial q(t)}{\partial t} = F[C_A(t) - C_V(t)] \tag{3.22}$$

where $q(t)$ is the quantity of a substance in an organ, F is the arterial blood flow, $C_A(t)$ is the arterial concentration of the substance and $C_V(t)$ is the venous concentration of the substance. In the case of $CMRO_2$, arterial blood flow is approximated by BFi measured with DCS and the quantity $C_A(t) - C_V(t)$ can be determined by TD- or FD-fNIRS, as discussed in more detail in Section 3.2.2.

3.1.3 Noise models and statistical considerations

Fully understanding the theory also requires understanding the noise. This section will briefly consider some common noise dependencies in diffuse correlation spectroscopy and a few of the methods taken to mitigate that noise.

Noise in DCS has been shown to be primarily dependent on source intensity, integration time, and correlator settings. Note that the integration time is the time spanned by the measurements that are averaged into a single representative measurement for that time period. The noise is inversely proportional to the light intensity within the ranges typically used for DCS, inversely proportional to the square root of the integration time, and inversely proportional to the square root of the correlator bin size [24]. Other sources of noise include detector afterpulsing, shot noise, dark counts, electronic noise, ambient light, other non-idealities in the source or detector, computational time in the correlator, and the influence of superficial tissues in the scalp [45].

Different fields have different ways of mitigating noise. In economics, isolating the known from the unknown to still properly use causal inference considers tools like prior probabilities, discontinuity effects, and instrumental variables [50]. In technology development there is a series of calibration, modeling, validation, data correction, and data processing [15]. Statistics requires certain sample sizes to make meaningful conclusions. Mitigation strategies for DCS have included using few-mode fibers to increase light at the detectors (which do not necessarily decrease noise due to the increase in the beta parameter of Equations 3.16 and 3.17 as a result of multiple speckles passing through), building an analytical model to better fit the data to the correlation curve, and experimental validation of these noise models [24,45]. One interesting example of noise characterization in DCS has shown that despite higher intrinsic noise in TD-DCS, the depth sensitivity gained by selecting late photons is improved from the CW-DCS case [45]. Studies like this are valuable for comparing modalities and determining paths forward.

3.1.4 Interesting application areas

Time-domain diffuse correlation spectroscopy (TD-DCS) has been considered for several applications thought to pertain to blood flow. These include use in biomedical studies, as diagnostic tools for medical conditions, as monitoring equipment for hospital patients, and as input devices for new technologies. In particular biological studies under consideration for incorporation of TD-DCS include studies on blood flow changes during social tasks like group interaction or performance tasks like running or driving [51]. Medical conditions of interest for the technology include: (1) conditions where cerebral autoregulation may be impaired,

such as traumatic brain injury (TBI), spaceflight-associated neuro-ocular syndrome (SANS) [52], stress, depression, epilepsy, seizure, and anesthesia; (2) conditions where the tissues are not receiving enough blood, such as shock, stroke, and ischemia; (3) conditions where the tissues are filling with fluid or blood, such as edema and non-compressible torso hemorrhaging [53]; and (4) conditions with abnormal carbon dioxide (CO_2) concentration in blood, such as hypercapnia [31,32,54]. Technologies like brain-computer interfaces have considered TD-DCS as an input strategy, as blood flow is possibly an indicator of brain function [32].

Additionally, TD-DCS can be considered for applications that heavily weigh the non-invasiveness of a technology (which is especially relevant for cerebral applications), limit high-frequency radiation but accept powerful photon emission at relatively low frequencies, cannot be exposed to a large magnetic field, or have certain mobility requirements—either so that the technology can be brought to immobile patients or for studies of highly mobile patients.

3.2 Comparison with other neuroimaging modalities

Neuroimaging refers to any technique used to produce an image measuring some quality of the brain. This section considers the utility of those measurable features of the brain for policy applications as well as practical limitations such as cost and portability. To do this I will first define a set of terms used to categorize and evaluate neuroimaging data, then I will describe non-optical and optical neuroimaging technologies using these terms to evaluate the type and quality of information produced by each methodology.

The type of information provided by neuroimaging research falls into two main categories: structural and functional. Structural information describes the physical brain: for example, the location and size of brain regions, connective tissues, nerves, and circulatory membranes. Functional information describes the operations of the brain, that is, its neurologic, metabolic, hemodynamic, and immunologic processes [55]. Note that genetic features can provide insight about both the structural and functional brain, but are typically separate from neuroimaging because genetic features can also be observed from cells not originating in the brain tissue.

Each neuroimaging technology has its own specifications, but there are a few metrics that are frequently used to compare and contrast various modalities. These include temporal resolution, spatial resolution, penetration depth, cost, invasiveness, and portability. Temporal resolution refers to the sampling time and how well a measurement can be assigned to one time or another. For example, if Technology A has a temporal resolution of one second and Technology B has a

temporal resolution of 5 seconds, Technology A can distinguish between events that occur two seconds apart, while Technology B cannot. Spatial resolution is an analogous term but for the location of an event. Penetration depth refers to the maximum distance relative to the scalp from which a measurement can be made. Cost considers power, maintenance, development, and manufacturing requirements for the technology. There are certainly other metrics of merit, and some modalities do not ascribe to these categories, but these six metrics are among the most commonly used and will be helpful for the rest of this section.

3.2.1 Non-optical techniques

Non-optical neuroimaging methods are the most commonly discussed variety of neuroimaging in use today. The obvious reason for this trend is that the brain is hidden by several layers of scalp tissue and the skull, which readily absorb visible light, making it difficult for optical methods to meet the penetration depth requirement for most applications. Non-optical methods bypass this problem using sonic, radiative, electromagnetic, or other methods that either penetrate more deeply into the head or else use biomarkers that are observable at the surface of the scalp. Non-optical techniques can be used to measure both structural and functional information about the brain. The realm of non-optical methods is vast and diverse, but this section will consider the most widespread and representative modalities. Specifically, this section will identify relevant information provided by electroencephalography (EEG), magnetoencephalography (MEG), positron emission tomography (PET), computerized tomography (CT), functional magnetic resonance imaging (fMRI), and functional ultrasonic imaging (fUS).

Electroencephalography (EEG) and magnetoencephalography (MEG) are representative of electromagnetic neuroimaging methodologies. Both technologies consider functional features of the brain, since the changes in electromagnetic properties of the scalp are thought to be correlated with current flow across neuronal cellular membranes after a synaptic potential [56]. EEG detects electric potentials from a set of electrodes placed around the scalp. The preferred locations of these electrodes have been carefully studied to minimize noise from the scalp's diffuse conductivity. The spatial resolution is on the order of decimeters. The temporal resolution, however, is on the order of milliseconds [57]. MEG detects localized magnetic fields in the brain with spatial resolution on the order of decimeters and temporal resolution on the order of milliseconds [58]. EEG is three orders of magnitude cheaper than an MEG system [59] and is wearable, in contrast to MEG's heavy and stationary magnet, which requires a shielding room [32]. Unfortunately, both electromagnetic modalities have no penetration depth, that is, all measurements only measure the surface of the scalp. Fortunately, radiation methods, both optical and non-optical, address this problem.

Positron Emission Tomography (PET), computerized tomography (CT) and functional magnetic resonance imaging (fMRI) are the traditional standards of radiation methodologies in neuroimaging. PET is a functional neuroimaging technique that works by detecting gamma rays from radioactive glucose that the brain is metabolizing, making it a functional technique. CT is a series of x-rays that penetrate the brain at multiple angles to form a composite image. The information it collects is purely structural. Although it can achieve about twice the spatial resolution of MRI at 500 μm, as opposed to 1 mm, CT has largely been replaced with MRI, because MRI uses radio frequency waves instead of the ionizing radiation used by CT [56]. Additionally, MRI can achieve about four times higher temporal resolution at 20-50 ms, and maintains higher contrast in soft tissues [60]. MRI is a structural technique but is combined with endogenous or exogenous tracers for use in functional applications, where it is then termed "fMRI". fMRI maintains millimeter to centimeter range spatial resolution in 3D pixels called voxels, but, depending on the tracers used, its temporal resolution worsens to several seconds. All of these non-optical radiation neuroimaging technologies are non-portable and expensive, but they have penetration depths that cover the entire brain [60].

An interesting intermediate between electromagnetic and radiation methods is sonic technology. Functional ultrasonic imaging (fUS) is the leading sonic technique in neuroimaging and is the basis for most other sonic techniques, such as photoacoustic tomography (PAT) [61]. fUS is a functional technique that uses ultrasonic waves to measure Cerebral Blood Volume (CBV) by considering the speed of sound through tissue, or blood flow by considering Doppler effects. fUS has been able to achieve a spatial resolution of 50-200 μm and a temporal resolution of 10-100 ms [61]. Ultrasound methods can image the full depth of the brain and can be reasonably portable and low-cost [62]. However, fUS relies on the presence of "bone windows" where the sonic waves can pass through the skull without adding too much noise to the signal. fUS also does not provide structural information other than depth, and it is often used as a free hand device that must be operated by an expert in cerebral vasculature, which causes significant variation in fUS signals [62]. Thus, despite excellent temporal and spatial resolution, fUS is not as common as fMRI, PET, or EEG.

These limitations force us to recognize that the utility of a technology is not only determined by technical parameters. Certainly, there are specifications that must be met, but more important questions are: What are you actually trying to measure? What part of space needs to be resolved? Does this technology resolve that space or a different space? Does this technology only resolve certain tissues in the brain? What time scale does the event of interest occur at? What practical requirements are met or not met by the technology? These questions are also at the center of considerations for neuroimaging technology in mobile application. For

example, large radiation and magnetic methods, such as MEG, MRI, and PET, could not be used in a study of runners or dancers in motion, whereas small portable technologies like EEG and fUS stand a better chance.

Non-optical technologies specifically considered for use as validation of TD-DCS with an expected agreement of 15% include the magnetic resonance based techniques TRUST (T2-Relaxation-Under-Spin-Tagging), ASL (Arterial Spin Labeling), SWI (susceptibility-weighted imaging), and PROM (Phase-based Regional Oxygen Metabolism), and other modalities, including PET and TCD (transcranial doppler ultrasound) [48]. Note that although MRI-based diffusion-weighted imaging sounds like it would produce similar results to DCS, it is actually measuring water moving through myelin sheaths and traditionally considers blood flow as noise [63].

3.2.2 Optical techniques

Optical imaging is nearly as varied as non-optical methods. Since the only requirement to be classified as an optical method is the measurement of photons, the term "optical imaging" includes visual techniques like surgery all the way to spectroscopic techniques for measuring absorbed or scattered light. In between there are fluorescence techniques for measuring emitted light, microscopy for measuring small amounts of light that are outside the resolution range of the unaided human eye, and cytometry for counting individual cells [64]. Invasive optical techniques such as light microscopy can image the brain on a neuronal or even dendridic scale, but these techniques fail to offer useful information about a conscious and active individual, as the subject should be unconscious and unable to perform tasks when their brain is exposed. Non-invasive optical techniques such as optical coherence tomography (OCT) and laser speckle contrast imaging (LSCI) tend to be limited to superficial layers of the scalp down to at most one millimeter but have temporal resolution on a millisecond scale and lateral spatial resolution on a submillimeter scale [56,65]. Furthermore, these techniques are interested primarily in blood flow, making them functional rather than structural techniques. Some non-invasive technologies take advantage of the transmission window in human tissue that occurs in the visual to near infrared wavelengths [55]. These include technologies like fNIRS and DCS, which are able to achieve penetration up to 1.5 centimeters with some cost to both temporal and spatial resolution [46,65,66]. Since the distance from the head surface to the cortical surface in humans is estimated to range from one to three centimeters, an optical method that is expected to provide information about the brain itself must have penetration depth of at least one centimeter [46]. Furthermore, fNIRS and DCS are lightweight and portable compared to non-optical radiation methods, like PET, CT, and MRI.

Functional near-infrared spectroscopy (fNIRS) is an optical technique that uses milliwatt-class lasers at different wavelengths in the tissue transmission window to determine the relative concentrations of oxygenated (or oxy-) hemoglobin (O_2Hb) and deoxygenated (or deoxy-) hemoglobin (HHb), thereby performing brain oxymetry [23]. These wavelengths are selected on either side of the isosbestic point, that is, the wavelength where O_2Hb and HHb have equal absorption coefficients, which occurs around 800nm [67]. By comparing the absorption effects at these two wavelengths an fNIRS operator independently measures the concentrations of O_2Hb and HHb in blood. These concentrations can be used to estimate CBV and changes in cerebral hemoglobin oxygen saturation (SO_2), which makes fNIRS a functional technique [31]. Because fNIRS is particularly relevant for DCS intermodality considerations, the four guiding equations for fNIRS are described below in Equations 3.23-3.26 [48].

Total hemoglobin concentration (HbT) can be calculated with the equation

$$HbT=HbO+HbR \tag{3.23}$$

where HbT is the total hemoglobin concentration (in g/dL), HbO is the cerebral concentration of O_2Hb (in g/dL), and HbR is the cerebral concentration of HHb (in g/dL). From this calculation, the total (or tissue) oxygen saturation (StO_2, in %, and sometimes simplified as SO_2) can be calculated using

$$StO_2 = HbO/HbT = w_aSaO_2+w_vSvO_2 \tag{3.24}$$

where SaO_2 is the arterial blood oxygenation (in %, and also known as the arteriolar hemoglobin oxygen saturation), measured by proxy with pulse oximetry; SvO_2 is the venous blood oxygenation (in %); w_a is the fNIRS sensitivity to arterial compartments, typically given a value of 15%; and w_v is the fNIRS sensitivity to venous compartments, typically given a value of 85%.

Building from this result, the oxygen extraction fraction (OEF) can be calculated as

$$OEF = (SaO_2-SvO_2)/SaO_2 \tag{3.25}$$

as well as the cerebral blood volume (CBV), given by

$$CBV = HbT.MW_{Hb}/(HGB.D_{bt}) \tag{3.26}$$

where MW_{Hb} is the molecular weight of hemoglobin, typically given a value of 64,500 g/Mol, D_{bt} is the brain tissue density, typically given a value of 1.05 g/mL, and HGB is the hemoglobin concentration in the blood (in g/dL) [48].

Since oxygenation is a biomarker for ischemic conditions, fNIRS has the potential to inform diagnostic decisions on conditions such as stroke, traumatic brain injury (TBI), and shock. Oxygenation measurements have also been shown to

correlate well with results from blood oxygen level-dependent (BOLD) fMRI during both sensorimotor activations and visual stimulations [28]. But unlike fMRI, fNIRS has been made into commercially available wearable systems, such as NIRx Sport, and its cost is in the thousands rather than the millions [32,68].

One modification of fNIRS called time domain fNIRS (TD-fNIRS) uses a series of laser pulses rather than a continuous wave source to take these measurements, allowing for estimation of tissue optical properties by considering time of flight (ToF) and the temporal point spread function (TPSF) [46,47]. By estimating these optical properties, TD-fNIRS is able to construct absolute measurements of absorption changes among different regions of the scalp, while traditional continuous wave fNIRS is only designed to take relative measurements [46]. TD-fNIRS has spatial resolution on the order of centimeters and temporal resolution on the order of deciseconds [32]. However, TD-fNIRS only has a penetration depth of approximately one centimeter, depending on the source-detector separation, laser power, and selective detector gating for late photons [46]. This means TD-fNIRS measurements reach only the surface of the brain, though efforts are being made at MITLL and elsewhere to improve penetration depth for fNIRS technologies.

Other optical techniques that are similar to DCS include spatial frequency-domain imaging (SFDI) [43], and laser speckle imaging (LSI) [24] and the combined modality. As with DCS, these modalities measure flow and optical properties. Unlike DCS, however, the photon paths do not reach depths where they are fully randomized [69]. Another interesting modality adds to DCS by using US to selectively modulate the optical properties of deep tissues with the acousto-optic effect, effectively tagging photons that pass through the modulated regions, thus improving depth sensitivity [70,71].

Time-domain diffuse correlation spectroscopy (TD-DCS) itself has penetration depth of approximately 1 cm, spatial resolution of about 0.5 mm, and temporal resolution down to 10 ms [65]. However, due to high noise and very low photon throughput, TD-DCS measurements usually need to be averaged over a larger acquisition time window [72]. The Martinos Center has demonstrated that TD-DCS can be made portable, and the cost of a TD-DCS system is much below that of fMRI. Furthermore, since fNIRS and TD-DCS can share much of the same acquisition equipment, the cost of a gated TD-DCS system is comparable to that of an fNIRS or TD-DCS system alone. In conclusion, gated TD-DCS is a functional brain imaging technology that is portable, low-cost, and fares reasonably well in penetration depth, and temporal and spatial resolution.

Chapter 4

Instrumentation and validation of the optical neuroimaging test bed

The gated TD-DCS test bed has four primary components: the source, the detector, the time controller, and the diffuse medium. Other components include optical and electrical items between the above, oscilloscopes, function generators, power meters, and spectrum analyzers. Building the test bed required (1) design or procurement, (2) assembly, and (3) validation of operation for each component. Additionally, the setup as a whole needed to be evaluated.

The validation procedures that I implemented include several for baseline operation, that is, DCS operation without gating the detectors, as well as preparations for gated operation. Baseline operation validation procedures include (1) laser bandwidth and operation voltage measurements, (2) laser amplification validation, (3) detector collimation adjustments, and (4) time controller data processing development and evaluation. Planned validation procedures for gated detector operation include (1) gate and laser synchronization, (2) time controller data processing development and evaluation for gated operation, (3) improved depth resolution validation and comparison with manual "time-gating scheme" used in [31], and (4) determination of after-pulsing (AP) levels in gated detectors using correlation measurements with a split fiber.

This section steps through the gated TD-DCS test bed development by first considering assembly and the system as a whole, then breaking it down into the four primary components including a section for the miscellaneous components. The breakdown of each component will discuss the design—or, for initial setup, procurement—requirements for each component and the procedures used to evaluate their operation. Validation procedures expected to be performed in the future of the test bed will also be mentioned.

4.1 Test bed overview and assembly

The gated TD-DCS research performed at Massachusetts Institute of Technology Lincoln Laboratory (MITLL) and the Massachusetts General Hospital (MGH) Martinos Center for Biomedical Imaging aims to produce a portable and ultimately wearable system for functional brain imaging of blood flow. Additionally, the system in development intends to build from the success of functional near infrared spectroscopy (fNIRS) to eventually produce a dual-modality system that will simultaneously measure blood volume and blood oxygenation [51].

The test bed that I set up at MITLL is directed towards these goals by focusing on the development of gated detectors, which MITLL has experience developing for applications including terrain mapping and disaster relief [73]. Since my setup focuses solely on the detector development, portability was discounted in favor of a simple tabletop arrangement with commercial off the shelf (COTS) components standing in as a baseline for later comparison with fabricated parts. To facilitate the evaluation of several different detector designs, the test bed is modular in nature such that components can be easily exchanged according to the detector operation specifications. For example, a detector designed for one range of wavelengths will require a different illumination source than a detector designed for another range of wavelengths, and the test bed must be able to accommodate that change. Particularly with a modular design, much of the test bed development comes from the establishment of standard operating procedures (SOPs) that facilitate comparison between different versions of the test bed. The first set of SOPs developed for the test bed are included in Appendix C. Note that each 'module' has its own set of test bed-specific operating procedures. Additionally, subsets of procedures are provided when certain combinations of modules require adjusted operating procedures.

Assembly

The gated TD-DCS test bed has four fundamental components, whose tasks can be performed by certain replaceable modules. The first component is the illumination source, which sends photons into the diffuse medium to ultimately be measured by the detector. The diffuse medium and the detector are the next two components, which diffuse the photons and detect some of the photons, respectively. The fourth fundamental component is the time correlator, which keeps track of time and synchronization between the source and the detector, and records the measurement. In practice the test bed also requires a computer, to program components and process the data. This conceptual flow is illustrated in Figure 4-1.

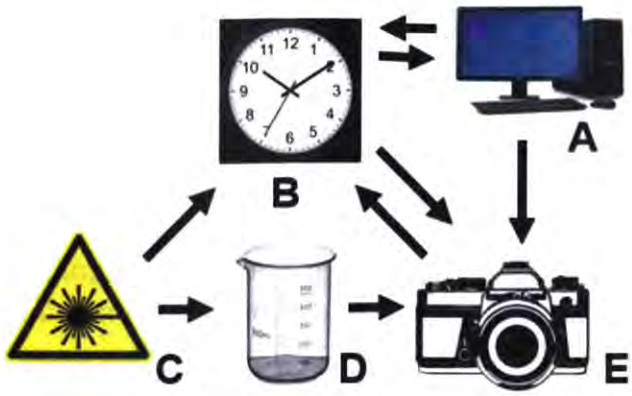

Figure 4-1: Simplified schematic of the test bed setup. A computer (A) stores data and interfaces with the software of the time controller (B) and the detector (E) to program operation. The time controller (B) receives the synchronization pulse from the source (C), which it uses to trigger the detector gate (E). The source travels through the sample (D) to the detector (E). A detection pulse is then sent from the detector (E) to the time controller (B) which records timestamps both from the start of the measurement as well as time of flight (TOF) estimated by the relative time of the detection from the last laser pulse. This data is sent to the computer (A) for further processing.

One example of the test bed setup is shown in Figure 4-2 below. In this assembly, the computer is a Windows 7 machine with software to program and interface with both the detector and the time correlator. The Lumics laser (LU0786M100-1G06E10A) is a butterfly diode pulsed with a PicoLAS BFS-VRM-03HP driver board using a 10dB attenuated 1.9V signal with 1.6ns pulse width originating from a SRS DG 645 delay generator, as triggered by a 1MHz SRS CG 635 clock signal. Both optical and electrical connections are required in this setup. Single-mode fibers are required leading to the detector, in order to collect only a single speckle. The setup in Figure 4-2 was used for collecting the first timestamps from the test bed using human adipose tissue as the diffusive medium.

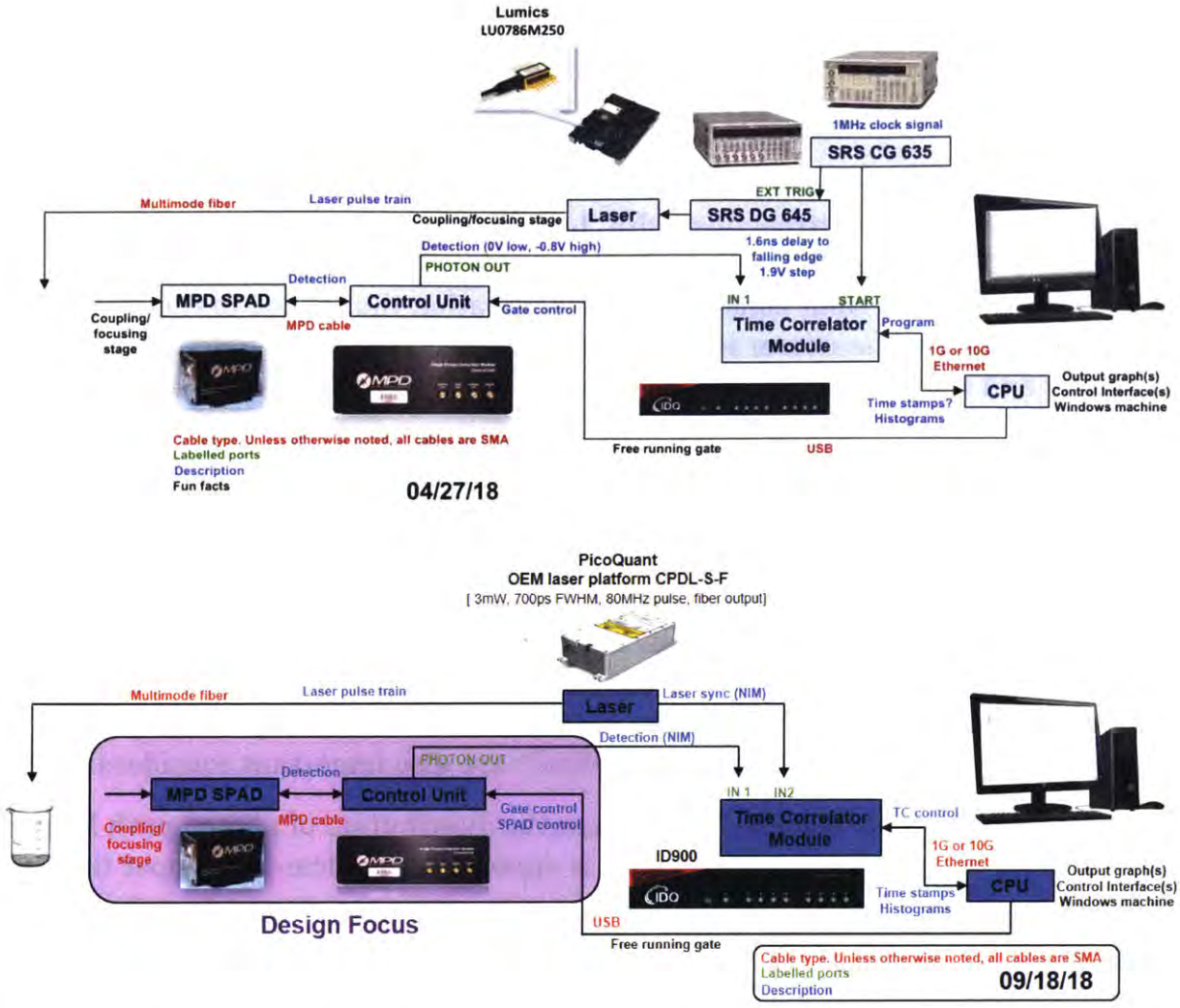

Figure 4-2: Gated TD-DCS test bed setup. Two examples are shown where various components are exchanged with other equipment according to the requirements of the test. The underlying structure of the test bed in both cases is traceable back to the heuristic model in Figure 4-1. Note that this figure uses a multimode fiber from the source, and that while either a multimode or single-mode fiber can be used at the source, only a single-mode fiber should be used to couple to the detector.

To meet the standards for test bed validation, analyses must be developed that can find agreement between theoretical, experimental, and modeling approaches. As with any large project, piecemeal validation techniques for each component are important for ensuring proper operation and debugging the test bed; however, note that the most valuable test of the system will be an overall test of the interconnected system. Therefore several completed, passed over, and planned

validation techniques for the test bed are discussed by component and then at the system level in Section 4.5.

4.2 Illumination source

The illumination source is by necessity a laser in the current state of technology as coherent, narrow linewidth, high-power, pulsed light is required for a meaningful TD-DCS signal. Coherent light is made of photon plane waves of the same wavelength with some constant phase separation that is due to the optical path length from each scatterer to the point, such that the interference patterns are temporally and spatially constant [74]. This type of light enables speckle patterns [75]. Narrow linewidth means nearly all of the energy in the laser is focused on a single frequency.

4.2.1 Criteria for source design and procurement

In addition to meeting requirements, the laser used in the gated TD-DCS test bed is expected to respect certain measures of merit. These measures include coherence length, linewidth, power, pulse duration, repetition rate, pulse shape, wavelength, and maturity of technology. Of course, cost, ease of operability and integration, and size, weight and power (SWaP) are also important considerations.

Coherence length must be longer than the distribution of photon path lengths [24], which for neuroimaging applications is approximately 4cm. The upper limit of coherence length can be calculated as

$$L_{coh} = \frac{c}{\pi \Delta \nu} \tag{4.1}$$

where c is the speed of light in a vacuum in $\mathrm{m} \cdot \mathrm{s}^{-1}$, and $\Delta\nu$ is the linewidth of the laser in Hz. It is often expressed in terms of the wavelength bandwidth through the approximate relationship

$$\Delta \nu \sim \frac{c}{\lambda^2} \Delta\lambda \tag{4.2}$$

where c is the speed of light in a vacuum in $\mathrm{m} \cdot \mathrm{s}^{-1}$, and $\Delta\lambda$ is the wavelength bandwidth of the laser in m and λ is the center frequency. This approximation is valid for small $\Delta\lambda$. Coherence length, L_{coh}, has units of meters and from Equation 4.2 is sometimes approximated as $\lambda^2/\Delta\lambda$. Linewidth should be as narrow as possible, to best approximate an impulse in the frequency domain. However, since we are also trying to have as short a pulse duration as possible in the time domain, to approximate an impulse, there is an unavoidable tradeoff. As width decreases in the frequency domain, duration increases in the time domain and vice versa. This limit where the spectral width is as narrow as possible for a given pulse duration is known as the transform limit, or Fourier limit [76]. An ideal pulse shape of $\mathrm{sech}^2(t)$ is desired as it would ensure the pulse is nearly transform limited [77]. The tradeoff

ought to be explored in more detail as it may be that absorption losses in the tissue are high enough that attenuation of incoherent light at later arrival times is not a limiting source of noise [78]. Assuming a transform limited source, the minimum pulse duration can be calculated as

$$\Delta t = \frac{\pi 0.315 L_{coh}}{c} \tag{4.3}$$

where the 0.315 comes from the time-bandwidth product of $\mathrm{sech}^2(t)$ pulses. Using Equation 4.1 with an ideal source gives an absolute maximum linewidth of 1.9GHz for a 5cm coherence length, and with Equation 4.2 the minimum pulse duration is calculated as 165ps.

Power should be as high as possible within American National Standards Institute (ANSI) limits to give the signal the best chance of overcoming noise sources and therefore improve the signal-to-noise ratio. These limits are approximately 25mW at 765nm and 100mW at 1064nm in terms of average power [79]. Limited power also ensures that thermal influences of the laser light do not distort the measurement by affecting blood flow in the tissue. Another factor in combating noise is a high repetition rate. Higher repetition rates decrease the integration time needed to produce a viable signal and as a result increase the temporal resolution of the measurements. The repetition rate is limited by the decay time of the temporal point spread function (TPSF) (i.e., the signal), which is approximately 3ns. Typically, our team has estimated this limit conservatively as 10ns, resulting in a 100MHz maximum repetition rate.

The desired wavelength of the laser for TD-DCS is anywhere in a transmission window for tissue. However, for a TD-DCS system capable for integration with functional near infrared spectroscopy (fNIRS), it is important to validate operation at wavelengths on either side of the 805nm isosbestic point of oxy- and deoxy-hemoglobin. Maturity of technology enables access to decades of research in other disciplines, and is a way to avoid falling down a rabbit hole in laser design. To this end, our team has filed a patent application for the use of 1064nm lasers for use in fNIRS and DCS, since this wavelength is in an optical transmission window for tissue [80] and can still provide useful data on the oxy-hemoglobin side of the isosbestic point [36]. It was first considered by our team due to its ability to be used with efficient Ytterbium fiber amplifiers [81].

As with the system as a whole, the size, weight, and power (SWaP) and costs should be minimized in laser selection and design. To this end, the team has been considering the use of Vertical-Cavity Surface-Emitting Lasers (VCSELs), which are small and inexpensive semiconductor devices that can be embedded into optodes for application to the skull. One significant problem with this approach is the low power output of these devices. Note that the VCSEL approach is an example of a

distributed source. Like the detectors, both split monolithic devices and site-specific sources are under consideration. Site-specific sources would be easier to replace and also eliminate the additional weight and design constraints of fibers and coupling, but monolithic sources are more readily able to meet power requirements.

One example of a monolithic source that would need to be split to deliver light to all sites is the laser currently used in the Martinos Center setup. It is a high powered device, known as the PicoQuant Vis-IR Stimulated Emission Depletion (STED), operating at 765nm with 550ps FWHM and 1.5W operation, and was not considered cost effective for acquisition in the MITLL setup. This decision was further supported by the idea that as collaborators, if MITLL had any need to test with the Martinos Center laser, they would be able to borrow the device.

Other options under consideration are summarized in Table 4.1 below. All reported values are approximate and vary considerably based on the specific device. The numbers are intended only to provide ballpark figures. Unknown quantities are left blank. These are representative of the laser options considered by the team, and included (1) a high-power gain switched diode, (2) a tapered amplifier using gain switching and an amplified spontaneous emission (ASE) filter, (3) a tapered amplifier using continuous wave seed chopping and ASE rejection, (4) VCSELs, (5) Vertical External-Cavity Surface-Emitting Lasers (VECSELs), (6) frequency doubling fiber with the Vis-IR STED, (7) a titanium-sapphire laser using continuous wave seed chopping and a tapered amplifier, and (8) mode-locked lasers.

Table 4.1 Qualitative Comparison of Various Laser Options

Parameter	Goal	VCSEL array	VECSEL array	Gain switched semiconductor	Ti:Saph Amplifier	Mode-locked laser	Edge-emitting diode
L_{coh} (cm)	5	Could work	Needs work	Needs work	>5	>5	
Linewidth (Hz)	Low	10s of kHz					
Power (mW)	100	0.5/element	500 @ CW	10-100 (peak)	20W	>100	100**
Pulse width (ps)	165	<10ns		100		500	
Repetition rate (MHz)	100				<100MHz	100MHz*	
Pulse shape	$\text{sech}^2(t)$	Good	Needs work	Good	Good	Good	
Wavelength (nm)	750-1064	750-980+		Many	Many	Many	
Maturity of technology	High	Adequate	Low			Hard to develop	High

Cost	Low	Low					Average
SWaP	Low	Low		Low	High	High	
Monolithic/ Distributed	Either	Dist.	Dist.	Dist.	Mono.	Mono.	Mono.

*achievable but requires a 1.5m cavity
**with single amplification stage

At Lincoln Laboratory, the decision was made to start with a simple approach: a Lumics butterfly package laser diode at 786nm (LU0786M100-1G06E10A). During the laboratory setup, I also found a pair of 1064nm QPhotonics butterfly package laser diodes (QFBGLD-1060-20PM) in a cabinet that we decided were worth considering. PicoLAS BFS-VRM-03HP laser diode drivers are used to operate the laser diodes at repetition rates from continuous wave up to 1MHz. Spectrum measurements with the QPhotonics diode that was in better physical condition indicated that the cabinet-sourced diodes were probably not in good operating condition and were therefore replaced by an Eagleyard butterfly package distributed feedback laser (DFB) diode (EYP-DFB-1064-1500-BFY2-0010) at 1064nm. An Oclaro butterfly package laser diode (LC96A1064BBFBG-20R) at 1064nm was also considered for integration into the TD-DCS test bed; it has a higher wavelength bandwidth than the Eagleyard, at 900nm instead of 200nm, and a higher continuous-wave operating power, at 350mW instead of 40mW. All butterfly diodes would use the same PicoLAS BFS-VRM-03HP laser diode driver as interfaced through the PicoLAS PLB-21 user control unit. These butterfly packages are fairly low power and are not designed for short and fast pulsing. The details of the measurements made to quantify these limitations are described in Section 4.2.2. We also ordered an Original Equipment Manufacturer (OEM) laser platform from PicoQuant that produces a 3mW 1064nm wavelength <700ps full-width half-maximum (FWHM) pulse at 80MHz. An amplification stage was also useful for operation of this device.

The amplification stage we developed uses a Cybel Mantaray-27-BT-CW-PM single-stage amplifier added between the 1064nm sources and the diffusive medium. The amplifier is only suitable for the 1064nm sources and for amplification up to 500mW, and amplifiers at 786nm would need to be custom built. To work around this, our team is considering using a 530nm laser, which can be amplified and then doubled such that it meets the criteria for wavelength sources at either side of the isosbestic point of oxy- and deoxy-hemoglobin. The validity of this approach has yet to be explored in greater detail.

4.2.2 Source validation results

The first step to getting the butterfly diodes working was to install them into the laser diode driver, which required precision soldering. Care was taken to avoid applying undue amounts of heat to the device. The diodes were also screwed in place and the leads cut. Since the diodes were designed primarily for continuous-wave operation, we needed to be careful about how much current was flowing through the device during pulsed operation. We used the current-voltage characteristic plot in the PicoLAS driver manual to determine the maximum input voltage to the driver that would result in the maximum allowable current through the diode. For example, the Eagleyard diode has a maximum pulse forward current of 1.5A which corresponds to a PicoLAS driver pulsed voltage input of 600mV.

Next we estimated coherence length using Equations 4.1 and 4.2 with the bandwidth of lasers as measured with an Ando AQ6317B optical spectrum analyzer. For the Lumics laser this was estimated as 2.05cm, for the Eagleyard laser this was estimated as 5.96cm, and for the PicoQuant laser this was estimated as 5.56cm. This contrasts with the estimates using the quantities in the specification sheets which for the Lumics laser was estimated as 1.23cm, for the Eagleyard laser was estimated as 15cm, and for the PicoQuant laser was estimated as 11.3cm [82]. The specification sheet approximations were made using the ideal operating conditions and the simplified equation for linewidth, $\lambda^2/\Delta\lambda$, or in the case of the Eagleyard laser, $c/\Delta v$ (where Δv is the spectral width in MHz). Small differences in the spectral width, which was only measured to two significant figures and was on the order of picometers, had a strong effect on the estimated coherence length. This partially explains the differences between the two coherence length estimation methods. A screenshot of the Lumics laser spectrum analyzer measurement is shown in Figure 4-3. Using the spectrum analyzer also gave us a measurement of the center frequency, which was 786nm for the Lumics laser, 1064nm for the Eagleyard laser, and 1063nm for the PicoQuant laser. The Eagleyard laser diode was also demonstrated to have a wavelength tunable between 1063.5nm and 1065.5nm using thermoelectric cooler (TEC) settings from 10°C to 50°C.

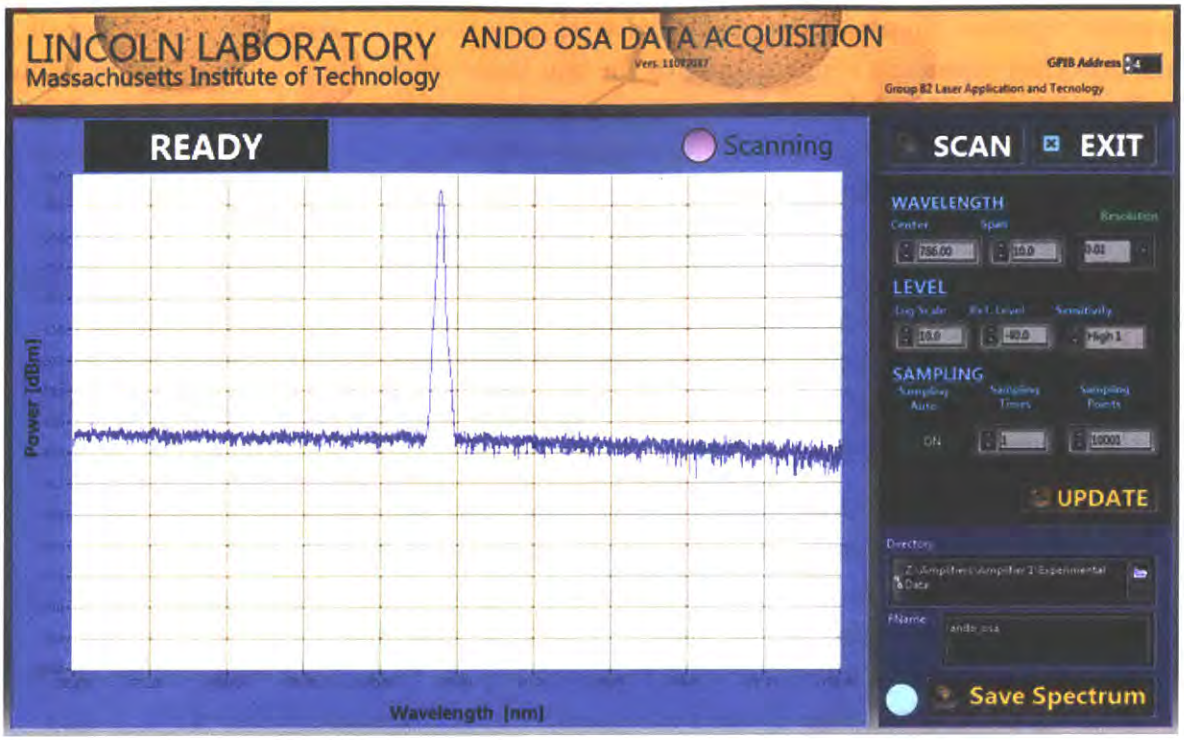

Figure 4-3: Pulsed laser diode (786nm Lumics LU0786M100-1G06E10A with PicoLAS BFS-VRM-03HP driver) **spectrum analysis screenshot**.

Because the coherence length is so important to DCS, it was also measured using interferometry, which is a more direct measurement of coherence length. This setup required a splitter that sent the light to two reflectors, one of which was situated on a motor that varied pathlength as a function of time. The light then would reflect off the two mirrors and recombine to focus on a detector. Analysis was performed to determine when the constant phase difference assumption was lost as a function of pathlength difference between the split light.

Average power was measured using a ThorLabs PM100D power meter and ThorLabs S305C detection head. Pulse length and pulse rate were monitored using an oscilloscope and Thorlabs detectors. A Thorlabs DET08CFC InGaAs 5GHz detector was used for the 1064nm lasers and a Thorlabs DET025 Silicon 2GHz detector was used for the 786nm laser. The PicoQuant laser has immutable pulse-shaping, but the laser diodes can be driven with an arbitrary waveform generator. An initial square wave pulse operation was developed using a Stanford Research Systems (SRS) Clock Generator (CG) 635 driving a SRS Delay Generator (DG) 645. The repetition rate is determined by the CG and the amplitude and duty cycle are determined by the DG. The narrowest pulse duration under admissible operation conditions for the Lumics, QPhotonics and Eagleyard laser diodes was found to be approximately 600ps, created using a 10dB attenuated 1.9V output from the delay

generator into the PicoLAS driver board with a delay time from the clock edge of 1.6ns. Another common repetition rate for the laser diodes is 200kHz, which is more friendly to the PicoLAS driver, which has a maximum driving rate of 1MHz. It is very important to decrease the voltage before widening the pulse duration, to avoid irreparable damage to the laser diodes. After these baseline measurements with square pulses, we used a Chase Scientific DAx14000-4M Arbitrary Waveform Generator programmed with an MITLL-developed LabView interface to experiment with cleaner pulses. There is much potential in pulse shaping that should be pursued further, as with only a few minutes of trial-and-error we were able to use pulse shaping to eliminate the oscillatory optical outputs that sometimes resulted from the square driver input pulses.

Continuous-wave operation was evaluated for the Eagleyard laser by incrementing the input voltage to the driver and measuring the power at the output. These results are shown in Figure 4-4. Notice that the threshold occurs at approximately 15mV input to the driver. This test was also performed on the QPhotonics laser and it never seemed to make it past threshold, even at its specified maximum operating voltage. Based on this result, we discarded the QPhotonics laser in favor of the Eagleyard laser, as it has similar specifications and also operates at 1064nm.

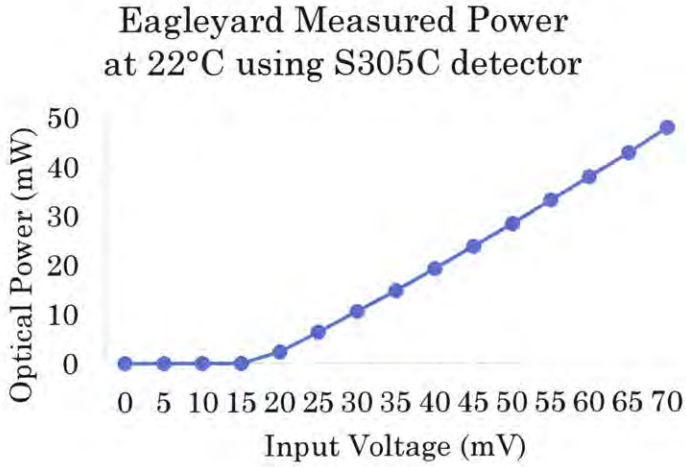

Figure 4-4: Input voltage-output power characteristic for the Eagleyard EYP-DFB-1064-1500-BFY2-0010 laser diode with the PicoLAS BFS-VRM-03HP driver.

Continuous-wave amplification operation was evaluated for the PicoQuant OEM CPDL-S-F laser by incrementing the current setting of the amplifier and measuring the power at the output. These results are shown in Figure 4-4. Notice

that the amplifier threshold is reached at approximately 200 device-defined current counts (~831mA) to the amplifier for the PicoQuant laser.

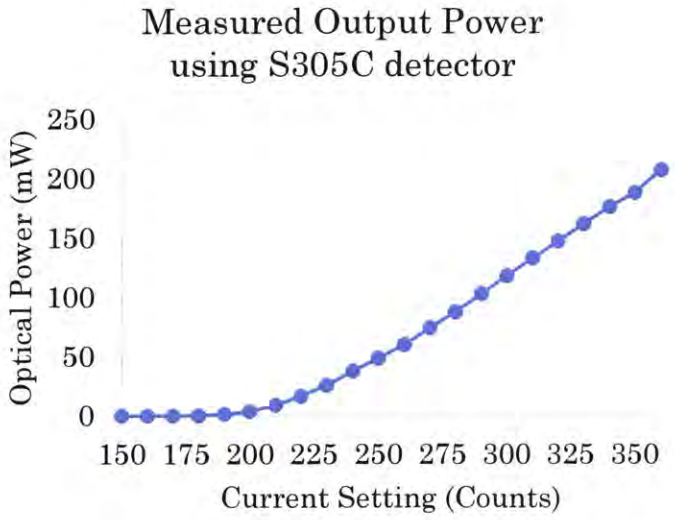

Figure 4-4: Cybel Mantaray fiber amplifier operation with PicoQuant OEM CPDL-S-F 650ps pulsewidth 80MHz repetition rate (4.5mW average power) as a seed.

Another key test of the laser system was the shortening of the PicoQuant laser output pulse duration using an Eospace intensity modulator. Shorter pulses of about 320ps pulse duration were attained. The coherence length of this output was measured using the interferometry-type setup described earlier and determined to be 5.08cm. Our team was able to demonstrate halving of the pulse duration without shortening the coherence length too much [83].

The Eagleyard laser with the PicoLAS driver, as well as the PicoQuant OEM laser, have been operated successfully by the Martinos Center on their own projects.

4.2.3 Future source validation steps

One area of development for the laser is finding a viable sub-805nm source. In addition to the PicoQuant Vis-IR STED laser, the Martinos Center has looked into the 760nm LDH-D-C Picoquant laser, which has a lower power at 7mW and 100ps pulses, and the 765nm Vis-IR PicoQuant with 400mW average power and 70ps pulses. These lasers operate below the minimum pulse duration, and could be used to interrogate the effects of limited coherence within the decay window of the temporal point spread function (TPSF) of TD-DCS. These effects of finite coherence length can be tested against theory from Cheng et al. [29].

Another future step in laser validation will be the amplification and splitting potential in the monolithic devices currently in use. This analysis will need to consider coupling and splitting losses, fiber weight, and output characteristics like coherence length, wavelength, and power. A start would be to use a single splitting stage and then try more and more until the design criteria are met. It would also be helpful to find the theoretical maximum number of splitters for given input power splitting losses, and coupling losses. This could also be used for the inverse problem of finding the minimum power required for a given number of splitters.

4.3 Gated Single-Photon Avalanche Detectors (SPADs)

Single-photon detection has been approached in multiple ways, from classical vacuum-based examples like photomultiplier tubes (PMTs), which are used in computed tomography (CT) imaging [84], and positron emission tomography (PET) [85], to more recent techniques like superconducting nanowire detectors [86,87]. The test bed developed at MITLL was created specifically to aid in the design of Geiger-mode avalanche photodiodes (GmAPDs), also known as single-photon avalanche detectors (SPADs).

Single-photon avalanche detectors (SPADs) are semiconductor devices doped to have some diode structure. Detecting at a specific wavelength requires certain absorption properties in the semiconductor, which in turn determines which materials can be used to achieve a certain photon detection efficiency (PDE). For reference, common materials in this field include silicon (Si), indium phosphide (InP), and indium gallium arsenide (InGaAs). The SPAD is reverse biased above a device-dependent breakdown voltage so that impact ionization from a carrier generated by an incoming photon results in avalanche multiplication and high current through the device. This event is known as breakdown. This phenomenon is in contrast to breakdown triggered by quantum tunneling, known as the Zener effect, when the depletion region of the diode is heavily doped and therefore thin enough such that there is a non-negligible chance of quantum tunneling from the valence band to the conduction band. Avalanche breakdown occurs at higher voltages than Zener-effect breakdowns because more energy is needed to accelerate the electrons sufficiently to produce the avalanche effect [88,89,90]. These two types of breakdown are illustrated in Figure 4-6.

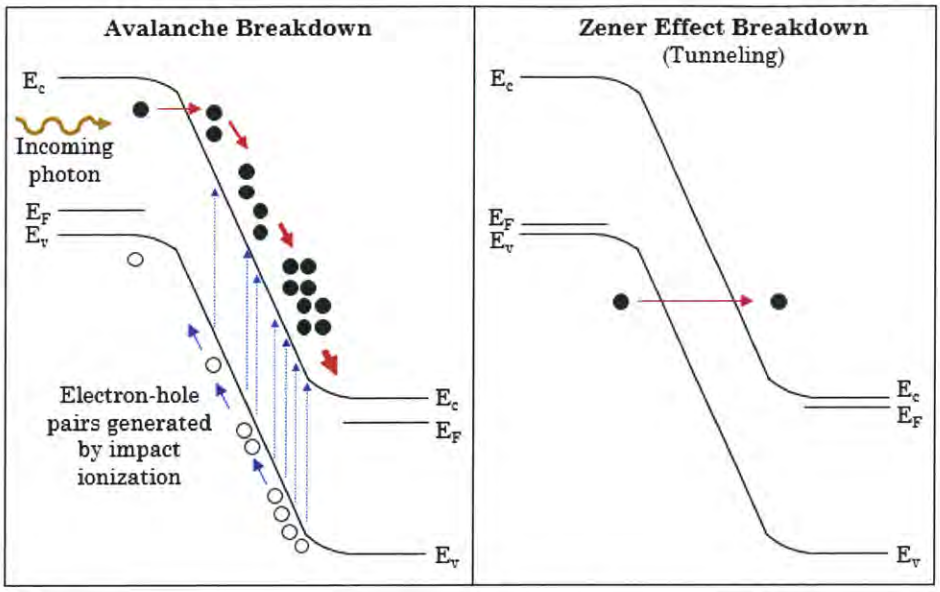

Figure 4-6: Breakdown conditions in diodes. Energy band diagrams for avalanche breakdown (left) and Zener-effect breakdown (right). Although an electron avalanche is shown, note that both electrons (solid circles) and holes (rings) can create impact ionization [91].

The strong current produced by the avalanche can be quenched either actively or passively. In passive quenching, a series resistor is used to bring the voltage below breakdown. This can be too slow for some applications, so active quenching has also been developed. Active quenching works using a sensing resistor that detects an avalanche and triggers an active circuit to respond by bringing down the voltage for a set holdoff time before resetting [92].

In addition to using active circuits for quenching, alternating between operating voltages above and just below breakdown enables SPADs to operate with gated detection. This allows the user to be temporally selective about which photons to detect. The gate is typically repeated at a set frequency with a specified duty cycle. The length of time for which the detector is "on" per cycle is referred to as the gate width. When an avalanche occurs, the holdoff circuitry takes priority over the gate, and the detector will be returned to operation voltage at the next rising edge of the gate clock after the holdoff time. A typical signal set for a gated SPAD is shown in Figure 4-7.

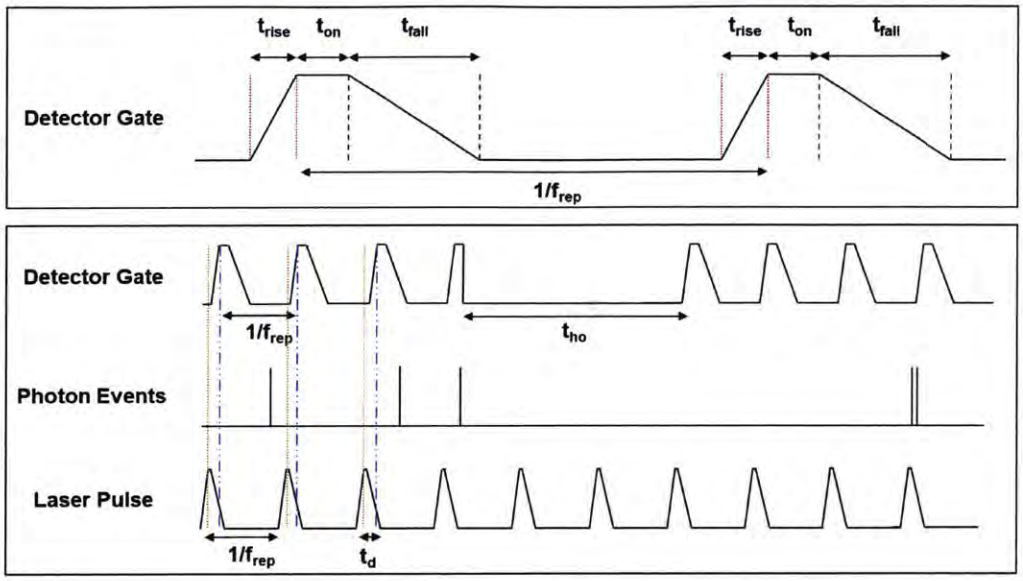

Figure 4-7: Typical signal set for gated SPAD operation. In this signal set, t_{rise} is the detector gate rise time, t_{on} is the gate width, t_{fall} is the gate fall time, f_{rep} is the laser pulse frequency, t_{ho} is the detector hold off time, and t_d is the delay time between the laser pulse and the gate window.

There are several non-idealities to contend with in SPAD design. Figure 4-7 illustrates finite rise and fall times for the detector. There are also problems associated with premature breakdown at junction edges where field lines are concentrated. Fortunately, premature breakdown probability can be reduced by increasing the radius of curvature at the junction edges or adding a guard ring to the device [93,94].

The two main sources of noise in the detectors are dark counts and afterpulsing. Dark counts result from thermal generation and field-enhanced generation, which are caused by the tunneling of carriers in the depletion region. Dark counts can be reduced by cooling the device and using lower voltages above breakdown. While detection efficiency increases with higher voltages above breakdown, the efficiency improves at a slower rate than the dark count rate increases, so there is an application-specific tradeoff between noise and detection efficiency [89]. Afterpulsing is caused by carriers that get trapped at defects in the multiplication region. When the voltage is increased back to breakdown voltage, these carriers can be ejected from the traps and cause an avalanche.

In contrast to dark counts, afterpulsing decreases with increased temperature as higher kinetic energy in the system provides more opportunities for the carriers to escape while the detector is biased below breakdown. Another way to reduce afterpulsing is to use a longer holdoff time since it gives trapped carriers

more opportunity to escape. The holdoff time is typically set to meet a certain threshold percent chance of afterpulsing. A final way of reducing afterpulsing is fast quenching, which reduces the current so carriers have a smaller probability of finding traps—also known as deep levels. Different gating strategies, such as sinusoidal gating [95], try to reduce these quenching times to increase repetition rate without losing as much signal to afterpulsing. Properly dealing with afterpulsing is especially important, as afterpulsing is a self-propagating problem [89,96].

4.3.1 Criteria for detector design and procurement

Detectors used in a gated TD-DCS setup must meet certain criteria in order to be effective. For SPADs, the measures of merit include photon detection efficiency (PDE), dark count rate (DCR), afterpulsing probability (APP), repetition rate, gate rise time, timing jitter, gate width, and wavelength. High PDE is important because it enables the signal to be further from the noise floor for lower light power. Since the American National Standards Institute (ANSI) limits laser power in medical devices, it is critical to be as efficient as possible with photon detection. DCR and APP must be low, as they are noise sources. Higher repetition rates are desired for faster integration time and shorter overall experiment time. Faster gate rise time and smaller timing jitter decrease ambiguity in the measurement. Smaller gate width allows the user to be more selective in detecting later photons. Detectors must be sensitive to the wavelengths of interest, which are in the range 750-1064nm, in the near infrared.

The goal parameters along with the actual parameters of several candidate SPADs are shown in Table 4.2 [51,97]. Unknown quantities are left blank. Note that the given numbers are approximations, and differ based on the device. Other important parameters not listed include size, weight and power (SWaP), cost, and ease of operation and integration.

Table 4.2 Comparison of Various Available SPADs

Parameter	Goal	Excelitas SPCM-NIR-14	MPD-InGaAs/InP	MPD - Si Fast Gated	IDQ—ID230 InGaAs/InP	MITLL Si APD	MITLL InP APD
PDE (%)	High	70 @ 780nm	30 @ 1064nm	5 @ 800nm	10 @ 1064nm		40 @ 1064nm
DCR (cps)	<100	100	>1000	50	100	100	2-34k
AP (%, decay)	<<1%, <1μs	<3%	<5%	<1%	<5%		1%
t_{ho} (μs)	<1μs	20-40ns	1-3'000	50-500	2-100		1.6

Timing jitter (ps FWHM)	<100	350	100	50	100		500
f_{rep} (MHz)	50-80		0-133	0-80			
t_{rise} (ps)	100-250		700	100-200		1ns	
t_{on} (ns)	200-500ps		1.5-500	2-500			4-10
t_{fall} (ps)	300-500		700			1μs quench	1.25μs quench
Wavelength (nm)	600-1200	600-900	950-1600	400-800	900-1700	400-900	1060 or 1030
Active area width (μm)	Any	180	50	50		25 pitch	5-15

For the initial laboratory setup, our goal was to mimic the test bed at the Massachusetts General Hospital (MGH) Martinos Center for Biomedical Imaging, which was used for the first demonstration of TD-DCS [31]. To this end, we purchased two of the same detectors that would also be used there. These devices are silicon fast-gated single-photon avalanche detectors (SPADs) manufactured by Micro Photon Devices (MPD), and their specifications are listed in Table 4.2. These detectors have peak detection efficiency of 50% at 400nm wavelengths, trailing off to 4% by 800nm. Even with such low efficiency at the wavelengths of interest, which are in the 750-1060nm range, the MPD SPADs are considered capable of standing in for a more suitable detector to be developed at MITLL. This is an assumption that must be explored in more detail when validating equipment.

Other detectors considered for the initial baseline setup included the ID Quantique ID100, ID120, and ID110. Unlike the comparably performing ID100, the MPD module can be used with a picosecond delay circuit, which will allow our team to significantly improve the signal-to-noise ratio in our measurement with fast gating relative to the laser pulses. The ID120 had a much better detection efficiency at the wavelengths of interest (around 60% at 850nm), which at the time were limited to 760-850nm, but unacceptably high timing jitter (400ps) and gate width (25ns). The ID110 looked promising at first but the Martinos center, which had tested the ID110 on their system, relayed that the ID110 was unable to provide adequate signal-to-noise ratio for the application. This comparison highlights the need for custom detectors.

Moving forward into the design phase, three paths were considered: (1) building from existing designs and expertise within Lincoln Laboratory using the Highly Efficient Counting and Timing Integrated Circuit (HECTIC) SPAD, (2)

focusing on minimizing quench time with sinusoidal gating [95], and (3) designing for reduced afterpulsing with a macropixel design, which allows for holdoff time to be maintained at a faster effective repetition rate by using multiple detectors per pixel [98].

Additionally, since the final gated TD-DCS system is eventually expected to operate at dozens of sites on the scalp simultaneously, two types of multi-detector implementations were considered: (1) one consolidated array and (2) several distributed arrays, or even individual pixels. Implementation 1 would be a consolidated chip with fibers connecting each detection site on the head to the corresponding pixel. The distributed design is to have each detector separate and closer to the detection site. The monolithic design is simpler from a chip design perspective, as only one power distribution system is required and Lincoln already has significant experience in large photodiode arrays [99]. The distributed design has greater potential for portability and medical operability, as large numbers of long fibers would be unpleasantly heavy for some patients.

4.3.2 Detector validation results

At this point, the detector has only been validated with the most rudimentary tests. The first is that it is able to turn on and off. The second is that it is able to interface with the software that turns on and off detection, including bias voltage and thermoelectric cooler (TEC) controls. These initial tests were performed by following the guidelines in the user manual after making appropriate connections from the detector control module to power, the computer, and the detection head, and then observing the binary variable of whether or not the system responded to input. The third test is that it returns output pulses according to the light intensity. This was tested by observing pulses per second as recorded by the time correlator when the detection head was covered or uncovered in the presence of ambient light. While covered, the count rate was nearly at the specified dark count rate of the device. While uncovered, the count rate increased significantly. This makes sense due to the higher incidence of photons on the device when it is not blocked by an opaque covering.

Since the detectors were free-space coupled, they needed to be coupled with a single-mode fiber. This was accomplished adding a ThorLabs collimator, lenses, and a pigtail fiber stand to optical posts screwed into the detection head. To precisely align the fiber to the detector active area, the count rate was actively observed with an oscilloscope while adjustments were made to the alignment of the fiber. When the count rate was maximized, the fiber was aligned. When the temporal point spread function of a 1MHz laser pulse at 786nm was coupled to this device, there was evidence of reflection at 12ns. This indicates that the confines of the room, which are a few meters away, may be causing some reflection. There may also be

smaller reflections coming from the coupling stages. The sources of these reflections and the possible methods of reducing them should be explored in more detail. Possible means of reducing the impact of reflections include limiting extra light entering the system by carefully extinguishing all or most of the non-laser sources in the room and using darker coverings around the detectors, or applying anti-reflective coatings to the problematic surfaces.

The two purchased detectors had different active region areas: 50µm and 100µm. Because a smaller active area will have less noise for detecting a single speckle, we sent the 100µm detector back to the manufacturer for a new detector head. Since this was several months after the purchase, they also installed new firmware and software, and built a pigtail connection for the device. Upon receiving the updated device, the first three basic tests to operation had to be performed, but there remain many more steps for validation.

While setting up the initial tests, it became clear that the default operating bias voltage would not always be ideal, as the dark count rate was rather high. To build an understanding of our system, the dark count rate as a function of overbias voltage was measured. A constant temperature of 14.6°C was maintained along with free-running detector gating, 50ns holdoff time, and 50mV threshold for detecting the riding edge of the avalanche pulse. The room lights were not illuminated but only a cloth covering was used. The remaining light in the room was left unchanged throughout the test. These results are plotted in Figure 4-8.

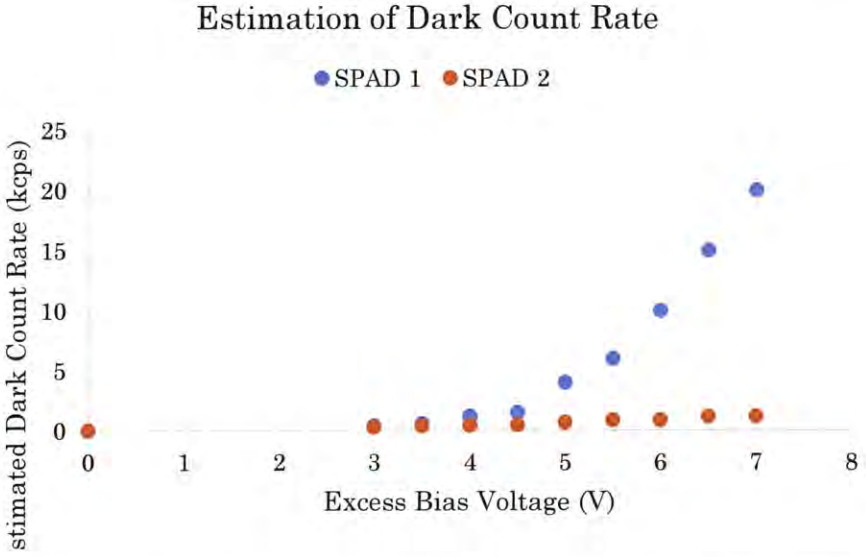

Figure 4-8: Dark count rate as a function of excess bias for MPD Si FG-SPAD. The blue dots correspond to the SPAD running on older software and with coupling completed in-house. The orange dots correspond to the SPAD running on newer software and with coupling completed by the manufacturer. There are clearly

some unexplained discrepancies between the two devices, though one explanation is differences in the casing of the two SPADs. The first SPAD has looser casing, which may be causing the significantly higher estimates of dark count rate.

This test was repeated with the second MPD Si FG-SPAD, which has updated software and was professionally fiber coupled. These results are also plotted in Figure 4-8. There is a large discrepancy between the two. This could be due to the casing limitations on the older SPAD, which presents more opportunity for light to enter the system and disrupt the measurement.

In order to determine the viability of existing designs for gated TD-DCS, our team ran a Spectre simulation of the current flow through a silicon chip design used for another project that has been built into a functioning camera, which indicated a 2.5μs holdoff time would be needed for the current to drop below the value needed for an AP probability less than 5%. Since this indicated existing designs would not meet the gated TD-DCS system requirements for repetition rate and holdoff times, the macropixel detector design approach was selected over the HECTIC approach [100].

To determine the viability of future designs and the tradeoff between linearly summed DCR and reduced APP with longer holdoff times in macropixel designs, the team performed simulations in Wolfram Mathematica to determine the number of pixels required in each macropixel to achieve the desired repetition rate without being consumed by dark count noise. The simulated model takes as inputs the number of signal photons detected per laser pulse (typical value 0.01 counts without microlenses), the dark count rate (typical value 1kHz), laser pulse repetition frequency (prf) (typical value 10MHz), detector gate width (typical value 2ns), holdoff time (typically 1μs), integration time (typical value 250,000 simulated laser pulses, which is 25ms for a 10MHz prf), and number of detectors in the macropixel (typical values 8, 16, or 32). In the typical case, detected photons are generated with a Poisson process of parameter 0.01, afterpulses are generated as a function of time (exponential decay) after the most recent detection, and dark counts are generated as a Poisson process of parameter 0.0001 (1kHz/10MHz). The binary macropixel model reports 1 if any pixel reports an event and the grayscale macropixel model reports the number of pixels reporting an event. These outputs are then used to calculate the simulated autocorrelation function. Furthermore, the blocking loss can be calculated for the binary macropixel model by the percent of time the macropixel reported zero when at least one pixel should have detected a signal photon, but could not due to the holdoff time. Blocking loss in a grayscale macropixel is the percent of time the macropixel failed to count a pixel that should have detected a photon, but could not due to the holdoff time.

The model is still under development, but it is expected to be informative to the design once a better estimate is made of the number of signal photons per pulse arriving at the detector during the gated window, both with and without effective optics like microlenses. The estimate of 0.01 counts per pulse was made using the integrated TPSF counts in a 2ns window 700ps after the detection peak (the peak of the TPSF) from an experimental measurement by the Martinos Center with the Picoquant Vis-IR STED and MPD Si FG-SPADs. The experimental counts were adjusted for a 1064nm wavelength by assuming 4 times more power, which is 5.5 times more photons due to decreased energy per photon, as allowed by ANSI limits, and a 20% detection efficiency for a typical 1064nm detector, which is 4 times the number of photons seen by the detector compared to the 5% detection efficiency of the MPD Si FG-SPAD at 765nm [69]. As they currently stand, these simulations indicate signal collection enhancement will be required to avoid unacceptable levels of shot noise [96].

A third set of simulations was run by a team member to consider a timed quench approach to decreasing the afterpulsing probability. As in the simulation with an existing design, a Spectre simulation is used to estimate current flow in the circuit. However, in this case the circuit is modelled as an indium phosphide (InP) device as current in Si devices increases too quickly, and is always quenched at a specified time after the detector arming is complete, and instead of detecting the avalanche with passive quenching, the avalanche is detected by comparing the signal from the detector pixel with the signal from a dummy detector pixel. Longer arm-quench sequences create a larger difference signal, but result in a higher total avalanche charge, where total avalanche charge is measured in femtocoulombs, fC. The results of these simulations indicate that the signal, though small, can be detected, and total avalanche charge can be reduced, if only slightly. Moving forward, more simulations should be run: (1) to interrogate the effect of process variation on the signal and the potential of a programmable capacitance trimmer to compensate for these effects; and (2) to determine the tradeoffs between reduced photon efficiency with the multi-nanosecond arm-quench sequence, as photons arriving just before or during quench will not be detected, and the reductions in APP with the reduced avalanche charge [101].

4.3.3 Future detector validation steps

Some tests were planned that were never executed due to staffing limitations and collaboration costs. One planned test involving the HECTIC SPAD approach would have measured the afterpulsing of the device as it was pushed to shorter and shorter effective holdoff times. When the test plan was put in motion, there were complications: the quench signal, which would permit a measurement of the holdoff time, needed to be wired out to an external pin. This required a technician's time

and conflicted with a sponsor visit and demonstration of the device so the test was postponed. After this the firmware would not build, due to a software error or required update, and debugging was difficult due to limited expertise with the Vivado toolchain. Confounding this problem were the lack of availability of interested persons to dedicate time to this exercise, and the lack of understanding between the original builders of the device and those who have been using it most recently. That is, the device has been changed sufficiently that it is not recognizable to the original parties. The test was not pursued, as there was some additional concern about even being able to get useful data on afterpulsing, since the HECTIC SPAD is limited to holdoff times of at least four clock cycles, which may not have been short enough to see significant impacts from afterpulsing. In the future and with more time, it would be helpful to characterize the afterpulsing in the chips designed by Lincoln in the past so that these considerations can be incorporated into afterpulsing-limited setups such as the gated TD-DCS test bed.

Another test that was planned, funded, and never executed was a breadboard implementation of sinusoidal gating for proof-of-concept before committing to a test chip design for fabrication. This test was outlined to be simple, but the time requirement was still too great for the researcher who proposed it, and it never was started. Moving forward, the team decided that sinusoidal gating was probably too different and complicated from what had already been done at MITLL to warrant the fabrication costs of a test chip. There is also the problem of decreased photon detection efficiency (PDE) as a result of sinusoidal gating, which has lower average bias for a given peak overbias than traditional square gating [102]. Nevertheless, sinusoidal gating does offer an interesting solution to fast quenching and reset that may be useful for tackling the afterpulsing problem in the future.

Some tests are still in the planning stages and are projected to help the team better understand the system and design requirements. Although these tests are expected to improve the understanding of the performance of existing designs, the main benefit for our team is to inform the design of the final detector chip. Interestingly, this double benefit structure also makes it easier to get access to the devices, as the teams currently working with them also gain from the information resulting from these tests. This rationale also applies to the HECTIC afterpulsing test described above.

One test that is in the later stages of planning is to obtain correlation measurements with the Lincoln Electro-Optical Sensor System (LEOSS) Low SWaP Sensor (LSS) and a 32x32 SPAD array using light at 1064nm. The goal of these tests is to understand how the tradeoff between holdoff time and repetition rate could be pushed to its limits. The test requires a fiber to split light from a continuous-wave laser onto two pixels in the detector. If one detector fires when the other does not, it is marked as noise and ignored. The test would be to see if there

could be any benefit from using the correlation to filter out afterpulsing and use a shorter holdoff time despite the increase in afterpulsing, which is a self-propagating process.

One very significant test that has yet to be performed is the validation of gated TD-DCS with a comparison of the depth sensitivity achievable using detector-gated TD-DCS and TD-DCS that removes early arriving photons from the data with post-processing. Another useful test would be comparison with the MGH setup results, which could be accomplished by probing an identically produced medium with each system and comparing the results. Other informative grounding steps include simulations of the number of photons arriving at each detector depending on the medium, which can be achieved with Monte Carlo simulations [103], and comparisons of the detectors at various wavelengths, to get a better understanding of how dependent the measurements are for properly matching the detector and the illumination source.

4.4 Time correlator

The time correlator is a device that keeps track of time for the measurement, performs simple calculations between different timed signals, and records these calculations as outputs. Typically this is accomplished with a field-programmable gate array (FPGA).

4.4.1 Criteria for time correlator design and procurement

The criteria for a time correlator are not as tied to the theory of DCS as the source and detector. Instead, it must simply be a reliable indicator of time. The most challenging aspect is that to appropriately throw out photons detected too soon after a laser pulse, it must be able to record the very short times between the laser pulse and the detected photons. Accordingly, the measures of merit are timing resolution, maximum acquisition rate, number of inputs, bin width, timing jitter, and dead time due to the conversion rate. For good timing, smaller resolution is better along with a faster acquisition rate, small bin width, small timing jitter, and low dead time due to the conversion rate. Having multiple inputs is useful for working with multiple detectors and experimenting with different timing setups, but only one input is required per detector for basic TD-DCS operation or SPAD gated operation and only two inputs are required for software-gated operation—one for the detector and one for the laser synchronous pulse.

The time correlator used by the Martinos Center was a custom device that we were discouraged from pursuing on account of the time cost of ordering the custom part and then programming it for our purposes. In my search for an appropriate

device I considered the PicoHarp HydraHarp 400 Event Timer and Time-Correlated Single-Photon Counting (TCSPC) Module and the ID Quantique ID900 Time Controller. Primarily due to cost concerns, I selected the ID900. The rest of the team agreed primarily due to stated performance. Unfortunately, the ID900 was very much in a state of development at the time of purchase, which was not helped by the fact that we rushed the order for it to arrive before the end of the fiscal year for budgeting purposes. To compensate for this, our team found access to two other time correlator devices at MITLL: the ID801 Time-to-Digital Converter (TDC), and the PicoHarp 300 TCSPC Module. The summary of these devices with respect to gated TD-DCS figures of merit is shown in Table 4.3. Note that values are approximations based on specification documentation from the manufacturers. Unknown values have been left blank. Other criteria not shown include cost, histogram features, data transfer rate, and internal electrical pulse rise times.

Table 4.3 Comparison of Various Time Correlator Options

Parameter	Goal	Custom FPGA	ID801	ID900*	PicoHarp 300	HydraHarp 400
Timing resolution (ps)	<100		81	20;100	<12	1
Time tag rate (MHz)	>100		10	25;100	5	40
Inputs	2		8	4	2	4
Binwidth (ps)	<100		81	13;100	4	1
Timing jitter (ps)	<100			8;100		<12
Conversion rate (ps)	<100			<6ns	<95ns	<80ns
Maturity	High	Low	High	Low	High	High

*Semi-colons distinguish high-resolution versus high-speed modes

4.4.2 Time correlator validation results

In order to set up validation tests for the time correlators, they first needed to be made operational. This involved locating and installing the driver software, which was nontrivial in several cases. Additionally, the ID900 in particular requires a dedicated ethernet card, which needed to be acquired and installed. Furthermore, due to MITLL security measures, a firewall exception protocol needed to be developed in order to interface with the device from a laboratory computer, which must be then disconnected from the internet whenever the protocol is in place.

After the setup was confirmed and the device was able to interface with the computer, the count mode was validated by supplying a signal of known frequency to an input channel and reading the count frequency. If the time controller's measured frequency matched the repetition rate of the input signal, which for our tests was typically a clock generator or laser synchronous pulse, then the time controller was considered to be operating according to expectation. We also recorded timestamps using the ID900 graphic user interface (GUI) and plotted the distribution of first-difference terms (i.e., the time between recorded inputs). The tests up to this point were mostly just to ensure that the majority of first-difference terms were the frequency of interest; however, an informative future test would be to build distributions at various frequencies to characterize the limitations of the timing scheme for a given input signal at various frequencies. The input signal should have as low a jitter as possible to ensure that the characterization is primarily of the time correlator and not the input signal generator.

Note that there were several problems with the early firmware and software for the time controller. The timestamps were occasionally recorded only as empty named files and several of the Standard Commands for Programmable Instruments (SCPI) did not perform as specified in the ID900 User Manual. These problems were identified and remedied by working with the distributor and updating to the most recent firmware and software updates for the device.

As the time controller is the means of actually taking the DCS measurement, another test aimed to calculate an autocorrelation with our full test bed, to determine how the autocorrelations from our system compared with those from the Martinos Center's test bed. First, I used no phantom, just an indirect illumination of the detector, the Eagleyard EYP-DFB-1064-1500-BFY2-0010 with the PicoLAS BFS-VRM-03HP laser driver operated at 200kHz with 10ns pulses as the source, and a MPD Fast-Gated Silicon SPAD in free-running mode (not gated) as the detector. Next, I used a 2%-fat cow's milk phantom in a paper cup as the diffuse medium, the PicoQuant OEM CPDL-S-F 1064nm laser without amplification as the source, and a MPD Fast-Gated Silicon SPAD in free-running mode as the detector, which had an average rate of 100kcps detections during this test. The detector was connected to one input and the laser synchronous pulse was connected to another. Autocorrelations were performed using all detected photons within each measurement. No software gating was used. The resulting autocorrelations are reproduced in Figure 4-9. Some aspects of the Eagleyard figures were as expected: (1) the autocorrelation at high lag (~1s) is 1; (2) the autocorrelation starts at 10e-5, which makes sense for a 200kHz laser; (3) the trend of both the 100ms and 3s integration times is the same, and the 3s integration time has less noise.

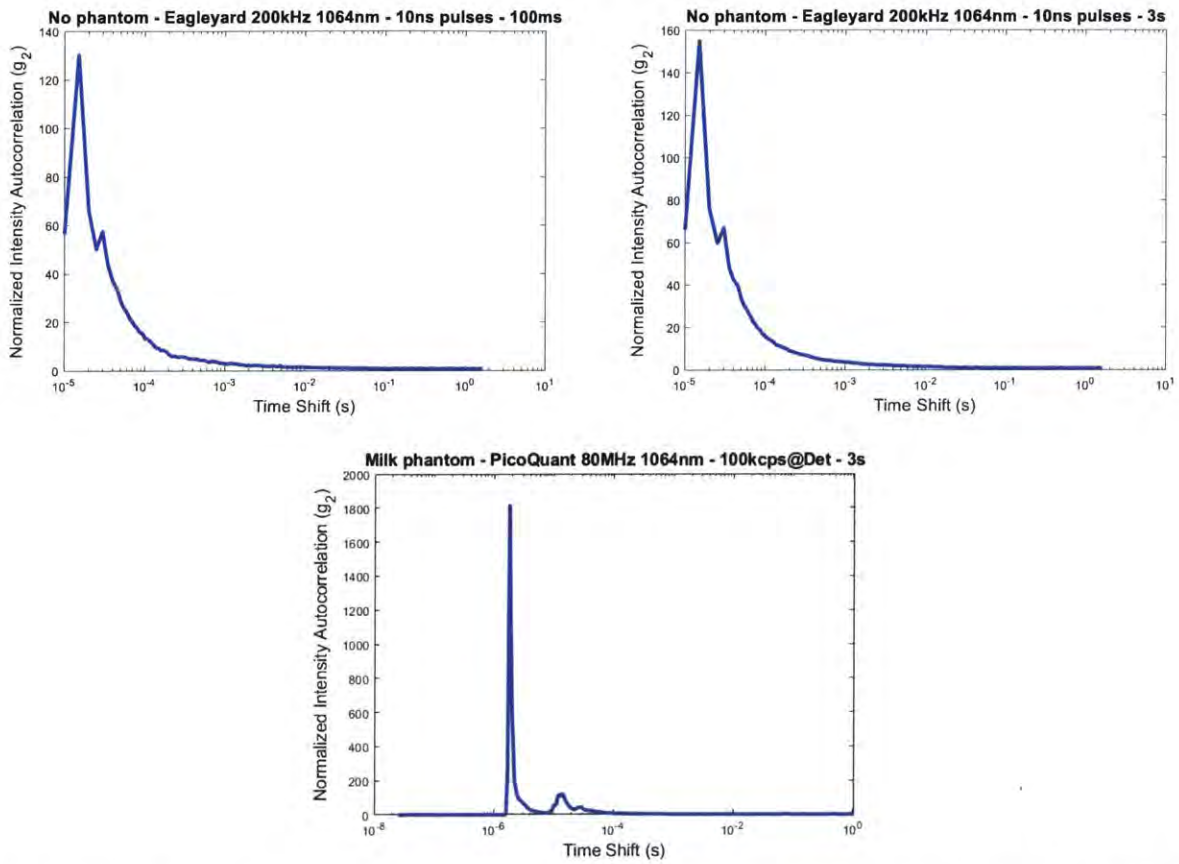

Figure 4-9: Initial autocorrelation measurements. The autocorrelations in the top row were acquired using no phantom, the Eagleyard EYP-DFB-1064-1500-BFY2-0010 with the PicoLAS BFS-VRM-03HP laser driver operated at 200kHz with 10ns pulses as the source, and a MPD Fast-Gated Silicon SPAD in free-running mode (not gated) as the detector. The top left autocorrelation had a 100ms integration time, while the top right autocorrelation had a 3s integration time. The autocorrelation on the bottom was acquired with a 2%-fat cow's milk phantom in a paper cup as the diffuse medium, the PicoQuant OEM CPDL-S-F 1064nm laser without amplification as the source, and a MPD Fast-Gated Silicon SPAD in free-running mode as the detector.

When we sent the resulting figures to the Martinos Center, they indicated that the decay of the autocorrelation looked different from what they would expect given our setup, as the autocorrelation peak was greater than 100 and is oddly shaped. One possible problem was that there was no awareness of the importance of keeping the average count rate at the detector below 5% of the laser frequency to avoid saturating the detector at early photon arrival times, which could be contributing to the odd shape in the autocorrelation function [104]. In the Picoquant autocorrelation, we noticed that the time between detections was less than 25ns

37.5% of the time, which suggests a pairing between photons that is not expected to be present [104]. This also may have resulted from detector saturation. In an attempt to isolate the problem, we brought the ID900 to the Martinos Center and used it with their setup, which included the PicoQuant Vis-IR STED laser, an MPD Fast-Gated Silicon SPAD in free-running mode, and a probe approved for human use. One of the researchers agreed to be the diffusive medium for the comparison. The detector output was passed to both the custom field-programmable gate array (FPGA) used by the Martinos Center and the ID900. The results, shown in Figure 4-10, were comparable and we were unable to identify any problems. Note that the custom FPGA records conversion start and stop times along with the time stamp data whereas the ID900 only records detection times.

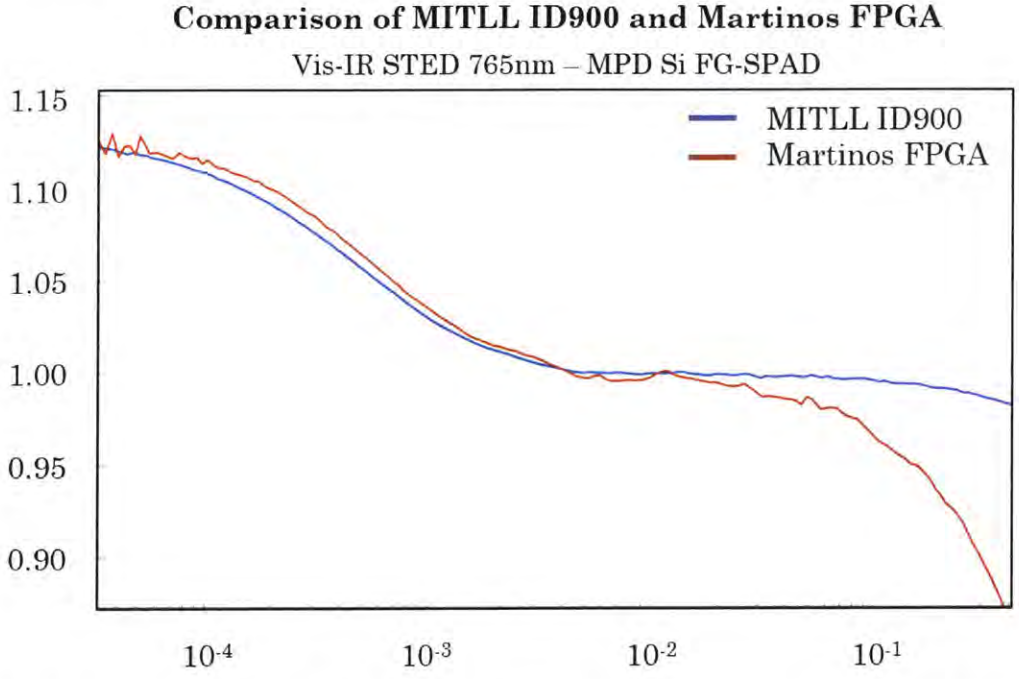

Figure 4-10: Comparison of MITLL ID900 and Martinos FPGA. A PicoQuant 765nm Vis-IR STED laser, an MPD Fast-Gated Silicon SPAD in free-running mode, and a probe approved for human use with one of the researchers as the diffuse medium. Note that the curves have similar shape for computing BFi, but different end behavior, possibly due to the time correlators' data collection start and stop behavior.

Eventually, after a year of pushing a foreign nationals visit request to MITLL, the Martinos Center researchers were able to come visit to help debug the setup. During debugging, we used the PicoQuant OEM CPDL-S-F 1064nm laser with amplification to 50mW, a MPD Fast-Gated Silicon SPAD in free-running mode as the detector, and the Martinos Center probe on a researcher as the diffusive

medium. The histogram temporal point spread functions (TPSFs) produced by the ID900 GUI and the decay of the autocorrelation function were reasonable, but the distribution of the detector timestamps modulo the laser period plotted as a uniform distribution. Additionally, the time stamp file saved for the laser was much smaller than it should have been, considering the length of the test and the detector timestamps. It is possible we are exceeding the capabilities of the timestamp functionality on the ID900, which is likely less than the specified 100MHz maximum event detection. This led us to reevaluate the setup and use the computational blocks in the ID900 to calculate both relative (laser to detection) and absolute (start of measurement to detection) timestamps simultaneously. This records only at detections, and is therefore a less computationally demanding measurement for the ID900. The execution of this measurement restructuring is still in progress as of the writing of this thesis, but the initial SCPI commands provided by IDQuantique are provided in Appendix C.

4.4.3 Future time correlator validation steps

Independently every piece of equipment used in our test bed setup has been tested operationally with the Martinos Center setup. However, there seem to be some lingering doubts about the time correlator in particular. To quantify the validity of these doubts, tests should be made to estimate the maximum operating rate of our ID900 under different conditions, including (1) timestamps from a single channel using the internal start signal, (2) timestamps from a single channel using an external start signal, and (3) timestamps from a single channel using an external start signal and one computational block for absolute timestamps. With gated detectors, the time correlator is in operating mode 1, but for software gating, the time correlator must operate in mode 3. The maximum operating rate can be quantified using histograms of the values of the relative timestamps and the values of the absolute timestamps modulo the input frequency. The input should have low jitter and the maximum operating rate will be considered the point where the histogram broadens beyond a certain threshold value, perhaps using a statistic like kurtosis. In such a test, kurtosis would be expected to decrease as the time correlator is pushed beyond its limits. It is also possible that the correlator will simply peak at its maximum detection frequency, and this would also mark a termination criterion for finding the maximum operating point.

Another important step in validating the time correlator will be working with the Martinos Center in continuing to define "reasonableness" for an autocorrelation of detection counts. Ideally, a representative curve for a given setup could be modeled and calculated for comparison with experimental results.

4.5 Meta-components

It may seem trivial to consider all the connecting pieces, but especially starting from an empty lab, such parts enabled the test bed setup and became limiting factors when they were absent. These additional parts can be grouped into four categories: (1) measurement equipment, (2) connection equipment, (3) diffuse media materials, and (4) practical components. Measurement equipment includes the optical power meter with its associated detection head, the oscilloscope, and simple detectors for the input, the function generator, the clock generator, the delay generator, and the spectrum analyzer. The connection equipment includes fiber splitters at 50-50 and 99-1, optical fibers and couplers, fiber cleaners, a fiber scope, SubMiniature version A (SMA) cables and couplers, Bayonet Neill-Concelman (BNC) cables and couplers, SMA-BNC couplers, power cables, ethernet cables, and Universal Serial Bus (USB) cables. The diffuse media materials include optical diffuser prisms, beakers, needles, syringes, probe structural materials, cow's milk, ink, Intralipid®, silicon oil, isopropyl alcohol, and a refrigerator. Practical components include time, experts, and funding.

4.5.1 Criteria for design and procurement

Measurement equipment should measure what it says it can measure, so that the equipment we select will meet our requirements. Connection equipment should not cause undue disruption to the signals or add noise; the diffuse media materials should return reliable measurements; the practical components should make everything possible. Even though limited resources do not permit a full investigation of every piece of equipment, care was taken (sometimes *ex post facto*) that at least the data sheet suggests this equipment should not be the limitation to the test. A few examples of this thought process are included below.

The detection heads for the power meter and oscilloscope needed to be able to accept high enough power and bandwidth for their application. In tests like the amplification characterization, special care needed to be made as power changed over time. Wavelength and coupling were also important considerations for the detector. We borrowed a ThorLabs DET025AL Si free-space coupled detector for the 786nm wavelength and a ThorLabs DET08CFC InGaAs fiber-coupled detector for the 1064nm wavelengths from another group at MITLL. Since coupling to the detector made the measurement much more reliable than a free-space detection, we also purchased a ThorLabs DET025 Si fiber-coupled detector for the 786nm wavelength. These ThorLabs detectors were used with the oscilloscopes and all required A23 batteries. We selected the ThorLabs PM100D power meter, and the initial detector for use with the power meter was a S151C Si detector limited to 20mW. For the more powerful tests, this detector was replaced by an S140C Si

detector limited to 500mW or an S305C thermal power sensor head, which was limited to 5W.

For connection components, the most impactful consideration is the use of single-mode fiber from the diffusive medium to the detector, but it also is useful to have a single-mode fiber from the source to the medium in order to limit noise in the system. Single-mode fibers have greater losses, but since they only allow a single-mode to pass, they are a requirement for detecting speckle patterns in the DCS measurement we are designing for.

The diffusive medium is expected to either be a phantom (i.e. model) or living tissue. A basic phantom can be created simply using cow's milk, but the limited standardization of the fat content and other components does not allow for rigorous and reproducible studies. Cow's milk phantoms are instead ideal for testing initial system operation and as a stand-in for future experiments. Combinations of cow's milk and water can also provide insight on the responsiveness of the system to changes in diffusivity. Beakers containing the phantom must be at least an inch or two in radius to simulate a semi-infinite medium. Note that, while an arbitrarily large phantom might better approximate this assumption, it not only might fail to model a human head, but it would also be a waste of materials, since the probability of photons traveling farther in the diffusive medium becomes vanishingly small. The same container concerns for a cow's milk phantom apply to an Intralipid® phantom.

A more complicated phantom requires Intralipid®, which is a pharmaceutical fat emulsion used to intravenously provide calories to patients who cannot eat. Intralipid® is therefore much more standardized and is often used as a phantom in diffuse spectroscopy literature [19,31,105]. Both Intralipid® and cow's milk must be stored in a refrigerated environment and used within a period of time after opening. One solution to increase the shelf-life of the Intralipid® is to use needles with syringes to extract the Intralipid® from its case and then use a 70% solution of isopropyl alcohol to sanitize the extraction point. Ink can be added to either type of phantom to increase absorption in the medium according to the test requirements.

The Intralipid® phantom can be made a more useful estimate of the human brain by adding another layer to imitate the scalp, or flow to imitate blood perfusion in the brain. The second layer is made using silicon oil, as it separates from Intralipid® and has different optical properties, more similar to scalp tissue [31]. In Monte Carlo simulations, three to five layer models are commonly used to represent the brain as a series of planes with optical properties mimicking the scalp, skull, and brain tissue, where brain tissue can be further decomposed into cerebrospinal fluid (CSF), grey matter, and white matter [45,47,106]. The optical properties used as inputs to the simulations depend not only on the tissue type, but also on the

wavelength of incident illumination. Multi-layered models add complexity and are therefore more challenging to construct in a phantom, and yet there is at least one example of a four-layer epoxy resin phantom, built with titanium oxide scatterers and ink absorbers, that has been used to test the ability of TD-fNIRS to determine the absorption coefficient in each layer [47]. Adding flow is also more complicated, but developing a reliable technique, perhaps with a magnetic stirrer in a single-layer phantom, could be used to quantify the sensitivity of TD-DCS to changes in flow.

Tests on living tissue have been done, but are not standard practice at MITLL, while the Martinos Center, as a partner of MGH, has extensive experience with both rat and human studies for optical neuroimaging. In humans such tests require a diffuse prism at the fiber termination point to meet American National Standards Institute (ANSI) requirements for skin exposure. Such prisms are used in the Martinos Center's approved tactile human probe. For tests on humans away from the brain region, the probe must be directed on diffusive areas of the body, such as areas with high adipose tissue content. Areas that are skin alone, such as the tissue between the thumb and the hand, have negligible diffusive properties and a reasonable signal will not be attainable. Human studies are especially challenging because they require special approvals.

The probes holding the fibers must be able to maintain a constant source-detector separation, as this distance has strong effects on the DCS measurement [29,31]. Our phantom probe stand was therefore developed with computer modeling and manufactured with a laser cutter using thin acrylic board. The probe can sustain a few discrete heights relative to the table top, and a continuous range of a few centimeters source-detector distance. The laser cutting file is illustrated in Figure 4-11.

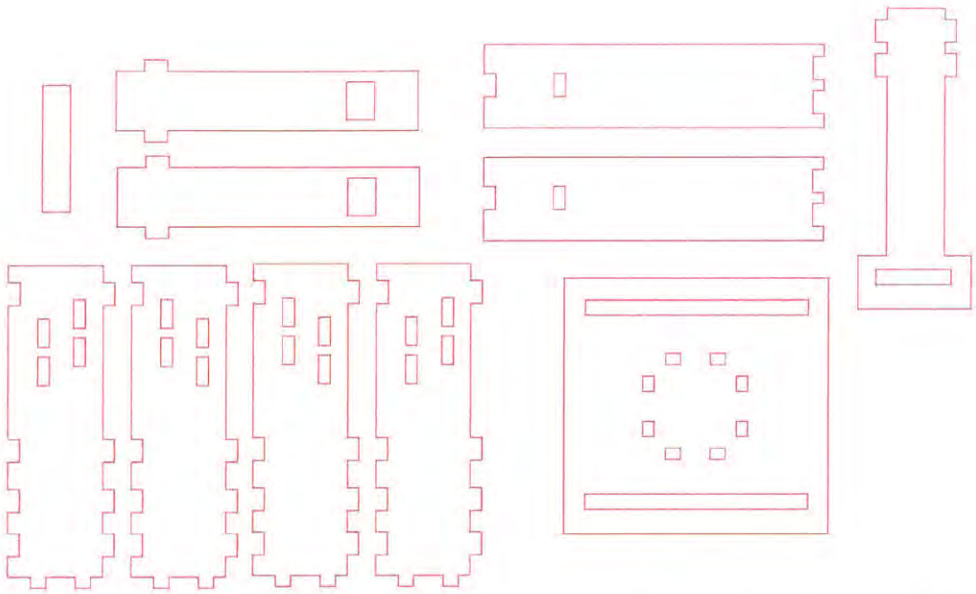

Figure 4-11: Probe stand diagram. Snapshot of Drawing eXchange Format (.dxf) file of the acrylic probe stand constructed for MITLL. Red lines indicate cuts. Note that the design must be altered for different construction material thicknesses.

For practical concerns, there must be funding that will not expire before all acquisitions are made for the test bed. There must also be enough time to complete the building and operation of the test bed, and experts with the proper expertise to make that possible. Practical concerns are extremely difficult to quantify, because compromising on one will often inflate the others in an optimization problem that is challenging to solve.

4.5.2 Validation results

Part of learning is, of course, learning from mistakes and failures even more than from success. In a mistake, I used the 20mW limited S151C detector on power measurements with the Eagleyard and amplified PicoLAS lasers up to what looked like over 300mW. When presenting my results, I was kindly asked what detector I was using. Although it can be dangerous to put too much faith into predictions about what will happen in a test, the estimations can also be a good way for identifying errors. The tests were rerun with the S305C 5W detector for the results in Figures 4-7 and 4-8. One caution with this detector is that it was far less responsive than the lower powered detector and patience was required to wait for the output to stabilize at a certain power value. Lower power tests were taken to assess the potential damage to the S151C detector, and it seemed unaffected, though blasting it with high power is still not recommended.

In a similar scenario, while evaluating pulse shapes with the LeCroy High Resolution Oscilloscope (HRO) 64Zi 400MHz 2GS/s, the pulses were appearing too smooth and symmetrical against the expected output. To test whether these were indeed the pulse shapes or if the output was limited by the sample rate of the oscilloscope, we repeated the measurements with both a Rhode & Schwarz RT01044 4GHz, 20GS/s oscilloscope and a Picoscope at 20GHz, 400GS/s loaned from another group at MITLL. The pulse shapes were indeed less Gaussian than the bandlimited oscilloscope indicated, which led the team to purchase our own Picoscope for future measurements.

Another notable test involved the connection equipment. In the process of debugging the time correlator, the question arose about whether cable impedance was causing problems with the setup. There is no multimeter in the laboratory, so we had to be creative about testing impedances when not specified in the data sheet. This required checking cable lengths, ensuring coaxial cables still had their pins and were not overly bent, and recording timestamps to compare for different cable arrangements. No problems were found, but such considerations are important to keep in mind moving forward, especially as synchronization between the gate and the laser becomes a concern.

4.5.3 Future validation steps

The most useful tests of the meta-components involve the operation of the test bed as a whole. These include validation of test bed operation at 786nm and 1064nm, quantifying the effect of source-detector separation for our detectors, evaluating depth sensitivity with a two-layer phantom, and evaluating flow sensitivity with a flow phantom.

The initial baseline validation tests at both wavelengths should use a consistent setup and a homogeneous phantom. The tests should be able to consistently measure the Brownian coefficient of the phantom. A follow-on test would evaluate whether the setup properly finds that this coefficient decreases with increased dilution of the diffusive media. Flow measurements would also use a homogeneous phantom, and would require a specific setup where the only parameter modified is the flow speed, perhaps using a magnetic stirrer or fluid mechanically pumped through a tube at some depth in the phantom. This measurement could be repeated at different wavelengths or gating strategies.

Since source-detector separation affects the depth sensitivity of DCS measurements, tests that modify this parameter should use a two-layer phantom of Intralipid® and silicon oil. The depth sensitivity can be quantified as in the supplemental material of Sutin et al. [31], by decreasing the thickness of the top layer (silicon oil) and noting how the decay of the autocorrelation curve changes to

match that of the bottom layer alone. Alternatively, our probe stand was designed to be incrementally submerged in the phantom. This avoids possible mixing effects in the phantom but is a messier setup, with more cleaning required to maintain good condition of the components. The source-detector separation could be modified at some large granularity for preliminary measurements, since this is not the focus of the MITLL TD-DCS test bed. With gated detector operation depth sensitivity tests, source-detector separation must remain constant. The depth sensitivity could be quantified as in the source-detector separation test. It would be useful to create a matrix of observations for different gate start times and gate widths with various source-detector separations.

A few other possible tests include spatial sensitivity tests and crosstalk tests. Spatial sensitivity measurements could be performed by placing an object at a certain depth in a homogenous medium and measuring the spatial profile of the object and determining its width. This could be repeated with objects of various shapes and sizes. Crosstalk could be measured by placing two identical objects at a certain distance from each other at a certain depth in the homogeneous phantom. This would then be repeated at various distances to determine when the signal interference from the second object becomes debilitating in properly detecting the target. Both when the objects can no longer be resolved as well as a quantification of the noise from the other object at various distances would be of interest. This could be repeated with objects of different sizes, objects with different optical properties, and objects at different depths. Since the combinations of these spatial measurements are vast, there is possibly better potential for Monte Carlo modelling of these scenarios to characterize the system using a complex-media photon migration solver like Monte Carlo eXtreme (MCX) or Mesh-based Monte Carlo (MMC) for complex media [103].

Chapter 5

Adjusting measurements and applications for policy-awareness

Development of the gated TD-DCS test bed revolves around several problems, from studying cerebral blood flow to identifying the power of a laser, that can be used to structure a policy-awareness evaluation. This makes it a useful set of example cases for understanding how to adjust both the test bed measurements and their applications to ensure that the test bed is policy-aware for effective interaction of policy and science. In Section 3.1.4, a few of the user applications of gated TD-DCS under consideration are listed. Among these applications, all three user interpretation classifications can be found. Using examples and intuition from the test bed development in Chapter 4, this chapter will consider how to change the measurements made, or the way they are made, and the user application to produce a more satisfying level of policy-awareness. Furthermore, the benefits of adjustment are shown to be two-fold within the definition of policy-awareness developed in Chapter 1: both science communication and scientific rigor can be improved using the framework developed in Chapter 2.

To identify adjustments that scientists and policy-makers can commit to that will produce sustainable results, it is imperative to consider the root-cause question: why do user interpretation and policy context not always align? There are certainly human-centric causes, which include organizational, monetary, time, social, educational, and communication costs as well as the way in which human values define application space (i.e., how do people determine what is "good enough"). There are also experiment-centric causes, which result from the nature of test beds being inherently investigative, that is, the projected output is often not the actual output, since a test bed is a way to learn about a system. Keeping these possible reasons for misalignment in mind can help develop solutions that will not only address the misalignment but also address the cause, and therefore have a better chance at finding a convergent solution.

5.1 Adjusting user applications

One way to improve the policy-awareness of a technology is to adjust the way it is used. All three categories of initial user interpretation will be considered and coupled with examples from the gated TD-DCS test bed development. Although only gated TD-DCS test bed applications are explored here, similar analysis can also be applied to other research test beds and systems. These adjustments include considering other possible user interpretations, planning for adjustments based on

incoming measurements, and considering the lingering questions after test bed results are considered.

The first misalignment can occur when a test bed is considered purely as an approach to a problem. As discussed in Chapter 2, this could lead to difficulty in securing funding and has no real policy-awareness as no actions are implied from the results of the test bed, despite the fact that there very well may be policy-relevant results. In the case of gated TD-DCS, the corresponding user application is the use of the technology developed with the test bed to improve understanding in the medical field. While this is certainly still a valuable task, in itself it has no policy-awareness. What is learned here is neutral to whether it creates or solves problems in policy construction. To adjust to a policy-aware interpretation, the user can make the effort to consider the implications of the new understandings from the test bed results. This is a prerequisite for the user to identify policy-relevant concerns from the test bed results. For example, validation testing with the time-correlator in the gated TD-DCS test bed forced the team to reconsider how measurement happens in the system, and by considering the implications of this we were able to develop a less computationally costly measurement strategy for gated TD-DCS. By recording the absolute timestamps in terms of a computational block with the laser as the start instead of using the laser and detector as inputs, not only did we better learn how to use the time correlator, but we also learned that the computational complexity of the measurement could be decreased, enabling the faster measurements that are required for more diverse medical applications.

One useful heuristic for identifying policy-relevant applications is to consider a 2x2 matrix where columns are "ends" and rows are "means" and each column/row is broken down into one column/row for science and one column/row for engineering and technology [107]. In this model, science refers to a pure approach towards a problem, and engineering and technology refers to developing tools and solutions. The gated TD-DCS modality most suitably fits into the engineering and technology means for science ends element. Since this model neglects the policy element, I supplement this model with one more column/row for policy, as shown in Figure 4-1, where policy refers to actions or directives. Examples characteristic of each element are provided in the figure. For instance, lightning and NCAA (National Collegiate Athletic Association) is in the science means for policy ends element, because the understanding of lightning developed by science has led to regulations by the NCAA about how outdoor sports events are conducted in the detected presence of lighting within a certain radius of the sports field. By considering how the test bed results could be placed into each box in the matrix, the user is forced to consider alternatives to placement in the bottom left corner of the matrix, which is very rarely the only habitat for a test bed result.

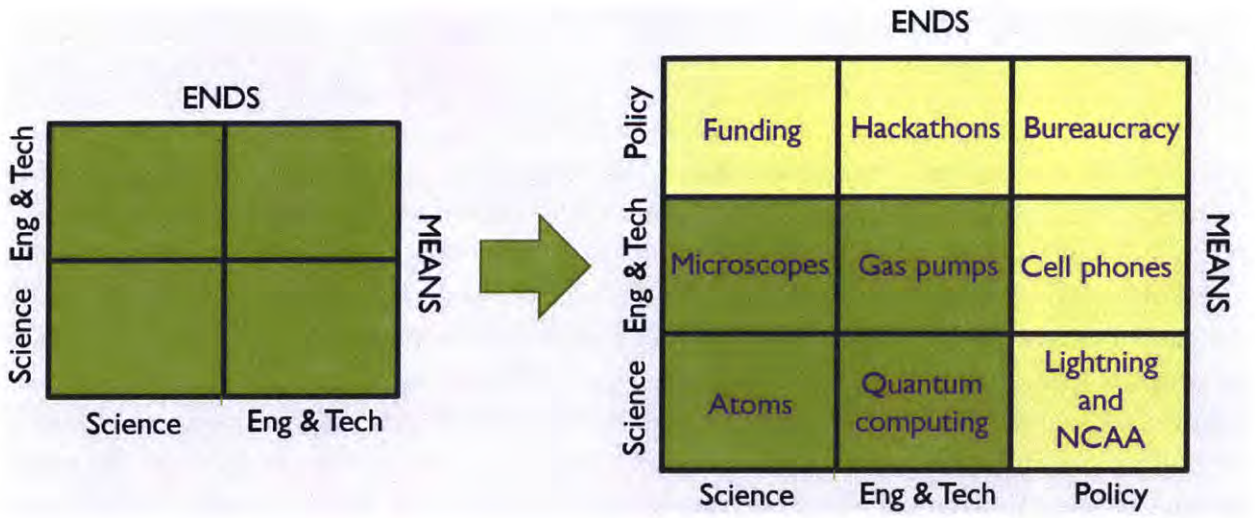

Figure 5-1: Science, technology and policy means and ends matrix. The matrix on the left is the original model and the matrix on the right is the model developed in this thesis, which adds a row and column for policy means and ends. Within each box is a representative example of what could be categorized into that box according to standard user interpretation or application. These examples are explained in Appendix B.

The second type of measurement to user interpretation misalignment occurs when a user interprets the evidence from a result improperly. This could be overemphasizing the relevance of a group study to an individual, or the relevance of a case study to a group, or some other breakdown of causal inference. One gated TD-DCS user applications relevant here is its use as a diagnostic tool for medical conditions. An adjustment that can be made in this case is the use of planned adaptation, which incorporates changing knowledge into policy with predetermined parameters established in advance of but conditional on measurements [108]. The dark count rate validation tests for the MPD FG-SPADs indicated that individual differences between detectors needs to be taken into more careful consideration than previously expected. That there are other parameters that may be influencing detector performance beyond the detector model, such as coupling efficiency and software, indicates that these additional considerations must be incorporated into how MPD FG-SPAD detections are interpreted for test bed results and their user applications. Without including or incorporating these parameters in some way, the evidence from the test bed will be less appropriately weighted in an evidence-based user interpretation. Using planned adaptation in this case would set a policy that is contingent on the detectors meeting certain parameters, which would need to be measured before the policy went into effect.

Realignment from the third type of user interpretation, which considers a test bed result as an answer to the problem at hand, can be addressed from the user side by identifying the related questions that are not answered by the test bed result and then considering if those questions have the potential to disrupt the connection of the test bed with the problem. In the case of gated TD-DCS, the test bed can be interpreted as an answer to studying blood flow in the brain. From this perspective, the test bed is defining a metric of blood flow, but it is possible that this definition is problematic if the questions left unanswered, such as the cause of changes in blood flow or measurement of the direction of blood flow, are integral to the aspect of blood flow that we want to study. From developing the test bed we identified a laser as part of the solution to finding an excitation source for gated TD-DCS (in addition to coupling components, diffusion prisms, amplifiers, and fibers), but as indicated in the verification steps a laser alone does not answer the question of single-mode detection, or adequate coherence length, or required power without damaging the subject tissue. These additional questions can be incorporated into source design, but must not be ignored if a gated TD-DCS measurement is to be made.

5.2 Adjusting test bed measurements

Unfortunately users cannot always be expected to make the right decisions or be aware enough to change their interpretations. It is important therefore to also adapt measurements while maintaining fidelity to the scientific process. Scientists face their own struggles with decision making and policy-awareness among the concerns of grant proposals, professorships, and scientific responsibility. These tasks have a high time cost to do well, and policy-awareness is typically not in the job description of an academic. Thinking back to the dual benefit of scientific rigor and science communication from increasing policy-awareness, it is clear that there is still some benefit for the test bed developer to ensure a policy-aware design. Standard operating procedures can help to automate this process in test bed design by addressing the various user interpretation categories when recording and reporting test bed results. The adjustments recommended here for test bed alignment to user interpretation include project selection, clarity of non-results, and clarity of assumptions. Although the examples discussed here are specific to gated TD-DCS, as with user interpretation adjustments, the lessons learned here can be applied to other technologies using similar analysis.

Test bed measurements can be adjusted for misaligned user interpretations of the results as a question, or approach, to a problem. In particular, test bed projects can be selected such that they have clearer implications. This is analogous to choosing a box in Figure 4-1 where there is a clear application for the test bed and taking measurements that are tailored to that application. While working on

the gated TD-DCS test bed, we encountered the problem of finding appropriate lasers at the wavelengths of interest, which traditionally were approximately 760nm and 830nm in a mixed modality system with fNIRS. This questioning interpretation of laser design, where the team was initially only focused on understanding what wavelengths could be used to produce gated TD-DCS results, led to the consideration of 1064nm, which also has several engineering benefits, including higher power limits and greater maturity of technology. By navigating the different mindsets represented in Figure 4-1, the test bed was not only able to address technical concerns with technology maturity, but it also presents the possibility of improving the signal-to-noise ratio, and therefore policy-relevant information content, by increasing allowable power.

A test bed can be adjusted for better alignment with an evidence-based user interpretation by ensuring record of non-results and failures as well as successes. Without recording these events in the test bed history, the risk of the user to poorly weight the evidence of the test bed results is much higher, since there is a selection bias to the results that are reported. One example from the gated TD-DCS test bed development is the use of oscilloscopes with different bandwidths. The lower bandwidth scopes were not recording some of the important information about the signal, and since this limitation was noted, it led to the follow-up measurements with higher bandwidth scopes, which improved both science communication and scientific rigor.

Finally, the test bed can be adjusted to align with user interpretations of test bed results as an answer to the problem by clearly listing assumptions. This makes it easier for the user to identify what was not tested and take the adjustment steps listed in Section 4.1. Furthermore, if these user interpretations persist, the measurements can be adjusted to more appropriately address the question the user assumes the test bed is already answering by improving equipment or relaxing certain assumptions with a different setup. This is very similar to project selection as described above. An example of this from the gated TD-DCS test bed is the mistake I made with the power meter while measuring continuous-wave laser responses. Had I not listed the detector I used, it would have been much more difficult to identify the error. This is another example of how policy-awareness is beneficial not only to policy, but also to science.

Chapter 6

Conclusions and future work

Test beds are an important feature of the policy-awareness of science. As a result, development of policy-aware test beds is an excellent focal point for developing science and technology informed policy. Considering the model developed in Chapter 2, to make a policy-aware research test bed the user interpretation and the test bed measurement must first be identified. Next, the alignment between the two must be evaluated, using risks and failures of misalignment as indicators. Validation procedures, such as those outlined in Chapter 4 and defended with theory from Chapter 3, are imperative for appropriately evaluating the measurement performed by the test bed. Based on the user interpretation and its misalignment with the test bed measurement, adjustments can be made as outlined in Chapter 5 that facilitate the user application's adaptation to the test bed measurement through consideration of alternative views, planning, and identification of lingering questions. Adjustments can also be made to the test bed itself, including careful project selection, and reporting of non-results and assumptions.

There are several interesting questions to pursue in the future beyond the scope of this thesis. For test bed development itself, beyond the tests described in Chapter 4, tests measuring blood flow in vivo on an adult head would give the ultimate validation of the gated TD-DCS system, and could be meaningfully preceded by forearm measurements. Additionally, case studies of other test beds would be useful in understanding how policy-awareness changes with fields of various levels of novelty and application. Future questions to explore in test bed policy include: Do we need a culture shift for policy-aware testbeds to be widespread? How much of this extra effort is the role of scientists versus technology policy experts? What can we learn about policy-aware testbed development from other fields? What does implementation of these adaptations look like?

Appendix A

Abbreviations and nomenclature

A.1 Abbreviations

ABET The Accreditation Board for Engineering and Technology
ANSI American National Standards Institute
AP After-pulsing
APD Avalanche Photodetector
APP Afterpulsing probability
ASE Amplified spontaneous emission
ASL Arterial spin labelling
BCI Brain-computer interface
BFi Blood flow index
BNC Bayonet Neill-Concelman
BOLD Blood oxygen level-dependent
B.S. Bachelor of Science
CBF Cerebral blood flow
CBFi Cerebral blood flow index
CBV Cerebral blood volume
CG Clock generator
$CMRO_2$ Cerebral Metabolic Rate of Oxygen
CO_2 Carbon dioxide
COTS Commercial off the shelf
CSF Cerebrospinal fluid
CT Computerized tomography
CTE Correlation transfer equation
CW Continuous wave
DCR Dark Count Rate
DCS Diffuse Correlation Spectroscopy
DFB Distributed feedback laser
DG Delay generator
DWS Diffusing wave spectroscopy
EEG Electroencephalogram
FAA Federal Aviation Administration
FD Frequency domain
FFT Fast Fourier Transform
FG-SPAD Fast-gated single-photon avalanche detector
fMRI Functional magnetic resonance imaging
fNIRS Functional Near-Infrared Spectroscopy

FPGA Field-programmable gate array
FWHM Full-width half-maximum
fUS Functional ultrasound
G2i Group to individual
GmAPD Geiger-mode APD, same as SPAD
GUI Graphical User Interface
HECTIC Highly Efficient Counting and Timing Integrated Circuit
HRO High Resolution Oscilloscope
HST Health Sciences and Technology program
i2G Individual to group
InGaAs Indium gallium arsenide
InP Indium phosphide
IR Infra-red
IRF Instrument response function
LEOSS Lincoln Electro-Optical Sensor System
LSCI Laser speckle contrast imaging
LSI Laser speckle imaging
LSS Low size, weight and power sensor
MCX Monte Carlo eXtreme
MEG Magnetoencephalogram
MGH Massachusetts General Hospital
MIT Massachusetts Institute of Technology
MITLL Massachusetts Institute of Technology Lincoln Laboratory
MMC Mesh-based Monte Carlo
MPD Micro Photon Devices
MRI Magnetic resonance imaging
MRI-TRUST Magnetic resonance imaging-T2-relaxation-under-spin-tagging
NCAA National Collegiate Athletic Association
NIST National Institute of Standards and Technology
NSTB National Transportation Safety Board
OCT Optical coherency tomography
OEM Original equipment manufacturer
PDE Photon Detection Efficiency
PET Positron emission tomography
PMT Photon Multiplier Tube
PROM Phase-based regional oxygen metabolism
RBCs Red blood cells
RTE Radiative transfer equation
SANS Spaceflight-associated neuro-ocular syndrome
SCPI Standard Commands for Programmable Instruments
SFDI Spatial frequency domain imaging

Si Silicon
SMA SubMiniature version A
SO_2 Tissue oxygen saturation
SOP Standard Operating Procedure
SPAD Single-Photon Avalanche (Photon) Detector
SRS Stanford Research Systems
STED Stimulated emission depletion
SWaP Size, weight and power
SWI Susceptibility-weighted imaging
TBI Traumatic brain injury
TCD Transcranial doppler ultrasound
TCSPC Time-correlated single-photon counting
TD Time domain
TDC Time-to-digital converter
TD-DCS Time-Domain Diffuse Correlation Spectroscopy
TPSF Temporal point spread function
ToF Time of flight
US Ultrasound
U.S. United States
USB Universal Serial Bus
VCSEL Vertical-Cavity Surface-Emitting Laser
VECSELs Vertical External-Cavity Surface-Emitting Lasers

A.2 Equation nomenclature

Diffuse correlation spectroscopy

μ_a absorption coefficient
μ_s scattering coefficient
μ_s' reduced scattering coefficient
μ_t transport coefficient
L radiance
$\vec{r}$ position
Ω direction, solid angle
t time
τ delay
Φ fluence
G_1 unnormalized temporal multiple scattering electric field correlation
G_2 unnormalized temporal multiple scattering intensity correlation
g_1 normalized temporal multiple scattering electric field correlation
g_2 normalized temporal multiple scattering intensity correlation
E electric field

I electric field intensity
ρ source-detector separation
R_{eff} effective reflection coefficient
β ideality parameter

Semi-infinite homogeneous geometry

z_b boundary distance
z_0 isotropic source approximation distance
r_1 Euclidean distance to detector from approximated isotropic source
r_2 Euclidean distance to detector from negative imaging source
K scatterer displacement term
D photon diffusion coefficient

Fick's Principle

$q(t)$ quantity of a substance
F arterial blood flow
C_A arterial concentration of a substance
C_V venous concentration of a substance

Functional near-infrared spectroscopy

$\mathbf{w_a}$ fNIRS sensitivity to arterial compartments
$\mathbf{w_v}$ fNIRS sensitivity to venous compartments
HHb Deoxygenated (or deoxy-) hemoglobin
O_2Hb Oxygenated (or oxy-) hemoglobin
HbT Total hemoglobin concentration
HbO Concentration of oxy-hemoglobin
HbR Concentration of deoxy-hemoglobin
StO_2 Total blood oxygenation
SaO_2 Arterial blood oxygenation
SvO_2 Venous blood oxygenation
OEF Oxygen extraction fraction
HGB Hemoglobin concentration in blood
$\mathbf{MW_{Hb}}$ Molecular weight of hemoglobin
$\mathbf{D_{bt}}$ Brain tissue density

Laser properties

L_{coh} coherence length
$\Delta\nu$ linewidth
$\Delta\lambda$ wavelength bandwidth or linewidth
λ center frequency

Appendix B

Further theory

B.1 Solid angles

Units of steradians (sr) are for solid angles, which is a unitless measure analogous to the differential surface area of a sphere, as depicted in Figure B-1. The maximum steradian is 4π.

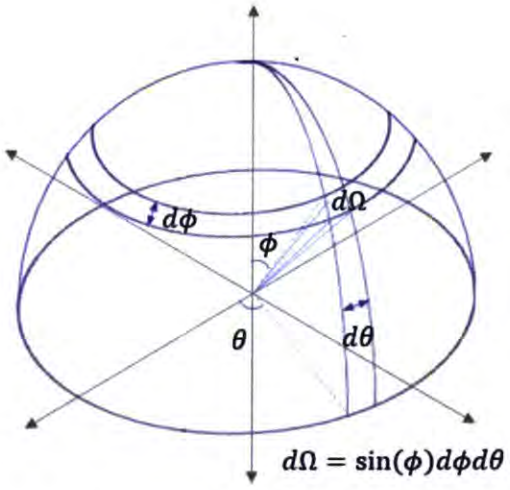

Figure B-1: Visualization of a solid angle. Omega is the solid angle, theta and phi are spherical coordinates.

B.2 Science, technology, and policy means and ends matrix

The matrix originally described in Section 5.1 includes representative examples of each element, which are described here to give a better understanding of how to navigate the matrix for improving policy-awareness of the user application. I will start in the bottom-left corner and work up to the top-right.

- ✓ Atoms can be categorized in the scientific-means-for-scientific-ends element because they are a scientific model that is used as a tool to help further scientific understandings of chemistry.

- ✓ Microscopes represent the engineering-and-technology-means-for-scientific-ends element because they are an observation technology that facilitates, and in some cases enables, scientific investigation of microscopic particles.

- ✓ Quantum computing is an example of the scientific-means-for-engineering-and-technology-ends element because the science and theory of quantum computing must continue to develop before it can be used in a marketable technology or to solve engineering problems.

- ✓ Gas pumps can be placed in the engineering-and-technology-means-for-engineering-and-technology-ends element because gas pumps are a technology that enables fossil fuel vehicle transportation, such as cars and airplanes, which are themselves technologies.

- ✓ Funding represents the policy-means-for-science-ends element because it is a policy to provide resources for science to continue.

- ✓ Lightning and NCAA (National Collegiate Athletic Association) is in the science means for policy ends element because the understanding of lightning developed by science has led to policies by the NCAA about how outdoor sports events are conducted in the detected presence of lighting within a certain radius of the sports field.

- ✓ Hackathons are characteristic of the policy-means-for-engineering-and-technology ends because they are a policy-guided strategy for encouraging concentrated thought on engineering and technology topics. Hackathons could also reasonably be in the policy-means-for-policy-ends element if the hackathon was focused on policy development, or the policy-means-for-science-ends element if the hackathon was focused on science. Hackathons are therefore also an excellent example for considering how a means can be reinterpreted to achieve different ends.

- ✓ Cell phones demonstrate the engineering-and-technology-means-for-policy-ends element because they are a technology that facilitates communication, which is critical for policy development and implementation.

- ✓ And finally, bureaucracy exemplifies the policy-means-for-policy-ends element because it is a set of policies that sustain other policies.

Appendix C

Standard Operating Procedures (SOPs)

Advanced fNIRS Testbed

Casey Evans – 5/31/18
Updated 5/15/19
Names have been redacted

Current State

As of now I have built histograms with one input source and one start signal. This has been done only with the CG/DG setup detailed below using the Lumics and QPhotonics laser diodes. I have also taken timestamps with one input and one start (raw data with no laser connected). As I see it, all the parts are here, we just need to put them together properly with D's help and then start working on detectors/lasers/miniaturization full throttle.

I've loaded most of the programs onto the Public folder. If they're inaccessible, N has copies of the AWG files, I provide a link for id900 software below and the MPD USBs that have been scanned by T are in the fiber bucket (please leave them there so that I know where to find them when I get back).

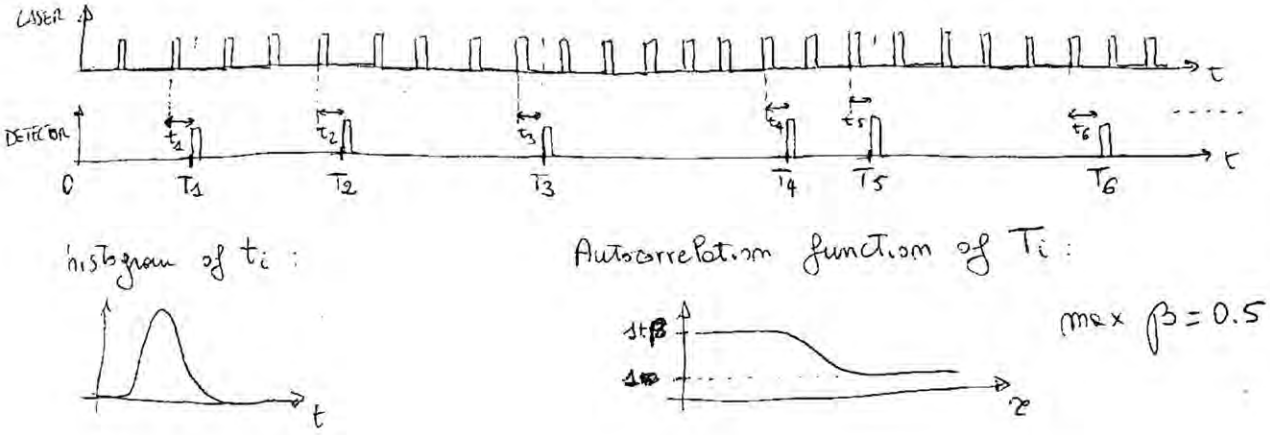

Figure 1: Current Understanding of what it is we need to measure (ti and Ti). Figure by Davide Tamborini.

TO DO

-Set up your desktop shortcuts on the lab computer – I recommend the FG SPAD interface, the ChaseScientific interface, the picosecond delayer interface, the id900 GUI and the SCPI client
~~-Follow up with R about answers to id900 questions (email chain)~~
~~-Work with NB to get 100um MPD SPAD shipped to and from MPD for upgrades, including detection head change to 50um and pigtailing for 5um fibers~~
-Follow up on coherence length measurements with D and A (for the Lumics, PicoQuant and Eagleyard lasers)
~~-Receive power meter and get a copy of the goods receipt to KR (keep one copy for records);~~

~~follow up if not received by 11 June 18~~
~~-Validate setup and data collection with D~~
-Work with R/S/Q to achieve post-simulation modification of attenuation coefficient (should be easy according to S and Q – ask them if you have issues)
-Ask X for TD-DCS code (if desired)
~~-Get guidance on how to proceed with MATLAB from D's thesis[1] to take our timestamps and turn them into TD-DCS data~~
-Find a way to interleave two lasers on either side of 805nm and collect data from each for usable TD-fNIRS data
-Create experiments that measure the testbed's ability to take TD-fNIRS and TD-DCS measurements together keeping in mind that the overall goal is to set up something that reliably takes measurements and that we can interchange detectors to test detector performance (first) and then interchange other parts to work towards miniaturization to a wearable device
-Consider packaging strategies
-Work on modeling all of the useful things
-All that completed: work on ways to miniaturize the device in SWaP, especially in ways that will make it less sensitive to motion artifacts

Procedures – when in doubt, read the manual, these SOPs are developed more or less from them

Working with the MPD SPAD

1. Turn on the big switch in the back of the SPAD control box
2. Open the FG SPAD program from the desktop
3. Enter the interface with the arrow at the top (select COM4)
4. Update settings (even if you don't update the settings, hit the button)
5. Hit turn on SPAD, this takes a minute or two
6. Hit start gate
7. I have been immediately switching to free gated mode and then hitting update gate, but feel free to try other gate settings
8. WHEN YOU'RE DONE hit stop gate
9. THEN hit turn off SPAD, this takes a minute or two
10. IF YOU DON'T DO #8 and #9 you can break the $22k SPAD – so do them if you haven't!!
11. Close the link
12. Turn of the big switch in the back of the SPAD control box

Working with the GUI[2]

1. Log in to the desktop
2. Unplug the LAN ethernet
3. AFTER #2, disable the endpoint security firewall (option under Quick links by clicking on the McAfee book in the lower right corner of the toolbar)
4. Input the reason "required for testing" or something similar and send
5. Click the TdGUI shortcut on the desktop
6. Operate histogram as you wish via the GUI, if you want to use timestamp blocks I recommend using the SCPI tab on the GUI or better yet, use the SCPI client (click on the shortcut on the desktop)

[1] https://github.com/dtyulman/tddcs
[2] If it's not downloaded on the Public folder for some reason, use this: http://idquantique.com/software/ID900_GUI_0_9.zip

7. Troubleshooting Tips (ie things that have worked in the past)
    a. If you don't see the pulse, expand the range to like 5us and then narrow back in on the pulse
    b. If it doesn't connect – close the GUI, turn on the firewall, plug in the LAN ethernet, wait until the computer recognizes it and then start again from #2. If it still doesn't connect, also try power cycling the id900.

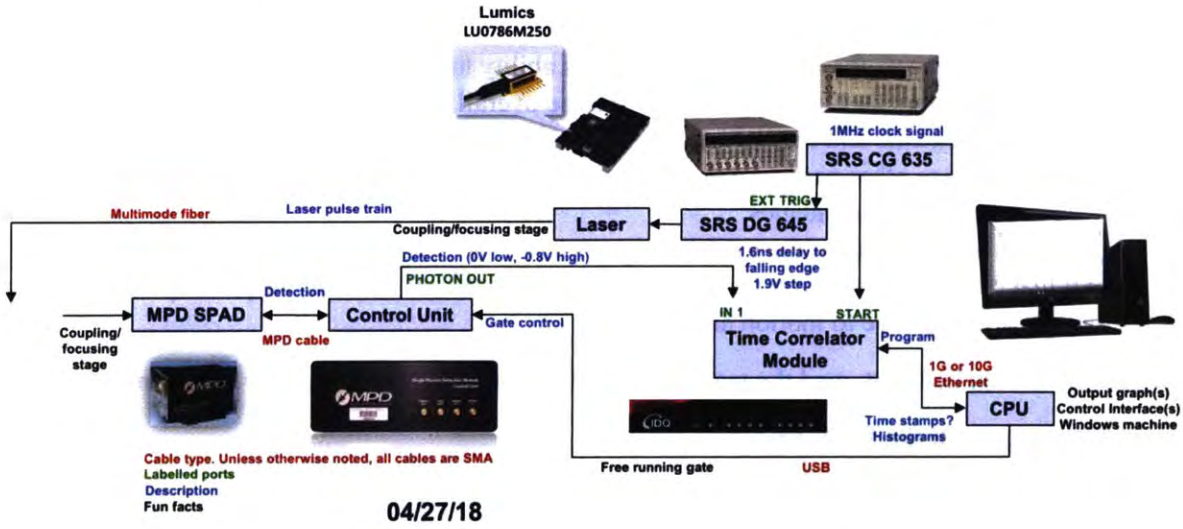

Figure 2: Overall lab setup (currently the only one used for histograms)

Figure 3: Histogram GUI example with TPSF from Human adipose tissue w/ 1cm perpendicular spacing w/105um fiber and Lumics laser diode using the setup from Figure 2

Working in SCPI Client

1. Follow steps 1-4 of "Working with the GUI"
2. Click the SCPI Client shortcut on the desktop (or do #5 from "Working with the GUI" and go to the SCPI Client tab, the figures below show the GUI interface)
3. Use the commands in the id900 User Manual with the following exceptions (**which need to be rechecked now that the new software and firmware has been installed**):
    a. Defaults – our device has some different defaults than the manual at least in the following areas
        i. input#:coupling is DC by default
        ii. sense#:mode is lowres by default
        iii. tsge#:enable is off by default
        iv. tsge#:mode is spulse by default
        v. tsco#:mode is coinc by default
        vi. tsco#:conf:coinc:width is 10ps by default
        vii. tsco#:conf:coinc:delay is 0ps by default
        viii. tsst#:inpo:mode is normal by default
        ix. tsst#:inpo:mode is 0ps by default
        x. tsst#:inpo:link is to sens# by default (with the exception of tsst5 which is unassigned)
        xi. tsst#:mode is counter by default
        xii. tsst#:inte is inf by default
        xiii. tsst#:save and tsst#:send are off by default
        xiv. tsst#:conf:histo:mode is mst by default when tsst#:mode is histo
        xv. tsst#:conf:histo:min is 0ps by default
        xvi. tsst#:conf:histo:bwid is 100ps by default
        xvii. tsst#:conf:histo:bcou is 100 by default
        xviii. tsst#:conf:histo:star:mode is normal by default
        xix. tsst#:conf:histo:star:delay is 0 by default
        xx. tsst#:conf:histo:star:link is star by default
    b. sour#:inpo:mode doesn't seem to update properly
    c. **sour#:inpo:delay stops the server – it's the worst, you'll have to restart everything like twice probably, so avoid this if you can**
    d. tsge#:conf:clock:per and tsge#:conf:spul:per seem to be invalid commands; possible reason: the indentation is incorrect in some places, so commands may be given incorrectly, also some commands are only valid if they are active
    e. tsco# seems to be limited to numbers 1-4 rather than 1-12
    f. tsco#:level? just returns the #
    g. everything under tsco#:inpo:fir and tsco#:inpo:sec seems to be invalid commands; possible reason: the indentation is incorrect in some places, so commands may be given incorrectly, also some commands are invalid if they are not active
    h. tsst# is limited to numbers 1-5 rather than 1-7

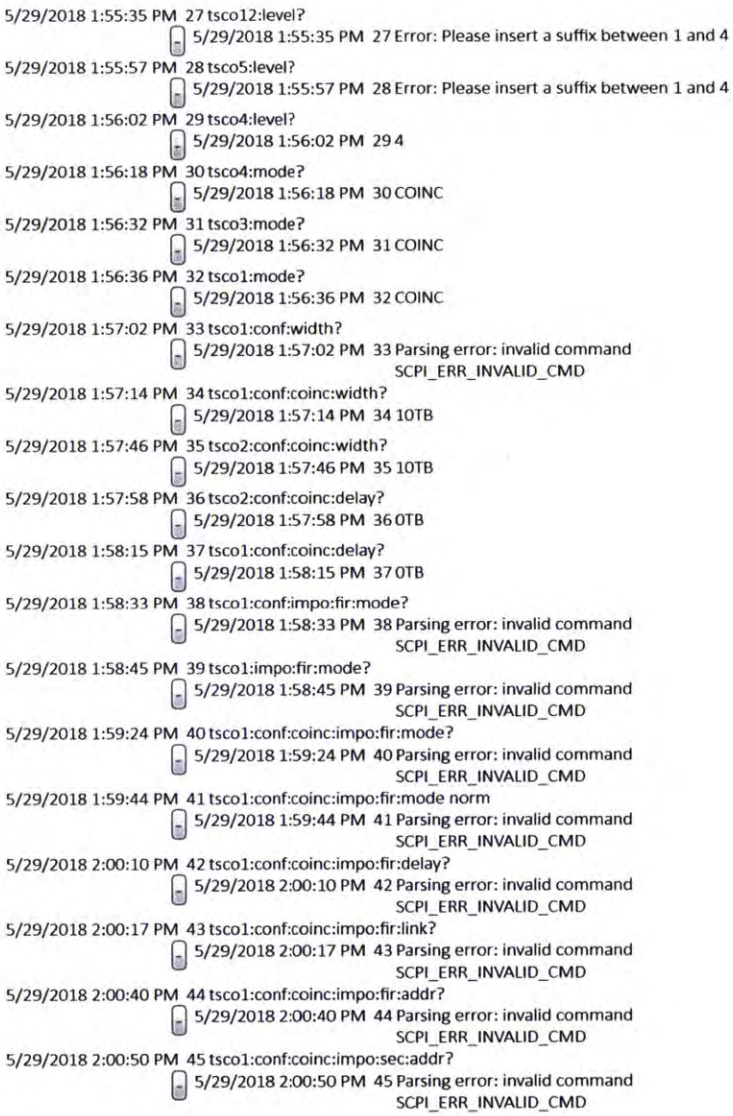

Figure 4: First Example of SCPI Client in GUI. Commands follow the number after the date and time in the nonindented lines, output follows the number after the date and time in the indented lines

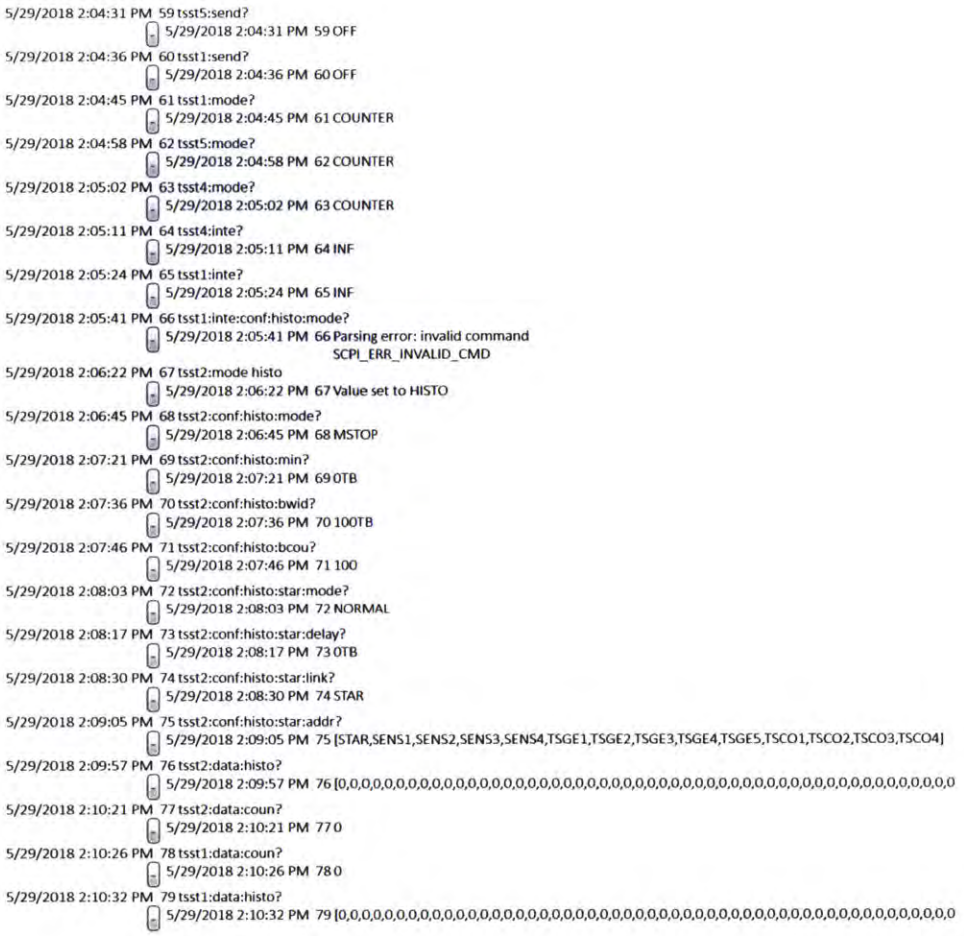

```
5/29/2018 2:04:31 PM  59 tsst5:send?
                  5/29/2018 2:04:31 PM  59 OFF
5/29/2018 2:04:36 PM  60 tsst1:send?
                  5/29/2018 2:04:36 PM  60 OFF
5/29/2018 2:04:45 PM  61 tsst1:mode?
                  5/29/2018 2:04:45 PM  61 COUNTER
5/29/2018 2:04:58 PM  62 tsst5:mode?
                  5/29/2018 2:04:58 PM  62 COUNTER
5/29/2018 2:05:02 PM  63 tsst4:mode?
                  5/29/2018 2:05:02 PM  63 COUNTER
5/29/2018 2:05:11 PM  64 tsst4:inte?
                  5/29/2018 2:05:11 PM  64 INF
5/29/2018 2:05:24 PM  65 tsst1:inte?
                  5/29/2018 2:05:24 PM  65 INF
5/29/2018 2:05:41 PM  66 tsst1:inte:conf:histo:mode?
                  5/29/2018 2:05:41 PM  66 Parsing error: invalid command
                                           SCPI_ERR_INVALID_CMD
5/29/2018 2:06:22 PM  67 tsst2:mode histo
                  5/29/2018 2:06:22 PM  67 Value set to HISTO
5/29/2018 2:06:45 PM  68 tsst2:conf:histo:mode?
                  5/29/2018 2:06:45 PM  68 MSTOP
5/29/2018 2:07:21 PM  69 tsst2:conf:histo:min?
                  5/29/2018 2:07:21 PM  69 0TB
5/29/2018 2:07:36 PM  70 tsst2:conf:histo:bwid?
                  5/29/2018 2:07:36 PM  70 100TB
5/29/2018 2:07:46 PM  71 tsst2:conf:histo:bcou?
                  5/29/2018 2:07:46 PM  71 100
5/29/2018 2:08:03 PM  72 tsst2:conf:histo:star:mode?
                  5/29/2018 2:08:03 PM  72 NORMAL
5/29/2018 2:08:17 PM  73 tsst2:conf:histo:star:delay?
                  5/29/2018 2:08:17 PM  73 0TB
5/29/2018 2:08:30 PM  74 tsst2:conf:histo:star:link?
                  5/29/2018 2:08:30 PM  74 STAR
5/29/2018 2:09:05 PM  75 tsst2:conf:histo:star:addr?
                  5/29/2018 2:09:05 PM  75 [STAR,SENS1,SENS2,SENS3,SENS4,TSGE1,TSGE2,TSGE3,TSGE4,TSGE5,TSCO1,TSCO2,TSCO3,TSCO4]
5/29/2018 2:09:57 PM  76 tsst2:data:histo?
                  5/29/2018 2:09:57 PM  76 [0,0,0,0,0,0,0,0,0,0,0,0,0,0,0,0,0,0,0,0,0,0,0,0,0,0,0,0,0,0,0,0,0,0,0,0,0,0,0,0,0,0,0,0,0,0,0,0,0,0,0,0,0,0,0,0,0,0,0,0
5/29/2018 2:10:21 PM  77 tsst2:data:coun?
                  5/29/2018 2:10:21 PM  77 0
5/29/2018 2:10:26 PM  78 tsst1:data:coun?
                  5/29/2018 2:10:26 PM  78 0
5/29/2018 2:10:32 PM  79 tsst1:data:histo?
                  5/29/2018 2:10:32 PM  79 [0,0,0,0,0,0,0,0,0,0,0,0,0,0,0,0,0,0,0,0,0,0,0,0,0,0,0,0,0,0,0,0,0,0,0,0,0,0,0,0,0,0,0,0,0,0,0,0,0,0,0,0,0,0,0,0,0,0,0,0
```

Figure 5: Second Example of SCPI Client in GUI. Commands follow the number after the date and time in the nonindented lines, output follows the number after the date and time in the indented lines

Working with the Lumics or QPhotonics laser diodes, a clock generator and delay generator

1. Turn on PicoLAS laser diode driver by quickly applying 5V (if you're current limited under 2A it may not start and if you're slow it may not start so you'll have to try again – fast as in human fast, not computer fast)
2. Turn on the CG to 1MHz (the top output is fine, ensure it's connected to the trigger of the DG)
3. Ensure the delay generator has a 10dB attenuator at the output
4. Turn on the delay generator set to trigger on the rising edge of the clock with a 1.9V pulse, and a 1.7ns delay to the falling edge it will output to the driver
5. Use the laser as you wish – these should be the narrowest pulses you can reasonably get at 1MHz – feel free to adjust in accordance with max power limitations of the device (DO NOT RUN DIODES at 1.9V at low frequencies)
6. Turn off DG
7. Turn off CG
8. Turn off power to laser diode driver

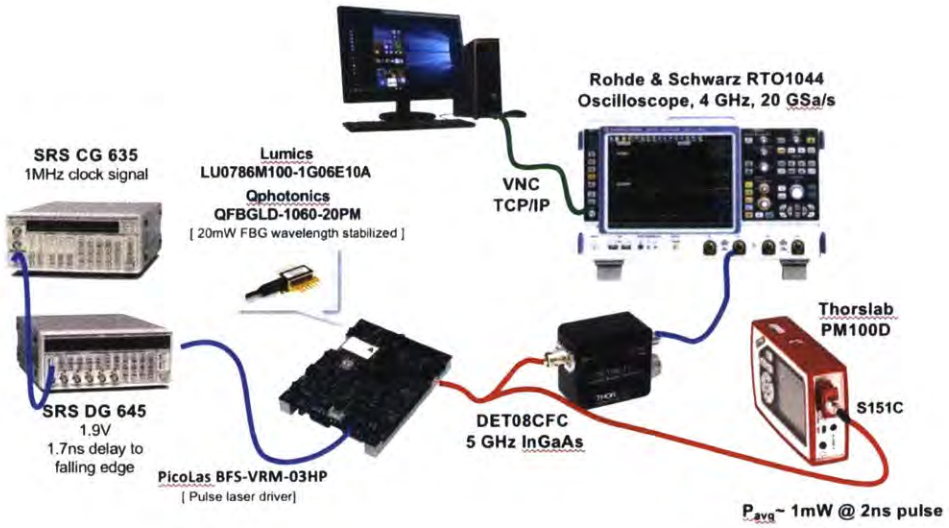

Figure 6: Setup for Laser Diodes and Clock Gen/Delay Gen

Working with the laser diodes and the Wavepond AWG

1. Turn on PicoLAS laser diode driver by quickly applying 5V (if you're current limited under 2A it may not start and if you're slow it may not start so you'll have to try again – fast as in human fast, not computer fast)
2. Connect power to AWG
3. Open the Labview program by selecting the ChaseScienceDAx14400_interactive file
4. Enter the program interface
5. Select the pulse shape you want
6. Hit update
7. Hit on
8. Connect the output of the AWG to the input of the laser diode driver
9. Make the best pulse shape ever!
10. Hit quit
11. Stop the interface program
12. Disconnect power to AWG

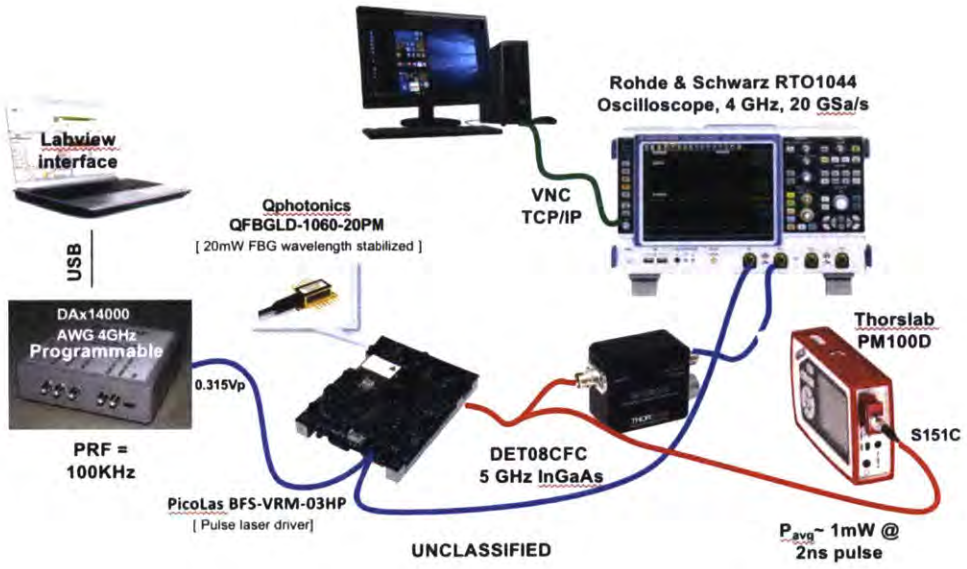

Figure 7: Setup for Laser Diodes and Wavepond AWG

Working with the laser diodes and the PicoLAS AWG

1. Connect the power leads from the driver to the AWG (the three screws on the one side – the outer screws are power (5V) and the center screw is ground (0V)). Make sure that the fan stays powered as well (the leads that are in there now).
2. Connect the trigger (T) to a 200kHz clock pulse (from 5V CMOS output)
3. Connect the signal (S) to the input of the laser diode driver
4. Attach the PicoLAS Universal Platform Interface
5. Power the devices by plugging the AWG into a wall
6. Use the AWG to select parameters of choice and enable the output (ex we used data settings at 0,0,6000)

Working with the PicoQuant laser

1. Wear protective lenses
2. Turn on the laser with the switch
3. You win. Turn it off when you're done

Coherence length via spectrum analysis

1. Ask politely to use an optical spectrum analyzer
2. Take the spectrum of the laser of choice
3. Calculate center wavelength squared divided by FWHM of the spectrum
4. Hopefully it's greater than 5cm

Coherence length via interferometry

1. Ask politely to use A's (talk to D, I don't know A personally) setup at BU
2. Or else set up an optical system where you vary the distance taken by two light streams split from the same source and sent to the same detector to measure the coherence length directly

Materials

-Purchased MPD SPADs (2)[3]
Came with picosecond delay modules (2)[4]

Came with software which can be found in a box on the desk (USBs that have been scanned by Tim)

-Purchased id900 time controller[5]
-Purchased Lumics 786nm laser diode[6]
-Found QPhotonics 1064nm laser diodes (2)[7]
-Borrowed Eagleyard 1064nm laser diode[8] with PicoLAS driver[9] from N
-Purchased Wavepond AWG[10]
-Borrowed a Stanford Research Systems Model DG645 Digital Delay Generator[11] from SA (indeterminate return date)
Purchased a fast rise time module from SRS
-Borrowed a Stanford Research Systems Model CG635 2.05GHz Synthesized Clock Generator[12] from RY (due back ~~now~~ a while ago)
~~-Can borrow an id810 from JL (if desired)~~
-Borrowed ThorLabs DET08CFC from N and ThorLabs DET025AL from SA (both with indeterminate return dates)
-Borrowed PicoLAS PLCS-40 (&BOB) AWG[13] from N
-Borrowed PicoLAS PLB-21 Universal Platform Interface[14] from SA
-Found/borrowed (O would know) a BK Precision 1672 DC Power Supply[15]
-Found a LeCroy HRO 64Zi 400MHz 2GS/s Oscilloscope[16]
-Purchased a PicoLAS driver[17]
-Purchased various optical equipment (patch cords, isolators, attenuators, splitters, connectors, power meter, fiber scope)[18]
-Found eye protection, IR viewer, IR cards, and various blades/screwdrivers/tools
-N has access to a ANDO optical spectrum analyzer AQ6317B and a Rohde & Schwarz RTO1044 4 GHz 20 GS/s Oscilloscope

---

[3] See MPD_SPAD_User_Manual_V1_0.pdf and MPD_SPAD_notes.pdf
[4] See PSD_User_Manual_V1_0.pdf
[5] See ID900_User_Manual_V0_9.pdf and id900_promises.pdf
[6] See Lumics_Datasheet.pdf
[7] See QPhotonics_Datasheet.pdf
[8] See Eagleyard_Datasheet.pdf (EYP-DFB-1064-00500-1500-BFY02-0010)
[9] See BFS-VRM-03_User_Manual_V1510.pdf
[10] See Wavepond_AWG_notes.pdf
[11] http://www.thinksrs.com/products/dg645.html
[12] http://www.thinksrs.com/products/cg635.html
[13] http://PicoLAS.de/product/plcs-40-2/ and see PCLS-40_Manual_Rev1601.pdf
[14] http://PicoLAS.de/product/plb-21/
[15] http://www.bkprecision.com/products/power-supplies/1672-triple-output-quad-display-dc-power-supply-2-0-32v-0-3a-15v-3a.html
[16] See LeCroy_Factsheet.pdf
[17] See BFS-VRM-03_User_Manual_V1510.pdf
[18] See OzOptics_Specs.pdf for some commentary on this

-A brought Silicon pigment, Si oil, and ink for phantoms; there may still be milk in the fridge too…

Resources

Basecamp
Chase
Email, phone, drop-ins, weekly meetings

Contacts (some of the people we've met with or talked to)

[CONTACT LIST HAS BEEN REDACTED]

Appendix D

Code Library

D.1 txttomat.m

```
% A collection of commands called in investigating the time controller
% by Casey Evans
% Prepared by: Casey Evans
% Last Updated: 17 May 2019
% Documentation:

%close all;
%clear all;

% Test 1: Ambient
fileIDb = fopen('id900_lltest/001_idq_test_20s.bin','r');
fpga_0 = fread(fileIDb,'short');
figure(1); plot(fpga_0(1:200));

fileIDb = fopen('id900_lltest/2018-08-24T10_48_01_C1.bin','r');
id900_0C1 = fread(fileIDb,'uint64','a');

fileIDb = fopen('id900_lltest/2018-08-24T10_48_01_C2.bin','r');
id900_0C2 = fread(fileIDb,'uint64','a');

fileIDb = fopen('id900_lltest/2018-08-24T10_48_01_C3.bin','r');
id900_0C3 = fread(fileIDb,'uint64','a');

% Test 2: Laser on
fileIDb = fopen('id900_lltest/001_idq_test_withlaser_20s.bin','r');
fpga_1 = fread(fileIDb,'uint64','a');

fileIDb = fopen('id900_lltest/2018-08-24T12_36_27_C1.bin','r');
id900_1C1 = fread(fileIDb,'uint64','a');

fileIDb = fopen('id900_lltest/2018-08-24T12_36_27_C2.bin','r');
id900_1C2 = fread(fileIDb,'uint64','a');

fileIDb = fopen('id900_lltest/2018-08-24T12_36_27_C3.bin','r');
id900_1C3 = fread(fileIDb,'uint64','a');

% First Difference
file0 = id900_0C2;
% It turns out there's also a function for this (diff)
diff1 = zeros(length(file0)-1,1);
for k=1:length(diff1)
    diff1(k)= file0(k+1)-file0(k);
end
max(diff1);
min(diff1);
nmax1=size(diff1(diff1==max(diff1)),1);
```

```
nmin1=size(diff1(diff1==min(diff1)),1);
probabilityMax1=nmax1/size(file0,1);
probabilityMin1=nmin1/size(file0,1);
period = mean(diff1)/10^12  % s
freq = 1/period   % Hz
variance = var(diff1)

% Eliminating asynchronous timestamps
% Detector timestamps taken before laser timestamps are ignored
% Laser timestamps taken after all detector timestamps are ignored
Tlas = id900_0C2;
Tlas = id900_0C1;
for k=1:length(Tlas)
    if Tdet(k)<Tlas(1)
        k = k+1;
    else
        break;
    end
end

% Computing the autocorrelation function
tstamps = floor(Tdet(k+1:end)/(10e9/80e6));
[acf, t] = pulse_xcorr_2stage(tstamps, tstamps, 80e6, 80e6, 0);
% Plotting the autocorrelation function
figure();
semilogx(t,acf,'LineWidth',3)
title('Autocorrelation Function','FontSize',18)
xlabel('Time Shift (s)','FontSize',14)
ylabel('Autocorrelation Function Intensity (units?)','FontSize',14)
grid on

% Est 80 MHz
% https://www.mathworks.com/matlabcentral/answers/20993-periodic-impulse-
train-train
f=80; %frequency of the impulse in Hz
fs=f*10; % sample frequency is 10 times higher
t=0:1/fs:1; % time vector
y80=zeros(size(t));
y80(1:fs/f:end)=1;

f=4; %frequency of the impulse in Hz
%fs=f*10; % sample frequency is 10 times higher
t=0:1/fs:1; % time vector
y4=zeros(size(t));
y4(1:fs/f:end)=1;
plot(t,y80,t,y4);
```

D.2 thesis.m

```
% Written by Casey Evans, 2019
% https://www.mathworks.com/matlabcentral/answers/29458-gaussian-distribution
% https://www.mathworks.com/matlabcentral/answers/364957-removing-xaxis-and-
yaxis-values
```

```
t = 0:0.001:1;

cw_source = ones(size(t));
fd_source = cos(2*pi*3*t)*0.5+0.5;
    sd = 0.005;
    mu = 0.1;
td_source = 1/(2*pi*sd)*exp(-(t-mu).^2/(2*sd^2));
td_source = td_source/max(td_source);

cw_out = 0.7*ones(size(t));
fd_out = 0.6*cos(2*pi*3*t-1)*0.5+0.5;
    sd2 = sd*5;
    mu2 = mu+0.3;
td_out = 1/(2*pi*sd2)*exp(-(t-mu2).^2/(2*sd2^2));
td_out = td_out/max(td_out);
    sd_tpsf = 20*sd;
    mu_tpsf = mu2;
    peak = find(td_out==max(td_out))+1;
    tpsf = 1/(2*pi*sd_tpsf)*exp(-(t(peak:end)-mu_tpsf).^2/(2*sd_tpsf^2));
    tpsf = tpsf/max(tpsf);
td_out(peak:end)= tpsf;
td_out = 0.9*td_out;

figure(1);
subplot(1,3,1);
plot(t,cw_source,t,cw_out,'LineWidth',3);
title('\fontsize{14}CW Approach');
xlabel('\fontsize{14}Time');
ylabel('\fontsize{14}Intensity');
xlim([min(t) max(t)]);
ylim([0 1.2]);
legend('Source','Measure');
set(gca,'XTick',[], 'YTick', []);

figure(1);
subplot(1,3,2);
plot(t,td_source,t,td_out,'LineWidth',3);
title('\fontsize{14}TD Approach');
xlabel('\fontsize{14}Time');
ylabel('\fontsize{14}Intensity');
xlim([min(t) max(t)]);
%ylim([0 1.2]);
legend('Source','Measure');
set(gca,'XTick',[], 'YTick', []);

figure(1);
subplot(1,3,3);
plot(t,fd_source,t,fd_out,'LineWidth',3);
title('\fontsize{14}FD Approach');
xlabel('\fontsize{14}Time');
ylabel('\fontsize{14}Intensity');
xlim([min(t) max(t)]);
ylim([0 1.2]);
legend('Source','Measure');
set(gca,'XTick',[], 'YTick', []);
```

D.3 pulse_xcorr_2stage.m

```
% Code provided by Optics @ Martinos Center for Biomedical Imaging
function [acf, t] = pulse_xcorr_2stage(tstamps, tstamps_shift, max_lag,
samplef, elimi)
% pulse_corr_2stage - 2-stage pulse autocorrelation
%  [acf, t] = pulse_corr_2stage(tstamps, max_lag, samplef, elimi)
%  acf - computed autocorrelation bins
%  t - lag time of computed bins in [s]
%  max_lag - maximum lag time to compute in samplef [periods]
%  samplef - 1/timestamps_resolution (e.g. 150e6)
%  elimi - number of bins to be removed from the start
%
%
%  written by Kuan-Cheng (Tony) Wu & Bernhard Zimmermann
%  MGH May 2016
%  with ideas from:
%  Emmanuel Schaub, "High countrate real-time FCS using F2Cor," Opt. Express
21, 23543-23555 (2013)
%  Davide Magatti and Fabio Ferri, "Fast multi-tau real-time software
correlator for dynamic light scattering," Appl. Opt. 40, 4011-4021 (2001)

P = 20;
m = 2;

navg = length(tstamps)/(tstamps(end)-tstamps(1));
K = round(log(1/navg)/log(2)) +1;

ncorr = ceil(log(max_lag/P)/log(m))+1;
% K = 12;
K = max(min(K, ncorr+1), 2);

% do the 2-stage algorithm
acf = zeros(1,P+P/m*(ncorr-1));
t = zeros(size(acf));

tstamps_rebin = unique(tstamps);
tstamps_counts = hist(tstamps,tstamps_rebin);

tstamps_rebin_shift = unique(tstamps_shift);
tstamps_counts_shift = hist(tstamps_shift,tstamps_rebin_shift);

% for short lag times, use normal pulse acf
ic = 1;
iclast = ic;
[acf_temp,t_temp]=pulse_xcorr_zero(tstamps_rebin,tstamps_rebin_shift,tstamps_
counts,tstamps_counts_shift,P*m.^(K-2),samplef/(m^(ic-1)));

    acf_temp_rebin = zeros(1,P + (P/m)*(K-2));
    t_temp_rebin = zeros(1,P + (P/m)*(K-2));

    acf_temp_rebin(1:P) = acf_temp(2:(P+1));
    t_temp_rebin(1:P) = t_temp(2:(P+1));
```

```
    % rebin result into exponentially sized bins
    for ib = 0:(K-3)
        rbsel = P+ib*P/m+(1:P/m);
        orsel = P*m.^ib + 1 + (m^(ib+1))*(0:(P/m)-1);
        for is = 0:(m^(ib+1)-1)
            acf_temp_rebin(rbsel)=acf_temp_rebin(rbsel)+acf_temp(orsel+is);
        end
        acf_temp_rebin(rbsel)=acf_temp_rebin(rbsel)./(m^(ib+1));
        t_temp_rebin(rbsel)=t_temp(orsel);
    end

    acf(1:P + (P/m)*(K-2)) = acf_temp_rebin;
    t(1:P + (P/m)*(K-2)) = t_temp_rebin;

    % for long lag times, use multi-tau approach
    for ic = K:ncorr
      [tstamps_rebin,~,indc]=unique(round(tstamps_rebin/(m^(ic-iclast))));
      tstamps_counts_new=zeros(size(tstamps_rebin));
      [tstamps_rebin_shift,~,indc_shift]=unique(round(tstamps_rebin_shift/(m^
      (ic-iclast))));
      tstamps_counts_new_shift=zeros(size(tstamps_rebin_shift));
      for is = 1:length(indc)
            tstamps_counts_new(indc(is))=tstamps_counts_new(indc(is))+tstamps
            _counts(is);
      end
      tstamps_counts = tstamps_counts_new;
      for is = 1:length(indc_shift)
            tstamps_counts_new_shift(indc_shift(is))=tstamps_counts_new_shift
            (indc_shift(is))+tstamps_counts_shift(is);
      end
      tstamps_counts_shift=tstamps_counts_new_shift;
[acf_temp,t_temp]=pulse_xcorr_zero(tstamps_rebin,tstamps_rebin_shift,tstamps_
counts,tstamps_counts_shift,P,samplef/(m^(ic-1)) );
        acf(P+(P/m)*(K-2)+(ic-K)*P/m+(1:P/m))=acf_temp((P/m+2):end);
        t(P+(P/m)*(K-2)+(ic-K)*P/m+(1:P/m))=t_temp((P/m+2):end);
        iclast=ic;
    end
    acf=acf(elimi+1:end);
    t=t(elimi+1:end);
end

function [acf, t] =
pulse_xcorr_zero(apd_r_fixed,apd_r_shift,apd_r_counts,apd_r_counts_shift,max_
lag,samplef)
acf = zeros(1,max_lag+1);
bi_start = 1;
for ai = 1:length(apd_r_shift)
   notset = true;
   for bi = bi_start:length(apd_r_fixed)
       temp_delta = apd_r_fixed(bi)-apd_r_shift(ai) ;
       if (temp_delta >= 0)
           if (temp_delta <= max_lag)
                  acf(temp_delta+1) = acf(temp_delta+1) +
                  apd_r_counts(bi)*apd_r_counts_shift(ai);
              if notset
                  notset = false;
```

```
                    bi_start = bi;
                end
            else
                break;
            end
        end
    end
end
acf = (max([(apd_r_fixed(end)-apd_r_fixed(1)),(apd_r_shift(end)-
apd_r_shift(1))])/(sum(apd_r_counts)*sum(apd_r_counts_shift))).*acf;
t = ((0:max_lag).*(1/samplef));
end
```

D.4 get_betaBFifit_TD.m

```
% Code provided by Optics @ Martinos Center for Biomedical Imaging
function [beta, BFi, fit_curve, t, err, err_ave] =
get_betaBFifit_TD(acf,t,lamda,mue_a,mue_sp,s,n,varargin)
switch nargin
    case 8
        max_acf = max(acf); min_acf = min(acf);
        ratio_low = varargin{1};
        thres_low = min_acf + (max_acf-min_acf)*ratio_low;
        for i = length(acf):-1:1
            if acf(i) >= thres_low
                t = t(1:i);
                acf = acf(1:i);
                break;
            end
        end
    case 9
        max_acf = max(acf); min_acf = min(acf);
        ratio_low = varargin{1};
        ratio_high = varargin{2};
        thres_low = min_acf + (max_acf-min_acf)*ratio_low;
        thres_high = min_acf + (max_acf-min_acf)*ratio_high;
        for i = length(acf):-1:1
            if acf(i) >= thres_low
                t = t(1:i);
                acf = acf(1:i);
                break;
            end
        end
        for i = 1:length(acf)
            if acf(i) <= thres_high
                t = t(i:end);
                acf = acf(i:end);
                break;
            end
        end
    otherwise
end
%~~~~~~~~~~~~~~~~!~~~~~~~~~~~~~~~!
%ex_BFi = 2.5*10^(-9); %cm >> nm
%rho = 2.5;%2.5 cm >> nm if rat, use 0.5
```

```
% n = 1.33;%1.37;
% lamda = 780*10^(2-9);%852*10^(2-9);%nm
% mue_a = 0.042;%cm-1 >> nm-1 if rat, use 0.1191
% mue_sp = 5.2;%cm-1 >>nm-1 if rat, use 3.7
%----------------
k0 = 2*pi/lamda; % Free-space wavenumber
k = k0*n; % Wavenumber in tissue
%ltr = 1/(mue_a+mue_sp); % Transport mean-free path
%Reff = -1.44*n^-2+0.71/n+0.00636*n+0.668; % Effective reflection coefficient
%----------------
%z0 = ltr;
%zb = 2/3*ltr*(1+Reff)/(1-Reff);
%r1 = sqrt(rho^2+z0^2);
%rb = sqrt(rho^2+(z0+2*zb)^2);
%~~~~~~~~~~~~~~~~~~~!~~~~~~~~~~~~~~~~~~~!
options = optimoptions('lsqnonlin','Display','off');
x0 = [0.5,3.2];
%tau0 = 1/150e6;%t(1);%
%K = @(tau,BFi)sqrt(3*mue_a*mue_sp+6*mue_sp^2*k^2*BFi*tau);
%g1 = @(tau,BFi)(exp(-K(tau,BFi)*r1)/r1-exp(-K(tau,BFi)*rb)/rb)/(exp(-
K(tau0,BFi)*r1)/r1-exp(-K(tau0,BFi)*rb)/rb);
g1 = @(tau,BFi) exp( -2*mue_sp*BFi*k^2*s*tau );
fun0 = @(x)(1+x(1).*(abs(g1(t,x(2).*1e-9)).^2)-acf');
[fixed_x,err] = lsqnonlin(fun0,x0,[],[],options);
beta = fixed_x(1);
BFi = fixed_x(2)*1e-9;
fit_curve = fun0(fixed_x)+acf';
err_ave = err./length(fit_curve);
```

D.5 config.txt

```
% Code provided by IDQuantique for ID900
TSST1:INPO:LINK TSCO5
TSST1:HISTO:STAR:LINK STAR
TSST1:RAW:STAR:LINK STAR

TSST2:INPO:LINK TSCO5
TSST2:HISTO:STAR:LINK TSCO8
TSST2:RAW:STAR:LINK TSCO8

TSCO8:OPIN ONLYSEC
```

Bibliography

[1] Plott, Charles. (1994). *Market Architectures, Institutional Landscapes and Testbed Experiments.* Economic Theory. 4. 3-10. 10.1007/BF01211116.

Describes the use of testbeds in social science and economics. Considers group to individual tensions and testbeds designed to either best capture data or best inform the model. Plott also suggests a few design principles. In general, full of interesting ideas and one of the main inspirations for this thesis.

[2] Rodger Pielke, *Forests, Tornadoes, and Abortion: Thinking About Science, Politics and Policy*, 2004, at 144.

[3] Casey Evans, *The Berlin Airlift and the Implications of Large-Scale Air Transportation*, 2016.

[4] Wallace, Gregory. "Aviation World Faces Moment of Reckoning after 737 MAX Crashes." *CNN*, Cable News Network, 7 Apr. 2019, www.cnn.com/2019/04/07/politics/boeing-aviation-737-max-aftereffects/index.html.

[5] Discours de Sylvie Bermann, Ambassadeur de France en Chine: https://www.youtube.com/watch?v=hLzyRmaSawM

[6] Langdon Winner, *Frankenstein's Problem: Autonomous Technology*, 1977, at 141-146.

[7] Alvin M. Weinberg, *Science and Trans-Science*, 1992, at 209-211.

[8] Mary Tiles and Hans Oberdiek, *Living in a Technological Culture: Human Tools and Human Values*, 1995, at 28.

[9] Neil Salkind, *Encyclopedia of Research Design*, 2010, at 1579-1580.

[10] Deborah Stone, *Policy Paradox: The Art of Political Decision Making*, 2012, in Chapter 8.

[11] Owen D. Jones, Jeffrey D. Schall, and Francis X. Shen, *Law and Neuroscience*, 2014, at 152.

[12] *Frye v. United States*, 293 F. 1014 (D.C. Cir. 1923).

[13] *Daubert v. Merrell Dow Pharma., Inc.*, 509 U.S. 579 (1993).

[14] Federal Rules of Evidence 401-403, 702.

[15] Danielle Wood, *Partnerships to enable earth science applications*, 2017, at 6.

[16] Douglas McKechnie. USAFA course notes Law 220S (Spring 2015).

[17] Donald Schön, *Metaphor and Thought*, 1993, Chapter 9, at 137.

[18] Peter-Paul Verbeek, *Materializing Morality: Design Ethics and Technological Mediation*, 2006.

[19] Boas, David A. *Diffuse photon probes of structural and dynamical properties of turbid media: theory and biomedical applications*. Diss. Graduate School of Arts and Sciences, University of Pennsylvania, 1996.

[20] U.S. patent no. US6076010A, 1996.

[21] Boas, David A., and Arjun G. Yodh. "Spatially varying dynamical properties of turbid media probed with diffusing temporal light correlation." *JOSA A* 14.1 (1997): 192-215.

[22] Cheung, Cecil, et al. "In vivo cerebrovascular measurement combining diffuse near-infrared absorption and correlation spectroscopies." *Physics in Medicine & Biology* 46.8 (2001): 2053.

[23] Yodh, Arjun, and Britton Chance. "Spectroscopy and imaging with diffusing light." *Physics Today* 48.3 (1995): 34-41.

[24] Zhou, Chao. "In-Vivo Optical Imaging and Spectroscopy of Cerebral Hemodynamics." PhD Dissertation. *University of Pennsylvannia*, 2007.

Excellent resource for introductory theory to light based measurements of biological processes in the brain. Focuses on DCS, including Monte Carlo simulations and noise modelling followed by validations in animal and human models. Does not consider gated DCS. BFi cross-validation studies listed on page 36.

[25] Kim, Meeri Nam. "Applications of hybrid diffuse optics for clinical management of adults after brain injury." (2013).

[26] Li, Xingde. *Fluorescence and diffusive wave diffraction tomographic probes in turbid media*. Diss. University of Pennsylvania, 1998.

[27] Shang, Yu, Katelyn Gurley, and Guoqiang Yu. "Diffuse correlation spectroscopy (DCS) for assessment of tissue blood flow in skeletal muscle: recent progress." *Anatomy & physiology: current research* 3.2 (2013): 128.

[28] Guoqiang Yu et al., *Near-Infrared Diffuse Correlation Spectroscopy for Assessment of Tissue Blood Flow*, 2011, at 207.

[29] Cheng, Xiaojun, et al. "Time domain diffuse correlation spectroscopy: modeling the effects of laser coherence length and instrument response function." *Optics letters* 43.12 (2018): 2756-2759.

[30] Tyulmankov, Danil. *Time-domain diffuse correlation spectroscopy: instrument prototype, preliminary measurements, and theoretical modeling*. Diss. Massachusetts Institute of Technology, 2017.

[31] Sutin, Jason, et al. "Time-domain diffuse correlation spectroscopy." *Optica* 3.9 (2016): 1006-1013.

Core DCS theory paper for the Martinos Center and Lincoln collaborators. The supplementary material considers motion in the liquid phantom and other interesting experimental results. BFi cross-validation studies listed on page 1006.

[32] Megan Blackwell, *Advanced Functional Near Infrared Spectroscopy*, 2017, at 1.

[33] Pei-Yi Lin et al., *Reduced cerebral blood flow and oxygen metabolism in extremely preterm neonates with low-grade germinal matrix- intraventricular hemorrhage*, 2016, at 1.

[34] Roche-Labarbe et al., *Noninvasive optical measures of CBV, StO2, CBF Index, and rCMRO2 in human premature neonates' brains in the first six weeks of life*, 2010, author manuscript at 1.

[35] Madsen, Steen J., ed. *Optical methods and instrumentation in brain imaging and therapy*. Vol. 3. Springer Science & Business Media, 2012.

[36] Faber, Dirk J., et al. "Oxygen saturation-dependent absorption and scattering of blood." *Physical review letters* 93.2 (2004): 028102.

[37] Ackerson, B. J., et al. "Correlation transfer-application of radiative transfer solution methods to photon correlation problems." *Journal of thermophysics and heat transfer* 6.4 (1992): 577-588.

[38] Sun, Bo, et al. "A practical analytic single scattering model for real time rendering." *ACM Transactions on Graphics (TOG)*. Vol. 24. No. 3. ACM, 2005.

[39] Reeks, M. W. "The relationship between Brownian motion and the random motion of small particles in a turbulent flow." *The Physics of fluids* 31.6 (1988): 1314-1316.

[40] Haskell, Richard C., et al. "Boundary conditions for the diffusion equation in radiative transfer." *JOSA A* 11.10 (1994): 2727-2741.

[41] Magatti, Davide, and Fabio Ferri. "Fast multi-tau real-time software correlator for dynamic light scattering." *Applied Optics* 40.24 (2001): 4011-4021.

Excellent high-level descriptions of DLS and why autocorrelation is central to the modality.

[42] Schaub, Emmanuel. "High countrate real-time FCS using F2Cor." *Optics express* 21.20 (2013): 23543-23555.

Breaks down ACF math as it is done in the MATLAB function used for DCS at the Martinos Center. I don't really understand it yet though.

[43] Mazhar, Amaan, et al. "Laser speckle imaging in the spatial frequency domain." *Biomedical optics express* 2.6 (2011): 1553-1563.

[44] Davies, David James, et al. "Frequency-domain vs continuous-wave near-infrared spectroscopy devices: a comparison of clinically viable monitors in controlled hypoxia." *Journal of clinical monitoring and computing* 31.5 (2017): 967-974.

Comments on frequency domain methods. Also has optical properties for a five layer model of the human head. Includes a noise model and discussion of depth sensitivity improvements with TD-DCS.

[45] Selb, Juliette J., et al. "Improved sensitivity to cerebral hemodynamics during brain activation with a time-gated optical system: analytical model and experimental validation." *Journal of biomedical optics* 10.1 (2005): 011013.

[46] Torricelli, Alessandro, et al. "Time domain functional NIRS imaging for human brain mapping." *Neuroimage* 85 (2014): 28-50.

The primary time domain NIRS paper referenced at Lincoln Laboratory.

[47] Sato, Chie, et al. "Estimating the absorption coefficient of the bottom layer in four-layered turbid mediums based on the time-domain depth sensitivity of near-infrared light reflectance." *Journal of biomedical optics* 18.9 (2013): 097005.

[48] Franceschini, Maria A. "Validation of time-domain near-infrared spectroscopy and diffuse correlation spectroscopy for baseline measurement of brain physiology." Detailed protocol. 11 Jan 2018.

[49] Zazulia, Allyson R., Joanne Markham, and William J. Powers. "Cerebral blood flow and metabolism in human cerebrovascular disease." *Stroke*. WB Saunders, 2011. 44-67.

[50] Angrist, Joshua D., and Jörn-Steffen Pischke. *Mastering 'Metrics: The path from cause to effect*. Princeton University Press, 2014.

[51] TD-DCS grant proposal for MITLL and Optics @ Martinos, 2017;2019.

[52] Stenger, Michael B., et al. "Evidence Report: Risk of Spaceflight Associated Neuro-ocular Syndrome (SANS)." (2017).

[53] Lorenzo Vigano master's thesis, *Modeling Torso Imaging via Time-Domain Diffuse Correlation Spectroscopy*, 2019.

[54] NASA grant proposal, Megan Blackwell, 2018.

[55] Brian W. Pogue, *Optics and Photonics News: Optics in the Molecular Imaging Race*, 2015.

A well-illustrated set of comparisons between different biomedical imaging modalities across the EM spectrum. Considers different detectable features, cost, system lifetimes for optical, CT, PET, MRI and combined systems.

[56] Bunge, Silvia A., and Itamar Kahn. "Cognition: An overview of neuroimaging techniques." (2009): 1063-1067.

Considers anatomical versus functional techniques. Includes one of the size-time resolution charts. Discusses optical methods, MRI, MEG, EEG, PET and lesions. Some comments on advantages of different techniques, goals and resolutions as well as what can be learned from such studies.

[57] Jonmohamadi, Yaqub, et al. "Constrained temporal parallel decomposition for EEG-fMRI fusion." *Journal of neural engineering* 16.1 (2018): 016017.

[58] De Pasquale, Francesco, et al. "Temporal dynamics of spontaneous MEG activity in brain networks." *Proceedings of the National Academy of Sciences* 107.13 (2010): 6040-6045.

[59] For price comparison, I used a quick internet search to corroborate the AfNIRS 2017 presentation by Megan Blackwell. The sites used were https://www.wired.com/2007/01/meg-scanners-are-mega-powerful/ and https://imotions.com/blog/eeg-headset-prices/.

[60] Eugene Lin and Adam Alessio, *What are the basic concepts of temporal, contrast, and spatial resolution in cardiac CT?*, 2009, Author Manuscript at 10.

[61] Thomas Deffieux et al, *Functional ultrasound neuroimaging: a review of the preclinical and clinical state of the art*, 2018, at 130.

[62] M. Akif Topcuoglu, *Transcranial Doppler ultrasound in neurovascular diseases: diagnostic and therapeutic aspects*, 2012, at 40-41.

[63] Personal conversation with Lauren O'Donnell, Assistant Professor of Radiology, Harvard Medical School, 2019.

[64] Casey Evans, *Brain Imaging Techniques in 2017*, 2017, at 13.

[65] Sironi et al., *Optical Blood Flow Measurement in Microcirculatory Systems*, 2016.

Compares resolution (lateral, depth, spatial, temporal) and invasiveness of optical techniques including DCS, OCT and LSCI.

[66] Strangman, Gary E., Zhi Li, and Quan Zhang. "Depth sensitivity and source-detector separations for near infrared spectroscopy based on the Colin27 brain template." *PloS one* 8.8 (2013): e66319.

[67] Stephen J. Matcher, *Chapter 27: Optical Oximetry* from *Handbook of Biophotonics: Vol 2: Biophotonics for Healthcare* Editor: Jürgen Popp et al., 2012, at 446.

[68] http://nirx.net/nirsport/

[69] Personal conversation with Stefan Carp, Optics @ Martinos, 2019.

[70] Robinson, Mitchell et al. Quantitative depth selective measurements of flow using acousto-optic diffuse correlation spectroscopy. SPIE presentation 2019.

[71] Tsalach, Adi, et al. "Depth selective acousto-optic flow measurement." *Biomedical optics express* 6.12 (2015): 4871-4886.

[72] Maria Franceschini, principal investigator at the Martinos Center for Biomedical Imaging, personal conversation, 2018.

[73] "Advanced Imager Technology." *MIT Lincoln Laboratory*, 2019, www.ll.mit.edu/r-d/advanced-technology/advanced-imager-technology.

[74] Hecht, Eugene. *Optics*. 5th ed., Pearson, 2017.

[75] Dragoo, Tadja, and Michael W. Davidson. "Explanations on the Concept of Coherence of Light." *Zeiss*, 2019, www.zeiss.com/microscopy/int/solutions/reference/all-tutorials/light-sources/coherence-of-light.html.

[76] Paschotta, Rüdiger. "Transform Limit." *RP Photonics Encyclopedia - Transform Limit, Pulse Duration*, 23 Oct. 2017, www.rp-photonics.com/transform_limit.html.

[77] Paschotta, Rüdiger. "Sech2-Shaped Pulses." *RP Photonics Encyclopedia - sech2-Shaped Pulses, Hyperbolic Secant, Solitons*, 20 Oct. 2018, www.rp-photonics.com/sech2_shaped_pulses.html.

[78] Oleg Shatrovoy laser design selection slides at MITLL weekly meeting, 2017.

[79] ANSI Z136.1—2007 Table 8a page 78: *Limiting Apertures (Irradiance and Radiant Exposure) and Limiting Cone Angles (Radiance and Integrated Radiance) for Hazard Evaluation*

[80] Jacques, Steven L. "Optical properties of biological tissues: a review." *Physics in Medicine & Biology* 58.11 (2013): R37.

[81] Oleg Shatrovoy, memorandum of justification for PicoQuant laser, 2018.

[82] Niyom Lue. UpdateLDs presentation, 2018.

[83] Niyom Lue. UpdateShortenPicoquant presentation, 2018.

[84] Sato, Tsukuru, et al. "Dual-energy high-count-rate X-ray computed tomography scanner using a cerium-doped yttrium aluminum perovskite crystal and a small-photomultiplier tube." *Health and Technology* 8.3 (2018): 179-187.

[85] Lee, Jae Sung, and Seong Jong Hong. "Geiger-mode avalanche photodiodes for PET/MRI." *Electronics for Radiation Detection*(2018): 179.

[86] Tamborini, Davide, et al. "Superconducting nanowire single-photon detectors for Diffuse Correlation Spectroscopy." *Optics and the Brain*. Optical Society of America, 2019.

[87] Natarajan, Chandra M., Michael G. Tanner, and Robert H. Hadfield. "Superconducting nanowire single-photon detectors: physics and applications." *Superconductor science and technology* 25.6 (2012): 063001.

[88] "Chapter 4: Diodes." *Microelectronic Circuits*, by Adel S. Sedra and Kenneth Carless. Smith, Oxford University Press, 2011, pp. 152–154.

[89] Rajeev Ram. MIT course notes for 6.731: Semiconductor Optoelectronics (Spring 2019).

[90] MPD Fast Gated SPAD User Manual

[91] Chuang, Shun Lien. *Physics of photonic devices*. Vol. 80. John Wiley & Sons, 2012.

[92] Cova, Sergio, et al. "Avalanche photodiodes and quenching circuits for single-photon detection." *Applied optics* 35.12 (1996): 1956-1976.

[93] Baliga, Jayant. "Modern power devices." (1987).

[94] Gersbach, Marek, et al. "A low-noise single-photon detector implemented in a 130 nm CMOS imaging process." *Solid-State Electronics* 53.7 (2009): 803-808.

[95] Zhang, Jun, et al. "Advances in InGaAs/InP single-photon detector systems for quantum communication." *Light: Science & Applications* 4.5 (2015): e286.

[96] Personal conversation with Brian Aull, MITLL, 2019.

[97] MITLL weekly meeting slides 2017-2019

[98] Malass, Imane, et al. "Parallelized Integrated Time-Correlated Photon Counting System for High Photon Counting Rate Applications." *Photon Counting-Fundamentals and Applications*. IntechOpen, 2017.

[99] Aull, Brian F., et al. "Large-Format Geiger-Mode Avalanche Photodiode Arrays and Readout Circuits." *IEEE Journal of Selected Topics in Quantum Electronics* 24.2 (2017): 1-10.

[100] Personal conversation with George Jordy, MITLL, 2019.

[101] Personal conversation with Robert Berger, MITLL, 2019.

[102] Personal conversation with Megan Blackwell, MITLL, 2019.

[103] Fang, Qianqian. "Mesh-based Monte Carlo method using fast ray-tracing in Plücker coordinates." *Biomedical optics express*1.1 (2010): 165-175.

[104] Personal conversation with Davide Tamborini, Optics @ Matrinos, 2019.

[105] Flock, Stephen T., et al. "Optical properties of Intralipid: a phantom medium for light propagation studies." *Lasers in surgery and medicine* 12.5 (1992): 510-519.

[106] Li, Jun, et al. "Analytical models for time-domain diffuse correlation spectroscopy for multi-layer and heterogeneous turbid media." *Biomedical optics express* 8.12 (2017): 5518-5532.

[107] Adapted from a personal conversation with Dan Ripin of MITLL, 2018.

[108] McCray, Lawrence E., Kenneth A. Oye, and Arthur C. Petersen. "Planned adaptation in risk regulation: An initial survey of US environmental, health, and safety regulation." *Technological Forecasting and Social Change* 77.6 (2010): 951-959.

To Learn More

Bashkatov, Alexey N., et al. "Optical properties of human cranial bone in the spectral range from 800 to 2000 nm." *Saratov Fall Meeting 2005: Optical Technologies in Biophysics and Medicine VII*. Vol. 6163. International Society for Optics and Photonics, 2006.

Blackwell, et al. Focal Plane Arrays for Time-Gated Functional Diffuse Correlation Spectroscopy.

Bryan Jr, R. M. "Cerebral blood flow and energy metabolism during stress." *American Journal of Physiology-Heart and Circulatory Physiology* 259.2 (1990): H269-H280.

Buckley, Erin M., et al. "Diffuse correlation spectroscopy for measurement of cerebral blood flow: future prospects." *Neurophotonics* 1.1 (2014): 011009.

Considers optical neuroimaging application of DCS in comparison with other neuroimaging modalities. Also considers limitations and possible future uses.

Burns, Terry W., D. John O'Connor, and Susan M. Stocklmayer. "Science communication: a contemporary definition." *Public understanding of science* 12.2 (2003): 183-202.

Carp, Stefan A., et al. "Due to intravascular multiple sequential scattering, diffuse correlation spectroscopy of tissue primarily measures relative red blood cell motion within vessels." *Biomedical optics express* 2.7 (2011): 2047-2054.

Carp, Stefan A., et al. "Combined multi-distance frequency domain and diffuse correlation spectroscopy system with simultaneous data acquisition and real-time analysis." *Biomedical optics express* 8.9 (2017): 3993-4006.

Cheung, Cecil, et al. "In vivo cerebrovascular measurement combining diffuse near-infrared absorption and correlation spectroscopies." *Physics in Medicine & Biology* 46.8 (2001): 2053.

Cipolla, Marilyn J. "The cerebral circulation." *Integrated systems physiology: From molecule to function* 1.1 (2009): 1-59.

Durduran, Turgut, et al. "Diffuse optics for tissue monitoring and tomography." *Reports on Progress in Physics* 73.7 (2010): 076701.

Another review of diffuse optics but with a broader perspective on applications. Focuses on mammography and cerebral hemodynamics.

FDA Intralipid® factsheet

Franceschini, Maria Angela, et al. "Assessment of infant brain development with frequency-domain near-infrared spectroscopy." *Pediatric research* 61.5, Part 1 (2007): 546.

Franceschini, Maria Angela. Time-Domain Diffuse Correlation Spectroscopy: From Theory to Human Subject Studies presentation. OSA Biomedical Optics, April 3-6, 2018.

Covers the underlying narrative of my journey on this program as I see it. fNIRS to DCS to TD-DCS, including detector and laser selection, IRF effects, functioning system at MGH and gated TD-DCS.

Grant, P. Ellen, et al. "Increased cerebral blood volume and oxygen consumption in neonatal brain injury." *Journal of Cerebral Blood Flow & Metabolism* 29.10 (2009): 1704-1713.

Ishimaru, Akira. *Wave propagation and scattering in random media*. Vol. 2. New York: Academic press, 1978.

Laser speckle imaging (LSI) in combination with spatial frequency domain imaging (SFDI). Similar to DCS except that light propagation is not sufficiently randomized in the spatial scales covered by SFDI. Stefan worked on this paper.

Krafft, Christoph, and Matthias Kirsch. "In Vivo Brain Imaging and Diagnosis." *Handbook of Biophotonics* (2013): 713-741.

Optical neuroimaging in general. Conclusion highlights special considerations for using light for in vivo measurements with the brain.

Medical Device Information: Time-Domain Diffuse Correlation Spectroscopy (TD-DCS). Martinos Center.

Medical Device Information: Combined Frequency-Domain Near-Infrared Spectroscopy and Diffuse Correlation Spectroscopy Systems (FDNIRS-DCS). Martinos Center.

Medical Device Information: Diffuse Correlation Spectroscopy (DCS) Systems. Martinos Center.

Mesquita, Rickson C., et al. "Direct measurement of tissue blood flow and metabolism with diffuse optics." *Philosophical Transactions of the Royal Society A: Mathematical, Physical and Engineering Sciences* 369.1955 (2011): 4390-4406.

Pifferi, Antonio, et al. "New frontiers in time-domain diffuse optics, a review." *Journal of biomedical optics* 21.9 (2016): 091310.

Roche-Labarbe, Nadege, et al. "Near-infrared spectroscopy assessment of cerebral oxygen metabolism in the developing premature brain." *Journal of Cerebral Blood Flow & Metabolism*32.3 (2012): 481-488.

Svaasand, Lars O., and Reinold Ellingsen. "Optical properties of human brain." *Photochemistry and photobiology* 38.3 (1983): 293-299.

Discusses how light travels in the human brain from neonates to adults. Especially considers penetration depth.

Welbourne, Dustin J., and Will J. Grant. "Science communication on YouTube: Factors that affect channel and video popularity." *Public Understanding of Science* 25.6 (2016): 706-718.

Zhou, Wenjun, et al. "Highly parallel, interferometric diffusing wave spectroscopy for monitoring cerebral blood flow dynamics." *Optica* 5.5 (2018): 518-527.